Co-deposited films of rod-like conjugated molecules: from phase separation to mixing

DISSERTATION

zur Erlangung des akademischen Grades
doctor rerum naturalium
(Dr. rer. nat.)
im Fach Physik

eingereicht an der

Mathematisch-Naturwissenschaftlichen Fakultät I
Humboldt-Universität zu Berlin

von

Herrn Dipl. Phys. Jörn-Oliver Vogel
geboren in Berlin

Präsident der Humboldt-Universität zu Berlin:
Prof. Dr. C. Markschies
Dekan der Mathematisch-Naturwissenschaftlichen Fakultät I:
Prof. Dr. L.-H. Schön

Gutachter: 1. Dr. Norbert Koch

2. Prof. Beate Röder

3. Prof. Annalisa Bonfiglio

eingereicht: 2.4.2009

Datum der Promotion: 6.7.2009

für meine Eltern und Großeltern

Abstract

This thesis is centered on studies of phase separation and mixing in co-deposited thin films of rod-like conjugated molecules. The main focus is to determine which molecular properties lead to phase separation and/or mixing of two materials. To address this question I used five materials, of importance in the context of "organic electronics": pentacene (PEN), quaterthiophene (4T), sexithiophene (6T), p-sexiphenylene (6P), α,ω-dihexylsexithiophene (DH6T). With these it was possible to form material pairs which differ in the parameters: energy levels, length of the conjugated core, and alkyl-end-chain-substitution. All films were deposited by organic molecular beam deposition onto the chemically inert substrates silicon oxide and Mylar, a polyethylene terephthalate (PET) foil. The material pairs were deposited simultaneously from two thermal sublimation sources. The mixing ratio was controlled by the individual deposition rates, which were measured online by a microbalance. The total deposition rate was 0.5 nm/min, and the film thicknesses ranged from 4 nm to 40 nm.

Phase separation is observed for material pairs with dissimilar conjugated core sizes, i.e. [4T/6T]. Noteworthy, the co-deposition of material pairs with similarly sized conjugated cores [4T/PEN] and [6T/6P] lead to well ordered layered structures. The molecules show mixing within layers on a molecular scale and the long molecular axis is oriented almost perpendicular to the substrate surface. Material pairs with similarly sized conjugated core and alkyl-end-chain-substitution [6T/DH6T] and [6P/DH6T] show also growth in mixed layered structures. An especially appealing fact is that the interlayer distance increases proportional to the DH6T content in the film. This can be explained with a phase separation into an aromatic and an alkyl domain vertically to the substrate surface. A decrease of the DH6T content in the film leads to a less dense packing in the alkyl domain. This leads, due to the flexibility of the alkyl chains, to a decrease of the overall interlayer distance.

The low surface corrugation and the interconnected islands render the material pair [6T/DH6T] well suitable for the use as active layer in organic field effect transistors. It is shown that it is possible to tune the charge carrier density in the channel by changing the ratio between 6T and DH6T. This effect enables switching the transistor from enhancement to depletion mode, while maintaining a high charge carrier mobility. This is comparable to p-type doping of inorganic semiconductors.

Keywords: phase separation, mixing, organic molecular beam deposition, OMBD, thin films, OFET, XRD, FTIR, pentacene, quaterthiophene, sexithiophene, p-sexiphenylene, α,ω-dihexylsexithiophene

Zusammenfassung

In dieser Arbeit wird die Phasenseparation und Mischung zwischen konjugierten Stäbchenmolekülen in dünnen Filmen untersucht. Hauptaugenmerk liegt darauf zu ergründen welche molekularen Eigenschaften zu Mischung und/ oder Phasenseparation führen. Mit den 5 Molekülen Pentacen (PEN), Quaterthiophen (4T), Sexithiophen (6T), p-Sexiphenylen (6P), alpha,omega-Dihexylsexithiophen (DH6T) werden Materialpaare zusammen gestellt, die sich in den Parametern „optische und elektrische Eigenschaften", „Länge des konjugierten Kerns" und Alkylkettensubstitution unterscheiden. Alle Schichten werden mittels organischer Molekularstrahlabscheidung auf die Substrate Siliziumoxid und Mylar, einer PET Folie, simultan von zwei Quellen aufgedampft. Das Mischungsverhältnis wird mittels der individuellen Aufdampfraten eingestellt und eine Gesamtrate von 0.5 nm/min eingehalten.

Es wird Phasenseparation für Materialpaare mit ungleicher konjugierter Kernlänge, z.B. [4T/6T], beobachtet. Erstaunlicherweise führt die Co-Verdampfung von Molekülpaaren mit ähnlicher konjugierter Kernlänge [4T/PEN] und [6T/6P] zu wohlgeordneten Filmen, in denen die Moleküle in gemischten Lagen parallel zur Substratoberfläche aufwachsen und die Längsachse der Moleküle fast senkrecht zur Substratoberfläche orientiert ist.

Molekülpaare mit ähnlicher konjugierter Kernlänge und Alkylsubstitution [6T/DH6T] und [6P/DH6T] zeigten ebenfalls geordneten Schichten, wobei als Besonderheit eine lineare Abhängigkeit des Lagenabstandes vom DH6T-Gehalt zu beobachten ist. Dies wird mit einer Phasenseparation in eine aromatische und eine alkyl Domäne erklärt. Mit abnehmendem DH6T-Gehalt im Film ist die Alkyldomäne weniger dicht gepackt, was auf Grund der Flexibilität der Alkylketten zu einer Abnahme des gesamten Lagenabstandes führt.

Die besonders geringe Oberflächenrauhigkeit und die miteinander verbundenen Inseln der [DH6T/6T] Filme prädestinieren sie zur Verwendung in Feldeffekttransistoren. Es wird gezeigt, dass es möglich ist, die Ladungsträgerdichte im Kanal durch Änderung des Verhältnisses zwischen DH6T und 6T so zu verändern, dass der Transistor im Verarmungs- oder Anreicherungsregime betrieben werden kann. Dabei bleibt die Ladungsträgermobilität auf gleich bleibend hohem Niveau. Dies entspricht dem Dotieren eines anorganischen Halbleiters.

Schlagwörter: konjugierte Moleküle, Phasenseparation, organische Mischfilme, Pentacen, Sexithiophen, Quaterthiophen, Sexiphenylen, AFM, XRD, Feldeffekttransistor, organische Halbleiter

Contents

1. Introduction

The story of *organic electronics* started with the observation of photo conductance in crystals of anthracen by Pochettino[1] in 1906. Further time marks were the development of a theory on intra molecular charge transport by R. Markus in the 1960s, which was rewarded with the Noble price in 1992. The prophetic theoretical work of Ratner and Aviram on "molecular rectifiers"[2] in 1974. Heeger, MacDiarmid, and Shirakawa were awarded the Nobleprice in 2000 for their work on charge transport in conductive polymers, which has begun in the 1970s. Compared to the growth in research and application of inorganic semiconductors, the development of *organic electronics* proceeded initially in small steps. However the number of publications on molecular electronics started to rise dramatically in the 1990s.

How can this strong interest in *organic electronics* be explained, since classical silicon based microelectronics is well established and well understood? The first reason is, besides academic interest, that with *organic electronics* it is possible to realize devices, which are not realizable with inorganic materials. The best example is the organic light emitting device (OLED), which is a large area light source, whereas the inorganic LEDs are essentially point light sources. Another example is the OLED display, which is already on the market with 28 cm display size. They have inherent better contrast and lower power consumption than the common LCD displays, because the OLED screen only consumes power for the emitting pixels, whereas the LCD screen only filters a white back light, which is always turned on.

An other reason is costs. All inorganic semiconductor fabrication techniques include energy consuming high temperature process steps. Processing techniques like inkjet printing and roll-to-roll processing suitable for *organic electronics* have a great potential to save money and energy. This is especially important for applications, which are very price sensitive, like radio frequency identification tags, and have moderate requirements on the device performance, or large area applications, like organic solar cells, where photo conversion efficiency versus the cost per surface area is a key factor.

The materials used in the context of *organic electronics* can be divided into two categories, polymers and small molecules, differing mainly in their processability. Polymers are in general processed from solution, using processes like spin coating, inkjet-printing, etc. Small molecules are processed in general by vacuum processes, like organic molecular beam deposition and related techniques. Huge

efforts have been made to make, for instance, pentacene solution processable [3] while preserving its outstanding electrical properties. Another special advantage of *organic electronics* is the possibility to specifically tailor the molecules and their properties for their intended application.

The miniaturization of device structures through top-down methods like photolithography has almost reached the stage of stagnation. This limit can be overcome with the use of self organizing material systems [4]. This miniaturization process is finalized in molecular electronics, introducing devices like molecular transistors [5, 6]. It is therefore of special interest to control the interface between two organic semiconductors by phase separation. This is also of significant importance for the use in organic heterojunction photovoltaic cells [7].

The formation of supramolecular structures is a successful strategy of nature to build up structures of multiple functions from non-covalent bound standard building blocks. Examples are the light harvesting complexes of plants and bacteria in which chlorophyll molecules fulfill the different tasks of collecting the electromagnetic energy (antenna complex) and charge separation (reaction center) [8, 9] depending on their spatial arrangement and their local environment. The cell membrane is another example in which the mixing ratio of two components changes the physical properties of the whole structure. The intercalation of cholesterol into the lipid bilayer has two effects: it prevents the hydrocarbon chains of the phospholipids from crystallization and decreases the permeability of the bilayer for small water-soluble molecules by decreasing the flexibility of the hydrocarbon chains [10].

I want to utilize this strategy to for *organic electronics* applications by combining different organic molecules which form by means of self organization structures with the desired properties. In the context of *organic electronics*, organic composites have been mostly reported focusing on solution processing [5, 11] and evaporated films in the monolayer range [12]. The co-deposition of two organic materials from the gas phase (OMBD - organic molecular beam deposition), which is used in this work, offers the advantages of solvent-free processing and an easy control of the mixing ratio and the film thickness. However, this method has been reported in very few cases. Such studies were focused on donor/acceptor-type molecular pairs for their application in bulk heterojunction solar cells [7, 13, 14] and light emitting diodes [15], where pronounced phase separation was often observed [14, 16, 17].

The objects of my study are five different rod-like conjugated molecules (Fig. 1.2) individually well studied in the context of *organic electronics*. These molecules have in common that they typically grow on insulators, like silicon oxide, in layered structures with their long molecular axis pointing almost perpendicular to the substrate surface. Their π-systems arrange in the so called herring bone pattern and their crystal unit cells have a similar foot print. (C.f. Fig. 1.1). All of these materials exhibit polymorphism. This means that for one material several (meta) stable crystal structures exist, depending on the deposition conditions (cast from solution, organic molecular beam deposition, deposition rate, substrate temperature, substrate material, etc.). A good knowledge of the pure material properties is important to determine which film properties are affected by the co-deposition.

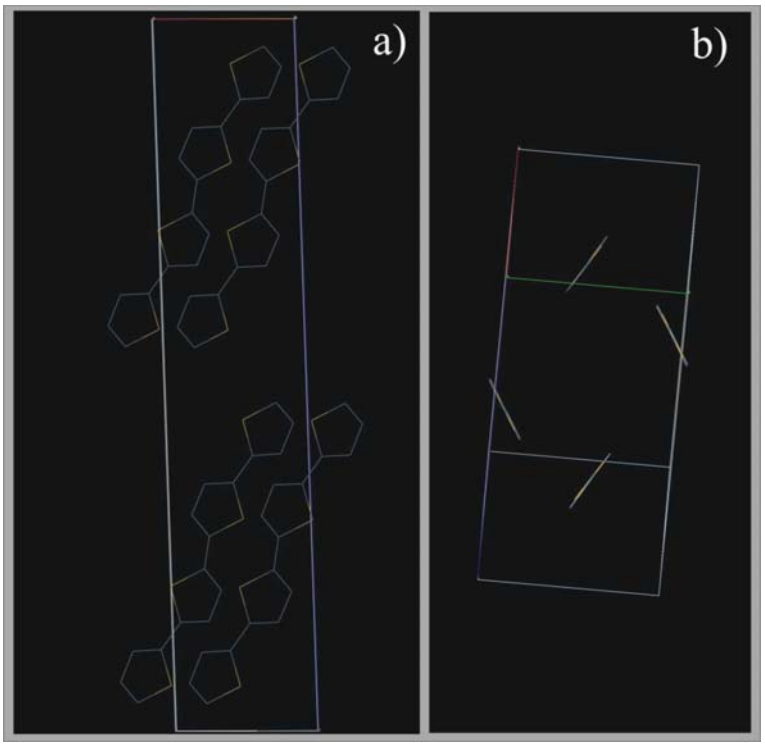

Fig. 1.1: Typical growth mode of rod-like conjugated molecules (4T Low temperature polymorph [18]): a) view along a-axis b) view along the long molecular axis visualizing the typical herring bone structure. [Cambridge Structural Database PEWXAQ01]

With these five materials (Fig. 1.2): pentacene (PEN) [19, 20, 21, 22, 23, 24, 25, 26, 27], α-quaterthiophene (4T) [18, 28, 29, 30], α-sexithiophene (6T) [29, 31, 32], p-sexiphenyl (6P) [33, 34, 35, 36], and α,ω-dihexylsexithiophene (DH6T) [33, 37, 38, 39] it is possible to realize material pairs differing in the parameters: van der

Waals length (vdWL) of the conjugated core (CC), optical and electronic properties and alkyl-end-chain substitution.

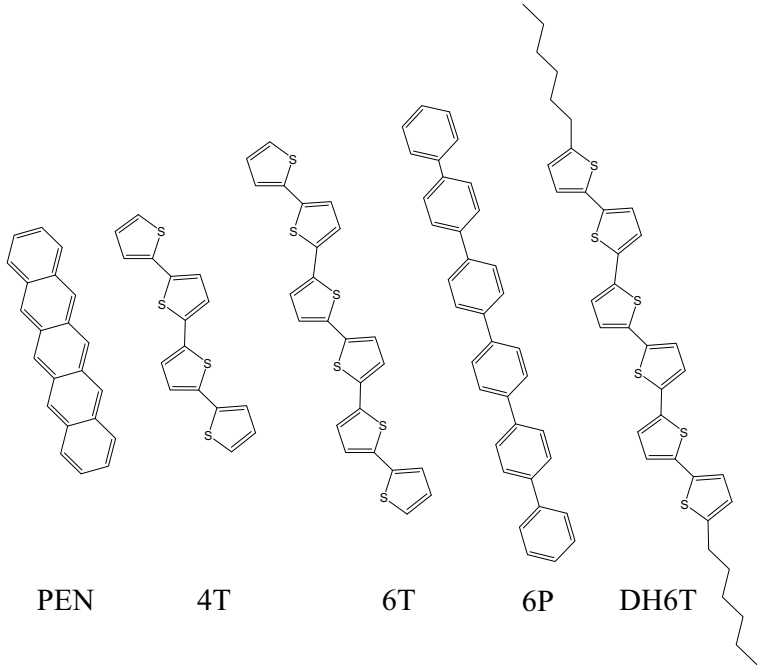

Fig. 1.2: Chemical structures of the used rod-like molecules : pentacene (PEN), α-quaterthiophene (4T), α-sexithiophene (6T), p-sexiphenyl (6P), and α,ω-dihexylsexithiophene (DH6T).

This thesis is structured in the following way: First I will describe the fundamentals of organic electronic starting with the linear combination of atomic orbital (LCAO) to describe elemental electronic properties. This method can be used to approximate the properties of a molecule as a whole from the interaction of its constituent atoms. I then turn to the conjugated molecules, which are in general carbon based, with alternating single and double bonds, which constitute one of the most important material classes in nature i.e. the chlorophyll used in light harvesting systems, the red blood pigment haem are conjugated molecules. Technical applications are devices from organic semiconductors and organic conductors, color pigments, and photoconductors used in laser printers. Starting from the single molecule, I turn to the charge transport properties in the solid state.

Since in organic devices, the metal – organic contacts play an important rule, the problems related to the charge injection barriers will be briefly discussed. Further I will introduce the growth modes of thin organic films and show that the film properties not only depend on the material used but also on deposition conditions in OMBD.

After presenting these fundamentals, I will introduce actual devices that can be realized using organic insulators, semiconductors, and conductors: heterojunction photovoltaic cells, light emitting devices, and field effect transistors. I will explain their typical structure, and their functional principles. For every device the desired properties of the organic semiconductor for best performance are discussed. A special focus will be laid on the phase separation, which is a desired film property for heterojunction solar cells [40], and on the mixing between two organic components, which can be of interest for the active layer of organic field effect transistors. *This is the main motivation to study which molecular properties lead to mixing or phase separation between two conjugated molecules that are co-deposited by OMBD.*

In the materials and methods section I will first introduce the OMBD technique and the used UHV (ultra high vacuum) equipment. This is followed by an introduction of the characterization methods used in this work. Scanning probe microscopy is used to analyze the surface morphology of the films. Infrared absorption spectroscopy can give us first information on the chemical structure of the molecules (Are the materials still intact after the OMBD?) and on the local molecular environment (Is it amorphous or ordered?). X-Ray diffraction experiments deliver information about the domains of the film, which exhibit order. Organic field effect transistors (OFET) are not only a possible application for new materials, additionally, they are also a tool to measure the charge carrier mobility of organic semiconductors.

The results and discussion part of this thesis is divided into two parts. The first part discusses the morphology of thin films grown on the model substrate silicon oxide. I will show that co-deposited material pairs with similarly sized CC (conjugated cores), PEN/4T and 6T/6P, form well ordered layered structures with an intimate mixing on a molecular level. This is followed by the two material pairs, DH6T/6T and DH6T/6P, with similarly sized CC but different overall molecular length due to an additional alkyl-end-chain substitution. These films show well mixed and ordered layered structures. A special feature of these films is possibility to control the interlayer distance *d* by controlling the ratio between the alkylated and non-alkylated component. Material pairs with dissimilarly sized CC, i.e. 4T/6T, PEN/6T, PEN/DH6T, show, in contrast, pronounced phase separation between the two components.

Since the material pair DH6T/6T with similarly sized CC and alkyl substitution exhibited mixed films of low surface corrugation and interconnected islands, it is predestined for the use as active layer in an OFET. I, in collaboration with Dr.

Piero Cosseddu (University of Cagliari), will show that we are able to tune the charge carrier density in the OFET channel by changing the mixing ratio between DH6T and 6T. This enables us to change the OFET working mode from the depletion to the enhancement mode, while simultaneously preserving high charge carrier mobility. This mechanism is comparable to the p-type doping of inorganic semiconductors

This work will be completed with a conclusion and outlook on challenges for the future.

2. Organic electronics

In this section I will give a brief introduction in the fundamentals of organic electronics. Starting with the bond between two atoms and the linear combination of atomic orbitals, we come further to the *Hückel* theory, which can be used to approximate the energy levels of conjugated molecules.

2.1 Conjugated molecules

The creation of molecules by the formation of bonds between atoms can be modeled with the theory of LCAO (linear combination of atomic molecules). As a first case, I will discuss the most simple molecule, the hydrogen ion molecule H_2^+. It consists of two hydrogen cores A and B and one electron. If the electron is located near core A, it mostly feels the electric potential of core A and has as wave function $\psi_{1s}(A)$ similar to the single hydrogen atom, vice versa for core B $\psi_{1s}(B)$. The first approximation is therefore a linear combination of both hydrogen wave functions. N is a scaling factor.

$$\Psi = N\{\Psi_{1s}(A) \pm \Psi_{1s}(B)\}$$

The resulting molecular orbitals have a cylindrical symmetry and are called σ-orbitals. The electron probability density is given by:

$$|\Psi|^2 = \{|\Psi_{1s}(A)|^2 + |\Psi_{1s}(B)|^2 \pm 2\Psi^*_{1s}(A)\Psi_{1s}(B)\}$$

$2\Psi^*_{1s}(A)\Psi_{1s}(B)$ is called overlap density. The electron density increases, when the orbitals overlap and interfere constructive (+). A higher electron density between the positive cores lowers the energy of the molecule compared to the separated atoms. This is called a bonding orbital σ. A destructive interference (-) leads to a decrease of the electron density between the cores and therefore to a higher repulsion and a higher total energy. These orbitals are called anti-bonding σ*.

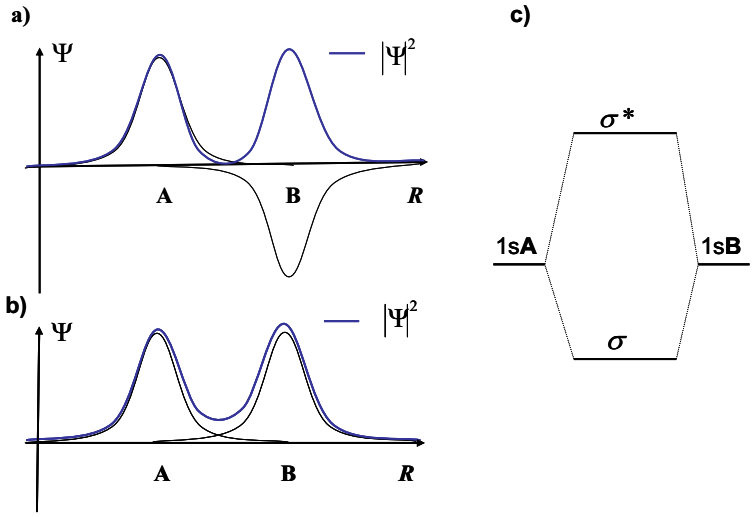

Fig. 2.1: LCAO (linear combination of atomic orbitals) for the H_2^+ molecule. The electron probability density for a) destructive and b) constructive interference. c) The difference in electron density between the nuclei causes the energy shift between bonding σ and anti-bonding σ*-orbital.

For more complex atoms and molecules we need some further simplifications. First we do not take the core orbitals into account, which form the inner closed shells. Second we do not take the virtual orbitals into account, which are the ones that are unoccupied in the ground state. We only treat the valence orbitals of the valence shell.

σ-bonds can be formed by s- and p_Z-orbitals which are rotationally symmetric with respect to the inter-atomic axis. π-orbitals are not rotational symmetric to the inter-atomic axis. Instead, a single nodal plane passes through the two nuclei. π-bonds are weaker than σ-bonds since the overlap is less strong. The overlap integral between two atomic orbitals of different symmetry (σ,π) is zero. The molecular orbitals are filled after G. Lewis with electron pairs of the binding partners. This explains the non existence of the He_2 molecules, because the σ-bond is filled by an electron pair and the next energetic level available is the anti bonding σ^*. The formation of He_2 is energetic unfavorable since the σ^* -bond is slightly more anti-bonding than the σ-bond bonds.

Since carbon is the basis of all organic matter, it is worth to have a look at its binding properties. In the ground state, carbon has a $2s^2\ 2p_x^1\ 2p_y^1$ configuration, which suggests that carbon can only form two covalent bonds since only two orbitals are partially filled. This limit can be overcome by the excitation (promotion) of a 2s electron into an unoccupied 2p orbital. This investment in energy is

recovered by the formation of two more covalent bonds. The now 4 partially filled orbitals ($2s^1$ $2p_x^1$ $2p_y^1 2p_z^1$) can interfere to form hybridized orbitals with different geometries.

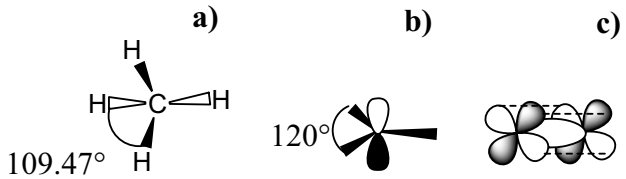

Fig. 2.2: Hybrid orbitals of carbon: a) sp^3, b) sp^2, and c) two sp hybridized carbons forming a triple bond

sp^3 hybrid orbital: Four equivalent partially filled tetrahedral oriented orbitals form σ-bonds with other molecules like hydrogen in methane. (Fig. 2.2 a) The bonds form an angle of 109.47°.

sp^2 hybrid orbital: The $2s^1$ and two $2p^1$ orbitals hybridize to three equivalent orbitals. (Fig. 2.2 b) They lie in one plane and enclose an angle of 120°. The unhybridized $2p_z^1$ orbital is oriented perpendicular to this plane. Two sp^2 hybridized carbons form a σ-bond with their hybrid orbitals and the two $2p_z^1$ orbitals can form a π-bond. A benzene ring can be created by binding 6 sp^2 hybridized carbons together to form a resonance π-electron system. The π-bonds disable the rotation between the atoms and are the reason for the planar arrangement of the benzene ring.

sp hybrid orbital: Two sp hybridized carbons form triple bonds. Here the two hybrids of $2s^1$ and $2p_z$ can form σ-bonds along the intramolecular axis whereas as the two $2p_x$ and $2p_y$ pairs form two π-bonds.

To calculate molecular orbitals for a polyatomic system, we can use the variation principle in which we use a trial wave function $\Psi = c_a\Psi(A) + c_b\Psi(B) + \ldots$. The goal of the variation principle is to find the coefficients c_i giving the lowest energy. The better the trial function is, the better it approximates the real eigenfunctions which give the lowest energy.

$$E = \frac{\int \Psi^* H \Psi d\tau}{\int \Psi^* \Psi d\tau}$$

The minimum is determined by setting the derivative with respect to the coefficients to zero. The secular equations have only a non trivial solution if the secular determinant is zero.

$$\begin{vmatrix} \alpha - E & \beta - ES \\ \beta - ES & \alpha - E \end{vmatrix} = 0$$

with

$$\alpha = \int \Psi^*(A) H \Psi(A) d\tau$$
$$\beta = \int \Psi^*(A) H \Psi(B) d\tau$$
$$S = \int \Psi^*(A) \Psi(B) d\tau$$

Hückel theory for aromatic molecules

A π-electron system is called aromatic if the electrons are delocalized in an electron cloud around the ring system. More specific requirements are that the number of π-electrons equals 4n+2 (Hückel rule), that every atom in the ring should be contributing to the delocalization by having a p-orbital or an unshared pair of electrons. Additionally, the ring system should be planar.

To simplify the quantum mechanical treatment of such systems, the Hückel theory was developed. In this approach σ-bonds and π-bonds are treated separately. The σ-bonds determine the framework of the molecule whereas the π-electron system determines the electronic structure. Following approximations have to be done:

- All overlap integrals *S* are set to zero.
- All resonance integrals between non-neighbors are set to zero
- all neighbor resonance integrals are set to a common value β

With this approximation the secular determinant has diagonal elements *a-E* and off diagonal elements between neighboring atoms: β. All other diagonal elements are zero [41].

Benzene molecule

All carbons in the benzene molecule are sp^2 hybridized and form a hexagon with 120° angles. This matches perfectly the bond angle of the sp^2 hybrid and forms σ-bonds without stress. The 6 p-orbitals overlap to form a ring of 6 π-bonds with following secular determinant:

$$\begin{vmatrix} \alpha - E & \beta & 0 & 0 & 0 & \beta \\ \beta & \alpha - E & \beta & 0 & 0 & 0 \\ 0 & \beta & \alpha - E & \beta & 0 & 0 \\ 0 & 0 & \beta & \alpha - E & \beta & 0 \\ 0 & 0 & 0 & \beta & \alpha - E & \beta \\ \beta & 0 & 0 & 0 & \beta & \alpha - E \end{vmatrix} = 0$$

Solving the secular determinant results in the eigenvalues $E = \alpha \pm 2\beta, \alpha \pm \beta, \alpha \pm \beta$. The lowest energy belongs to an all bonding orbital. The orbital of highest energy is all non-bonding. The two degenerated orbitals are mixtures of bonding and non-bonding bonds. Since we have 6 electrons to fill in, only bonding orbitals are filled. Due to delocalization the π-energy of the benzene is by 2β higher than that of a linear molecule with 3 double bonds. The benzene is especially stable because of the regular hexagon structure favoring strong σ-bonds, all electrons can be accommodate in binding π-orbitals, and the delocalization energy is large. The delocalization energy is the energy of which the π-electron system is lowered compared to a number of ethene molecules with the same amount of double bonds.

Benzene rings can be part of larger aromatic π-electron system like acenes, poly phenyls, or graphene.

2.2 Charge transport

The electrical conductivity σ is defined as $\sigma = qn\mu$ where q is the elementary charge (+e holes, -e electrons), n the charge carrier density and μ the charge carrier mobility. The charge carrier mobility $\mu = v_D / \hat{E}$ is the dependence of the mean drift velocity v_D on the electric field $\hat{E}$. μ of organic materials exhibits two very different temperature dependencies. Ultra pure organic crystals show (similar to inorganic semiconductors like silicon) an increase of μ with decreasing temperature, i.e. for perylene crystals from about 1 cm^2/Vs (300 K) to 100 cm^2/Vs (30 K) [42]. The mobility of disordered small molecule and polymer films has exactly the opposite temperature dependence. E.g. they show a decrease from 10^{-3} cm^2/Vs (350 K) to 10^{-6} cm^2/Vs (200 K) for (4-N,N-diethylamino-2-methylphenyl)-4-methylphenylmethane (MPMP) [43].

This difference in the temperature dependence and in the magnitude of μ is based upon two different mechanisms of charge carrier transport. Pure single crystals exhibit band-like conductivity which is explained in standard solid state physics textbooks [44]. The main contribution to the resistivity is scattering by

lattice vibrations, the phonons, whose density increases with temperature and therefore decreases the mobility.

In contrast, disordered molecular solids show thermally activated hopping conductivity. The charge carriers are localized on so called hopping sites (molecules or small crystal grains) and must be thermally activated to hop from one site to an other site. The mobility increases therefore with increasing temperature. (See Fig. 2.3)

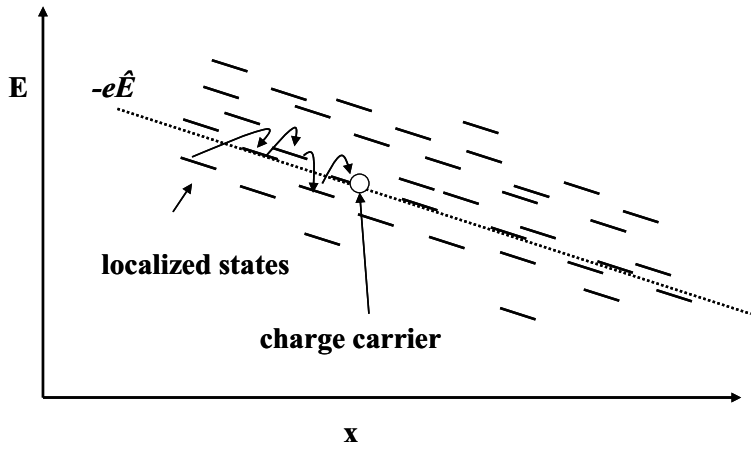

Fig. 2.3: Scheme of the hopping transport mechanism according to the *Bässeler* model in an external electrical field $\hat{E}$. The hopping takes place to sites of lower or higher energies.

Organic films show due to their high defect density a mixture of both transport mechanisms modeled in the multiple trapping and release model by Vissenberg and Matters [45]. Hopping transport for non ordered organic films is reviewed in a paper of H.Bässler [46]. This model is based upon the assumption that the energies E_i of the hopping sites fit a Gaussian distribution. The probability t_{ij} (equ. 2.1 and equ. 2.2) of a hopping from site *i* to *j* depends exponentially on the overlap factor between the two hopping site wave functions 2γ and the distance between the two sites ΔR_{ij}. The second exponential term is a Boltzman term with the energies E_j and E_i of the hopping sites, and the elementary charge *e*. $e\hat{E}(x_i - x_j)$ is the difference in electrostatic energy between the two sites. The difference between the upward $t_{ij}(\uparrow)$ and downward $t_{ij}(\downarrow)$ hopping rates results in a net charge flow along the electrical field.

equ. 2.1
$$t_{ij}(\uparrow) = t_0 \exp(-2\gamma\Delta R_{ij}) \exp(-\frac{E_j - E_i - e\hat{E}(x_j - x_i)}{k_B T})$$

for $E_j - E_i - e\hat{E}(x_j - x_i) > 0$

equ. 2.2
$$t_{ij}(\downarrow) = t_0 \exp(-2\gamma\Delta R_{ij})$$

for $E_j - E_i - e\hat{E}(x_j - x_i) < 0$

The treatment of this model by means of a Monte Carlo simulation results in the following temperature dependence of the mobility:

equ. 2.3
$$\mu = \mu_0 \exp\left(-\left(\frac{T_0}{T}\right)^2\right)$$

Since band transport exhibits at least one order of magnitude higher mobilities, crystalline ordering of the organic semiconductor films is desired for most applications.

2.3 Metal-organic contacts

Most organic devices, like OLEDs, are connected to a power source by metal contacts. The effective injection of charge carriers into OSCs (organic semiconductors) is therefore of importance for good device performance. It is therefore crucial to minimize the electron or hole injection barrier at the interface between metal electrodes and organic material.

In the *neutral contact* approximation [42] the electron injection barrier Φ_e is just the difference between conduction band (CB) of the OSC and the low work function Φ_{M2} of metal M2 (Cf. Fig. 2.4). The hole injection barrier Φ_h is the difference between the OSC valence band (VB) and the high work function Φ_{M1} of metal M1. This picture is strongly idealized, as it has to be assumed that the OSC does not contain charge carriers of its own, in other words is not doped. Additionally, the metal surface should have the same work function as the bulk and no contact dipole between metal and OSC, which alters the work function, should exist.

Unfortunately this picture is too simple. It is a topic under strong debate and in the focus of elaborate photoelectron spectroscopy [47] studies. Since a small charge injection barrier favors the injection of charge carriers and is therefore crucial for a good device performance, large effort is made to minimize this barrier.

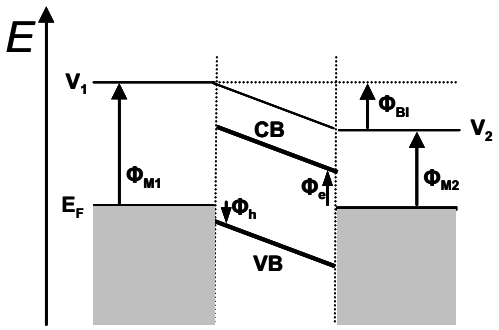

Fig. 2.4: Neutral contacts: An intrinsic semiconductor between two metals M1 and M2 with work functions $\Phi_{M1} > \Phi_{M2}$. The build-in voltage is $\Phi_{BI} = \Phi_{M1} - \Phi_{M2}$. Φe is the electron injection barrier, Φ_h is the hole injection barrier, CB is the conduction band, VB is the valence band and V_1 / V_2 are the vacuum levels of M1 and M2.

Since OSC can not easily be rendered to p- or n-type by doping like inorganic semiconductors, the p- or n-type conduction is determined by the type of charge carriers that are injected into the OSC. In general, low work function metals like calcium ($\Phi \sim 2.9$ eV) are used to inject electrons and high work function metals like gold ($\Phi \sim 5.1$ eV) are used for hole injection. Since the work function of metals vary only in a relative small range and are located near the HOMO of most OSC, the majority of materials can be considered as p-type conductors. The rare occasions of n-type OSC [48] must have a high electron affinity.

2.4 Thin film growth mode

The film growth in organic molecular beam deposition (OMBD) can be described similar to the inorganic molecular beam deposition. However, the main difference is that the atoms can be described as spheres with an almost isotropic interaction to its nearest neighbors. On the other hand, conjugated molecules deposited by OMBD are due to their π electron systems highly anisotropic in their nearest neighbor interactions. In general organic solids have one or even more (meta) stable bulk crystal structures (this is called polymorphism). The interaction with the substrate makes the thin film growth even more complex. A good review of the film growth by Locklin et al. [49] is available. In general thin films grow in three different modes shown in Fig. 2.5.

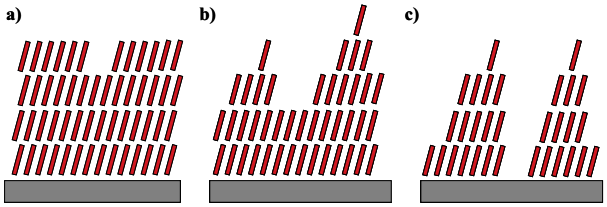

Fig. 2.5: a) Layer-by-layer (Frank-van der Merwe), b) layer-plus-island (Stranski-Krastanov), and c) island-growth (Volmer-Weber)

In thermodynamic equilibrium the growth is determined by the following three interactions (Fig. 2.6):

Φ_{sub} substrate - molecule interaction

Φ_{intra} molecule - molecule interaction – π-π interaction between the π - systems of molecules oriented almost parallel in one layer

Φ_{inter} molecule - molecule interaction – the interaction of an molecule on top of an existing layer of molecules

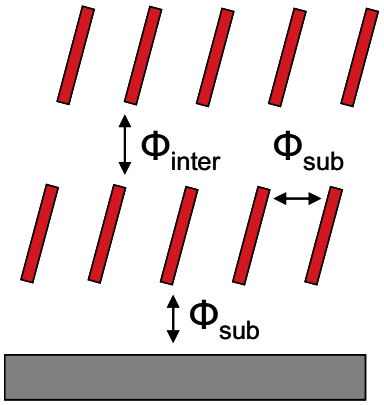

Fig. 2.6: Schema describing the different molecular interactions

The film growth in OMBD starts with a molecule hitting the substrate surface. It will then diffuse on the surface and thermalize or desorb again. The molecule will first lie flat on the substrate to minimize its energy. If Φ_{sub} is large as in the case of metal substrates like gold the substrate surface is first covered with lying molecules. If Φ_{sub} is weak as in the case of inert substrates like silicon oxide, the molecules will arrange almost perpendicular to the substrate surface to maximize the interactions of the π-electron systems and therefore Φ_{intra}.

Island growth is observable if Φ_{inter} is stronger than Φ_{intra} and Φ_{sub}. In this case the molecules can easily diffuse to already existing molecule layers and grow on top of them instead of covering the substrate.

Layer-by-layer growth is observed if Φ_{intra} is comparable to Φ_{inter} and the next molecular layer starts to grow after all coordination sites of the preceding layer are filled. Normally the influence of the substrate fades after a few "wetting" layers and the films starts to grow in layered structures on top of a continuous layer. This is called the *layer-plus-island* mode.

It is therefore possible to influence the film growth by specifically tailoring the molecules. A higher aspect ratio of the rod-like molecule is expected to lead to layer-by-layer growth [50], because the intralayer interaction Φ_{intra} increases while the interlayer interaction Φ_{inter} stays comparable. Additional alkyl-end-chain substitutions as in the case of the DH6T used in this work have two effects. The van der Waals interaction between the alkyl chains increases the intra-layer interaction Φ_{intra}, while simultaneously decreasing the interlayer Φ_{inter} and substrate interactions Φ_{sub}.

Assuming thermodynamic equilibrium, theoretical treatment can give information on the expected growth mode, but cannot predict important parameters like nucleation density, island size, and shape [50, 51]. Kinetic factors like substrate temperature, deposition rate and the kinetic energy of the molecules (controllable by super sonic beam deposition [52]) have a strong influence on the film properties.

A low substrate temperature decreases the diffusion length so that the molecules are basically stuck in place and can not find their bulk arrangement. A higher substrate temperature gives the molecule the opportunity to diffuse on the surface to find a high coordination site and to cross activation barriers. Such an activation barrier is for instance the transition from lying molecules to standing molecules. This has been shown for diindenoperylene (DIP) [53], where the occurrence of domains of lying molecules vanished at higher substrate temperatures or even by annealing the films after deposition. A lowering of the deposition rate has a similar effect since the molecules have more time to diffuse to an existing crystallization nucleus promoting a low island density and higher order. In contrast, high deposition rates can even lead to amorphous film growth since the molecules are just stuck in place and have no time to rearrange. This kinetic effects have been elaborately studied for PEN on SiO_2 by Yanagisawa et al. [51].

The growth of the initial film layer can be explained by the diffusion limited aggregation models [54].

To the best of my knowledge, the co-deposition of two materials via OMBD has not been described theoretically yet. It is clear that a mixing of two kinds of molecules A and B is favored because this increases the entropy of the system. But this is only the case if the interactions between A and B Φ_{AB} are comparable to Φ_{intra} and Φ_{inter} so that the crystallization energy does not decrease significantly when molecules A and B form mixed films.

2.5 Electronic devices

This chapter is devoted to the working principle of organic heterojunction photovoltaic cells (OHPV), organic field effect transistors (OFET) and organic light emitting devices (OLED). After introducing the basic functional principles of each device, it will be discussed how the performance of each device can be improved by the optimization of the organic semiconductor film morphology. Special attention will be given to phase separation and mixing of two different rod-like materials.

2.5.1 Organic heterojunction photovoltaic cell

Unlike other organic electronic devices like OLED and OFET, the OHPV (organic heterojunction photovoltaic cell) has not reached the maturity of commercialization yet, mainly due to the low efficiency and lifetime compared to inorganic solar cells. The goal of current research is to further increase the lifetime and power conversion efficiency while simultaneously decreasing costs by large scale manufacturing processes like roll to roll processing. In the following I will explain the basic function mechanism of solar cells.

Classical inorganic and organic solar cells have the general steps of charge carrier generation in common. First a photon with an energy larger than the band gap of the semiconductor is absorbed. This creates a bound electron-hole pair called the exciton. This exciton has to dissociate into a free electron and a free hole which can then drift by the build-in potential to the electrodes.

The inorganic photovoltaic cell consists of a junction between p- and n-type doped semiconductors. The diffusion length of the excitons is so high that they can diffuse to the p-n-junction. Since the excitons are only weakly bound, they

can easily dissociate there by thermal excitation. The free charge carriers can then drift to cathode and anode driven by the build-in potential which is approximately the difference between the Fermi levels of the p- and n-doped semiconductor.

On the other hand, the radiation creates in organic semiconductors a highly localized exciton which has a binding energy E_B of 0.4 to 1.2 eV [55]. This Frenkel exciton cannot dissociate thermally. In the OHPV [56] the exciton dissociation can only take place at the interface between donor and acceptor type molecules. This principle is shown in Fig. 2.7a. After the excitation of a donor or acceptor type molecule, the created exciton diffuses to the donor - acceptor interface. The exciton can dissociate if the offset between the conduction or valence bands is larger than the exciton binding energy E_B. The now separated electron and hole can then drift to the electrodes supported by the build in potential E_{BI} which is the difference between the work function of the used metal anode Φ_1 and cathode Φ_2.

$$E_{\mathrm{BI}} = \Phi_1 - \Phi_2 \, .$$

We can deduce the requirements on the OSC used in an OHPV by analysing the three main steps of the photo-conversion process.

1. To provide optimal photon absorption the transition dipole moments of the used electron acceptor and donor molecules should be large. The material optical gap should be small to absorb also light down to the red part of the sun spectrum.
2. For maximum quantum efficiency all created excitons have to be able to diffuse to the donor acceptor (D/A) junction, before they recombine radiatively or non-radiatively. It is therefore necessary to increase the exciton diffusion length. An optimal length scale of the D/A domains is in the range of the exciton diffusion length (1 nm to 100 nm).
3. After exciton dissociation at the heterojunction, the charges have to drift to the electrodes. Therefore a direct path from the site of charge separation to the electrodes is needed. Otherwise the charges are trapped in isolated domains and cannot contribute to the external photocurrent. Optimal transport is facilitated by a high charge carrier mobility which requires a high degree of order.

The standard set up of an OHPV consists of a transparent substrate followed by a transparent electrode (normally Indium Tin oxide ITO) covered with the organic semiconductor and a metallic back electrode. The requirements on the or-

ganic semiconductor film lead to an ideal structure of interdigitating rods of donor and acceptor material with phase separation in the order of the exciton diffusion length. (Fig. 2.7b). This structure maximizes the interface of the heterojunction while still providing a direct path for the separated charges to the electrodes. To achieve such morphology was the main motivation for my work and lead my interest to the phase separation between two kinds of OSC materials.

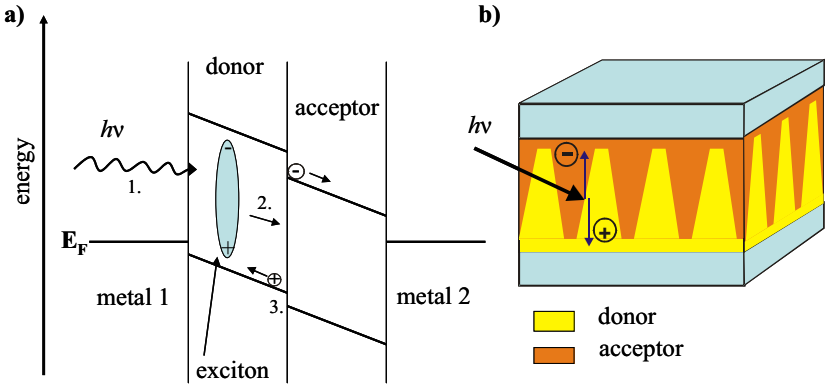

Fig. 2.7: a) Energy scheme of an OHPV. 1.) Absorption of a photon and creation of an exciton. 2.) Exciton diffusion to the donor/acceptor interface and dissociation. 3.) Drift of the charge carriers to the metal contacts. b) Scheme of an OHPV cell

2.5.2 Organic field effect transistors

Organic transistors have reached the level of commercialization in the last years. They are used in the field of low cost "plastic electronics" applications like single use sensors [57] or radio frequency identification tags [58]. In research organic field effect transistors (OFET) are a powerful tool to determine charge carrier transport properties of OSC. I will first explain the basic principles of the OFET which is a close relative of the metal oxide semiconductor field effect transistor (MOSFET). The OFET has typically a metal-insulator-OSC structure which can be thought of as a plate capacitor with the gate electrode and the semiconductor forming the capacitor plates. (See Fig. 2.8.) They are separated by a very thin insulating layer called gate dielectric. The source and drain contacts, which are separated by a gap called the channel, can inject charge carriers into the semiconductor. An OFET works mostly in the accumulation mode meaning that for p-type OSC a negative bias V_G and V_D is required in order to obtain charge carrier accumulation and transport within the device channel. A negative bias V_G attracts holes to the OSC/gate dielectric interface and enables us to effectively control

the charge carrier density n_H in a very narrow 2D channel near to the interface. Charge carriers are highly localized at the OSC/insulator interface, because the electrical field decays very fast (2-3 molecular layers). By applying a positive gate voltage V_G it is possible to push the holes away from the interface and, as a consequence, to fully deplete the channel of holes. This voltage is called threshold voltage V_T. If the positive bias is further increased electrons are induced into the channel. This is called the inversion regime. Normally the current in the inversion regime is negligible since the charge injection is small due to a high electron injection barrier. See metal organic contacts chapter 2.3. The OFET is not in the off state at zero gate voltage V_G, if the p-type OSC is doped by lattice defects or oxidation. The holes must therefore actively pushed away from the interface resulting in a positive threshold voltage V_T.

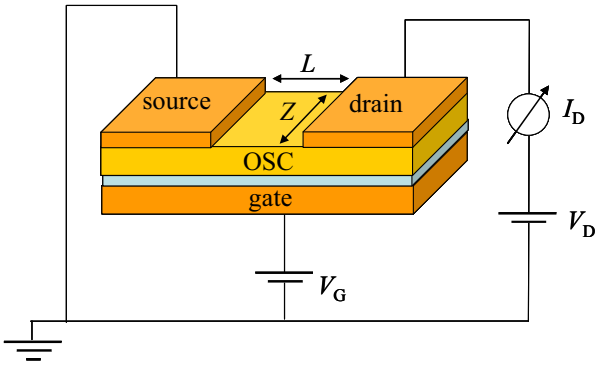

Fig. 2.8: Scheme of an organic field effect transistor (OFET). *L*: channel length, Z: channel width, V_G: gate voltage, V_D: drain voltage, I_D: drain current. The thin blue layer is the gate dielectric.

The OFET works in two different regimes:

In the linear regime ($V_G < V_D << (V_G - V_T)$) the gate voltage V_G is more negative than the drain voltage V_D and therefore the electrical field and charge carrier density in the channel are almost homogeneous. The drain current I_D increases linearly with the drain voltage V_D and can be described with the following formula, where Z is the channel width, L the channel length, C_i the capacitance of the gate electrode, and μ the field effect mobility. See Fig. 2.8 and Fig. 2.9.

equ. 2.4

$$I_D = \frac{Z}{L}\mu C_i\left[(V_G - V_T)V_D - \frac{V_D^2}{2}\right]$$

The further increase of V_D results in a zero electrical field between gate and drain electrode. This result in an area in the channel, in which no free charge carriers are present. This effect is called pinch-off. A further increase of the applied source-drain voltage V_D will not lead to a significant increase of the source-drain current I_D. The OFET saturates and I_D is only dependent on the gate bias V_G. The drain current I_D in the saturated regime can be calculated with following equation [59].

equ. 2.5

$$I_D = \frac{Z}{2L}\mu C_i (V_G - V_T)^2$$

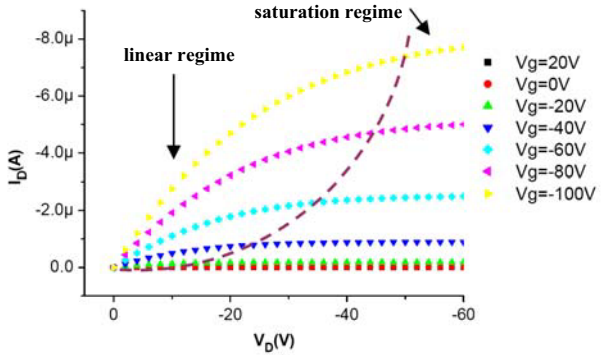

Fig. 2.9: Output characteristics of an OFET with linear and saturated region. The dashed line shows the onset of the saturation regime, the pinch off voltage, from [60].

One of the fundamental points in determining the electrical performances in OFETs is that, even though they are usually thought of as macroscopic devices, their behaviour is strongly driven by interfacial phenomena taking place on the nano-scale. On the one hand, there are the intrinsic properties of the organic semiconductor such as molecular packing and island or domain boundaries, where the interfaces are on the molecular and inter-island scale. On the other hand, there are the interfaces organics/electrodes and organics/gate dielectric which are dependent on the device structure, and significantly dictate the electronic properties of the OFET.

In this thesis I will show how by a proper engineering of the OFET active layer a fine tuning of its most important parameters can be achieved.

2.5.3 Organic light emitting devices

The organic light emitting device (OLED) uses the reversion of the photovoltaic effect to produce photons from electrical power. Fig. 2.10 shows a scheme of a prototypical two layer OLED. The first step is the charge carrier injection. Holes are injected from a high work function metal, e.g. ITO, Au into the hole transport layer (HTL) and the electrons are injected by a low work function material, e.g. Ca, Mg, Ag, Al, into the electron transport layer (ETL). The charge carriers drift to the interface between HTL and ETL (emission layer) where they recombine to excitons. The offset between HOMO and LUMO of the ETL and HTL is needed to prevent the charge carriers from drifting to their counter electrode resulting in radiation less recombination. The formation of exciton results in ¼ singlet excitons and ¾ triplet excitons which can not decay radiative and are therefore lost for the direct conversion into light. This can be overcome by the use of triplet emitters which have effective radiative triplet decay channels due to the heavy nuclei effect. Actual OLEDs consist of up to 5 or more layers of vacuum deposited small molecules and solution processed polymers. This makes the morphology of the interfaces between the layers very important. Also guest host system are important (mixing).

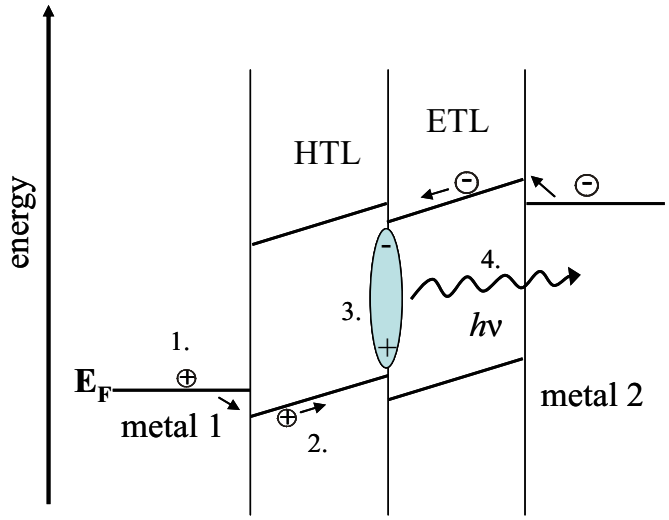

Fig. 2.10: Scheme of two layer OLED. 1) Charge injection, 2) Charge transport 3) Exciton creation and 4) Radiative decay. The energy diagram is drawn for an applied external voltage which is larger than the build in voltage V_{BI}.

3. Materials and methods

In this chapter I will describe the organic materials which are used to fabricate the co-deposited thin films. The technique of organic molecular beam deposition will be explained with focus on its advantages: The solvent free processing; the easy control of the mixing ration of two organic moieties; and easy control of the film thickness. The samples are characterized by complementary characterization methods which as a sum give a comprehensive picture of the film properties. The surface morphologies of the films are characterized by scanning probe microscopy, which gives the first indication on phase separation and mixing observable on the film surface. Infrared spectroscopy (IR) gives information on the bulk properties of the film. It delivers information if the molecules are still chemical intact after the deposition. Further IR can deliver information on the local environment of the molecules. It gives therefore indications for phase separation or mixing; and ordered or amorphous growth.

X-ray diffraction delivers information on the ordered contents of the films. New mixed crystalline phases could be detected as well as the separation into ordered domains of pure material. The last part of this section will treat the OFETs. They are used to characterize the electronic properties of the films such as the charge carrier mobility μ and are additionally a proof of concept for an actual application for the studied organic films.

3.1 Materials

Pentacene (Aldrich), 4T (Aldrich), DH6T (H.C. Stark) and 6P (TCI Europe) were used as received. 6T (Aldrich) was purified by temperature gradient vacuum sublimation by S. Hirschmann in the Group of Prof. Dr. Jens Pflaum Universität Stuttgart. As substrate for infrared spectroscopy we used 1.5 mm thick doubleside polished (0 0 1) Si wafers (Siegert Consulting). For AFM measurements 0.5 mm thick singleside polished (0 0 1) Si wafers (Siegert Consulting) were used. Both wafers have a native oxide layer. The silicon was cut into 1 cm^2 coupons with a diamond tip. During the cutting process the surface comes only into contact with KIMTECH wipes (Kimberly Clark). After every step, the surface was vigorously blown with dry nitrogen to remove any debris from the scratching process, which might scratch the surface. The silicon coupons are then used without further cleaning.

3.2 Organic molecular beam deposition

The vacuum chamber consists of two main parts, the load lock and the preparation chamber, which is pumped by an ion getter pump (Varian). The load lock is used to transfer the samples from the ambient to ultra high vacuum in the main chamber. After the sample is placed in the load lock and the load lock is evacuated by the turbo pump (Varian V301) for about 20 min, the gate valve between load lock and main chamber is opened. Then the transfer rod can pick up the sample from sample holder in the load lock and transfer it into the preparation chamber. To start the deposition of the organic films the substrates, still attached to the transfer rod, are turned towards the sublimation sources. The nominal mass thickness is monitored online with a microbalance (Syncon STM100). The microbalance consists of a quartz crystal which is electrically excited to perform vibrations at its resonance frequency. The deposition of a very thin film on top of the crystal leads to a decrease of the resonance frequency. This can be evaluated by the controller into a nominal mass thickness. (Parameters: density 1.35 g/cm^3, tool = 100%, z = 100%). We monitor the film thickness by a labview program which tracks the actual deposition rate. We are able to co-deposit up to 4 different materials simultaneously. A central shutter can block each molecular beam to measure the deposition rate of each source separately. (Fig. 3.1)

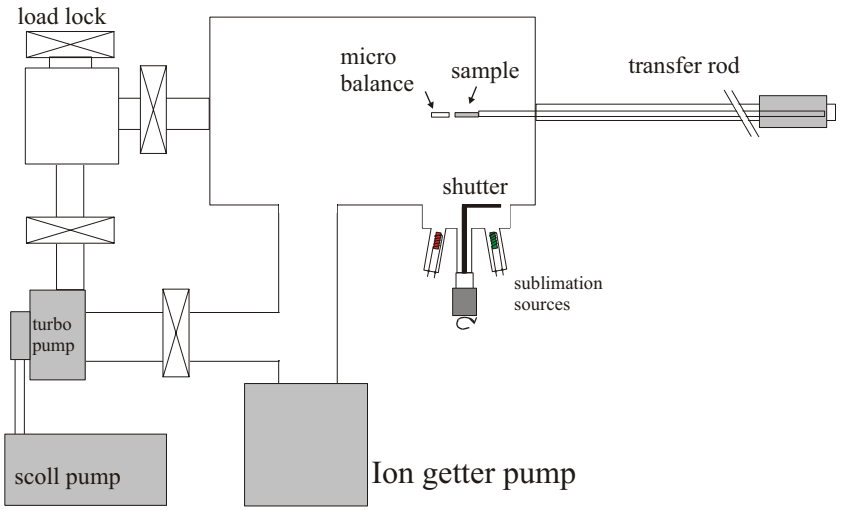

Fig. 3.1: Schematic drawing of the vacuum chamber which was used to deposit OSC onto the substrates.

3.2.1 Sublimation sources

The organic molecules are sublimed from the solid phase by heating in a ceramic crucible. Sublimation [41] is the direct phase transition from the solid to the gaseous phase for temperatures lower than the triple point temperature T_{tp} (Fig. 3.2). The ceramic (AL_2O_3) crucibles are resistively heated by Tantalum wires because of their high melting point and their much superior processability compared to the brittle Tungsten wires. The deposition rate is controlled by the heating current. The sources delivered stable deposition rates over hours.

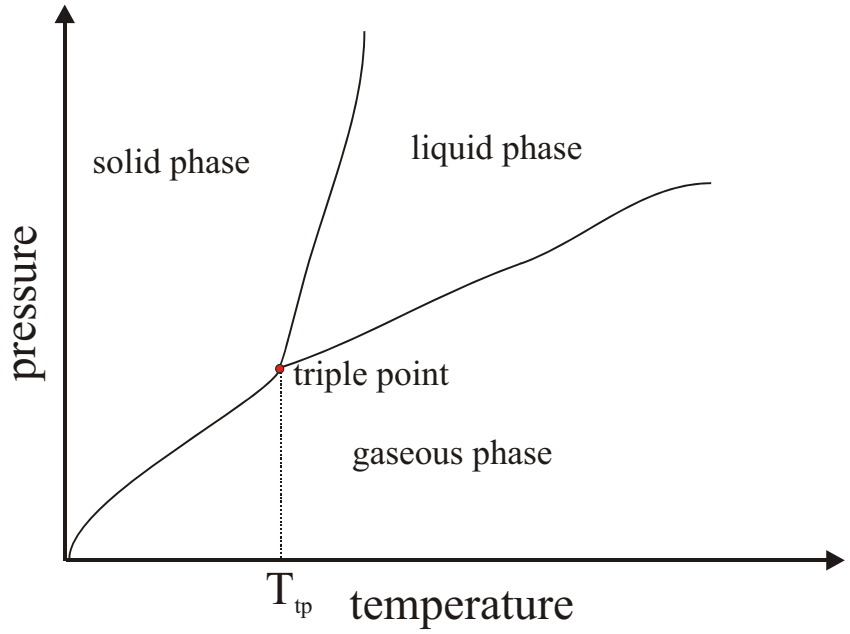

Fig. 3.2: Phase diagram showing the phase boundaries between solid, liquid, and gaseous phase. The point of co-existence of all three phases is called triple point.

3.2.2 Vacuum

The organic molecules are sublimed from crucibles at temperatures from 80 °C to 250 °C. To estimate if the molecules hit residual gas molecules on their way to the sample, I estimate the mean free path with equ. 3.1. In this coarse approximation [61] I assume an atmosphere consisting of molecules with a very large diameter d of 2 nm (comparable to pentacene), a partial pressure P of 10^{-7} mbar and a temperature T of 300 K. The resulting free mean path length is 23 m, which is two orders of magnitude larger than the source sample distance of 0.3 m in the vacuum chamber. Therefore most of the molecules reach the substrate without a collision with residual atmosphere.

equ. 3.1

$$\lambda = \frac{k_B T}{\sqrt{2}\pi d^2 P}$$

3.3 Scanning probe microscopy

All SPM (scanning probe microscopes) operate with a similar principle. A very small probe scans and senses the sample surface via a short range interaction. This interaction is usually used to measure the separation between probe and sample surface. Thereby, the tip-sample distance is kept constant with sub atomic resolution by a piezo stage (constant height mode). The surface of the sample is scanned line by line resulting in a three dimensional map. The advantage of the SPM technology is, that it is able to measure in real space with a resolution which is only limited by the decay length of the used short ranged (near field) interaction. This results for some SPM techniques in possible atomic resolutions. In contrast to light and scanning electron microscopy, which are as far field techniques diffraction limited to a resolution of half of their wavelength.

SPM was invented by Binning and Rohrer [62] in 1982 with the scanning tunneling microscope (STM). The STM images the sample surface with a very sharp metallic tip. (See Fig. 3.3.) The tip or the sample is moved by a piezo scanner. If a voltage between tip and sample is applied, a very small quantum mechanical tunnel current I_T begins to flow. It has an exponential dependence on the tip sample separation and decreases one order of magnitude with an 1 Å increase in tip-sample distance. The tunnel current is therefore a very good measurand for the tip-sample distance. A drawback is that this method is limited to samples with conducting surfaces. Yet, it is possible to image very thin films of non conducting materials, if they are thin enough to allow the electrons to tunnel through the non conducting barrier (~1 nm).

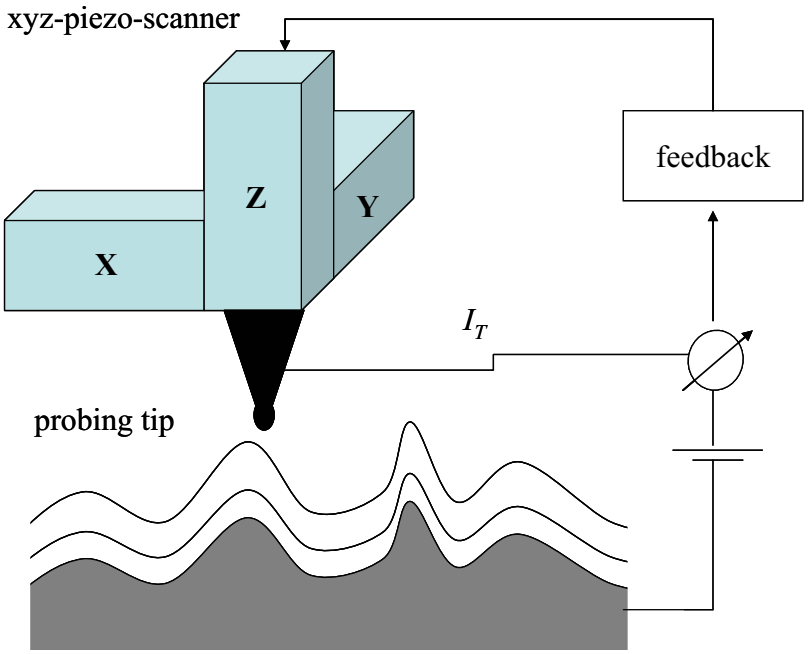

Fig. 3.3: Scheme of a STM (Scanning tunneling microscope).

To measure samples with non conducting surfaces Binnig, Quate, and Gerber [63] developed the AFM (Atomic Force Microscope) in 1986. The first version of this now SFM (Scanning Force Microscope) called device utilizes a diamond tip on a cantilever whose Z-movement was monitored by a STM tip on the rear of the cantilever. Today most SFM use the beam deflection method [64]. A light beam is reflected from the backside of the cantilever and its deflection is measured with a four segment photodiode. (Fig. 3.4)

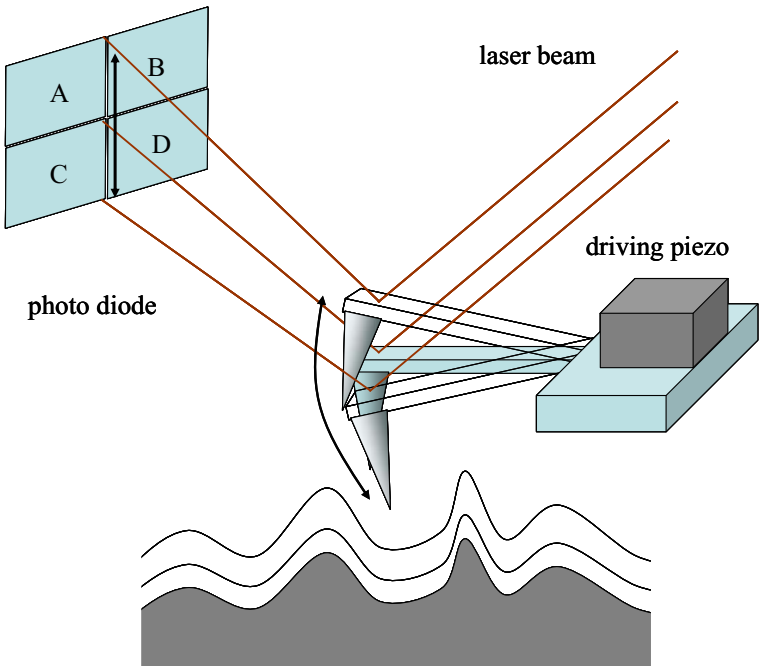

Fig. 3.4: Scanning force microscope (SFM) in beam deflection mode setup.

There are several operation modes for the SFM. First, we distinguish between static and dynamic modes. The most used static mode is the contact mode (CM) in which the tip-sample distance is controlled so that a constant tip bending is achieved. This method can be used on hard rigid sample surfaces like metal clusters on metal single crystals. For organic samples the tip-surface interactions in CM are often stronger than the molecule-substrate interaction which can result in nano manipulation of the sample, instead of an imaging.

In the dynamic mode a piezo actuator forces the cantilever to vibrate near its resonance frequency. There are two ways to measure the tip-sample interaction. 1) The shift of resonance frequency is measured. This mode is often applied in vacuum SPM, where the damping is low and the cantilever has a very high Q-factor (small band width). 2) In atmosphere or liquids (low Q-factors) it is useful to detect the amplitude of the oscillation at a fixed resonance frequency. Throughout this work the SFM Veeco Nanoscope IV was used in the tapping or intermittent contact mode. Here the cantilever is excited near to its resonance frequency and conducts oscillations of several nanometer amplitude, getting only for a short moment in close contact (tapping) with the surface. This reduces the friction forces while scanning.

A range of different forces act on a SFM cantilever. This is in contrast to a STM, where due to its exponential decay, the tunneling through the outermost atoms of the tip dominates the tunneling current.

The short range forces on a SPM probe can be attractive or repulsive. The repulsive force is caused by the Pauli exclusion principle, which causes repulsion when electron orbitals of same spin are superimposed. On the other hand, can an overlap of electron wave functions be attractive, when it lowers the total energy similar to a chemical bond This short range forces can be described with the repulsive part of the Lennard-Jones potential (equ. 3.2) which is strictly only applicable for interactions between uncharged, not chemical interacting atoms.

A part of the long range forces is the attractive part of the Lennard-Jones potential caused by the Van der Waals forces which are dipole-dipole interactions. These dipoles emerge from fluctuations and interact with dipoles induced by their own electrical field. r is the distance between two atoms, ε is the depth of the potential, σ is the (finite) distance at which the potential is zero.

$$V = 4\varepsilon\left[\left(\frac{\sigma}{r}\right)^{12} - \left(\frac{\sigma}{r}\right)^{6}\right] \qquad \text{equ. 3.2}$$

At a distance of 0.5 nm the attractive Van der Waals force on the tip is in the range of F_{VdW} = 2 nN [65]. At this tip-sample distance of 0.5 nm [65], the short range forces become comparable to the longer range forces and pose therefore the upper limit for atomic resolution.

In ambient conditions micro contacts can act as condensation nuclei for water vapor. A micro contact can be the crystallization site of a water meniscus, if the radius of curvature is small than the Kelvin radius r_K (equ. 3.3).

$$r_K = \frac{\gamma V}{R_m T \log(p/p_S)} \qquad \text{equ. 3.3}$$

The Kelvin radius r_K depends on the partial pressure p and saturation vapor pressure p_S, surface tension γ = 0.074N/m (20°C Water), gas constant R_m, temperature T, the molar volume V. For a relative humidity of p/p_S = 0.9 a Kelvin radius of 100 nm is obtained. For smaller p/p_s this formula is not applicable, since r_K becomes comparable to the size of molecules.

Condensation is possible since the typical SFM tip radia are much smaller than 100 nm. It is possible estimate the force [66] with (equ. 3.4) where R is the radius

of curvature, Φ the angle of the meniscus, θ the contact angle, and D the distance between tip and sample. This results in a maximal attractive force of $F = 9.3 \cdot 10^{-8}$ N, which is much larger than the van der Waals Forces. Typical force vs. distance measurements in ambient reveal adhesion forces in the order of 10^{-8} N - 10^{-7} N mainly originating from capillary forces [67]. Therefore large oscillation amplitudes are a prerequisite for the tapping mode in air, since the restoring force of the cantilever spring has to overcome the capillary forces.

$$F = \frac{4\pi R\gamma \cos\Theta}{1 + D/[R(1-\cos\Phi)]}$$

equ. 3.4

3.3.1 Image processing

Since the surfaces of some thin films (Fig. 3.5 a) exhibit very flat layered structures it is useful to measure the average step height between this layers with high precision. For image processing I used the software package SPIP 3.2.11.0 by Image Metrology ApS. In the height image (Fig. 3.5 a) of the raw data the substrate surface is tilted relative to the image plane and the height histogram (Fig. 3.5 b), which shows the distribution of pixels with certain height values, is featureless.

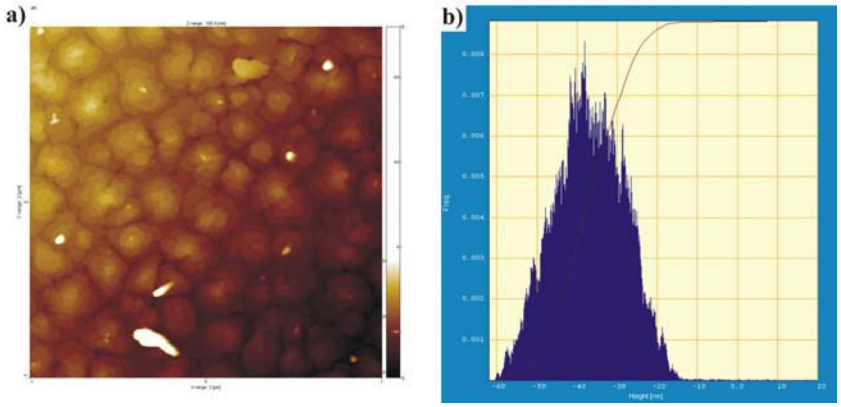

Fig. 3.5: SFM raw data of a 20 nm thick organic film on SiO_2 a) height image b) height histogram - distribution of pixel with certain height value.

As first step I used the "plane correction menu" to tilt the image so that the scan lines are parallel to the image plane (Fig. 3.6 a). Now, the height histogram (Fig. 3.6 b) shows regular peaks representing the different layers on the surface. The next step is to perform the "histogram alignment" routine on the image. This routine fulfills the following process steps. For every individual scan line a height

histogram is produced and the program assigns the maxima of this distributions corresponding to different height levels (planes parallel to the image plane).

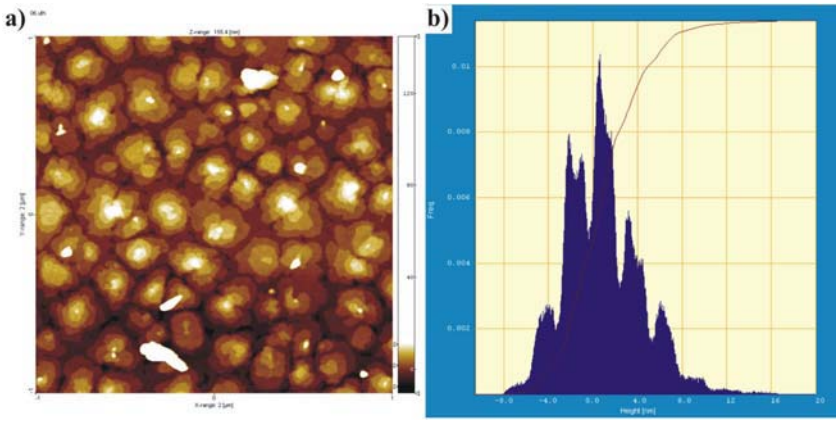

Fig. 3.6: SFM image after tilting the scan lines parallel to the image plane a) height image b) height histogram.

Since between the individual scan lines small offsets in height occur, the program corrects them by adding an offset so that the maxima in the height histograms match. The resulting height histogram Fig. 3.7 b) exhibits Gaussian shaped peaks representing the different molecular layers (Fig. 3.7 a). These peaks can be fitted with multiple Gaussians (Fig. 3.8a). The average step height results from the slope of the linear fit of the peak centers height over layer number (Fig. 3.8 b).

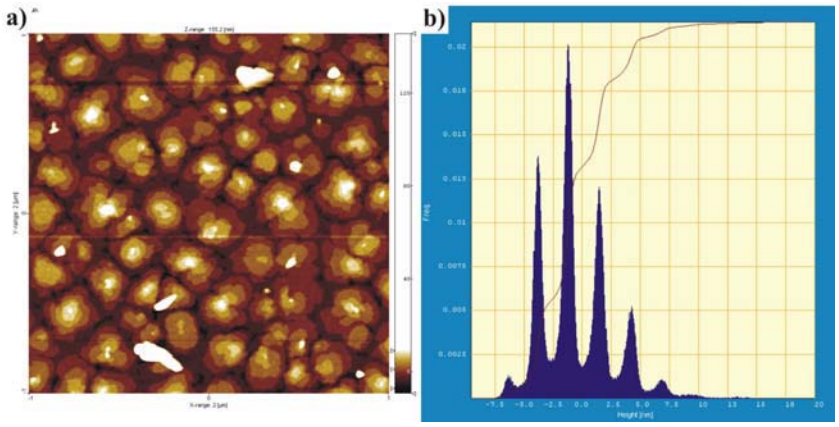

Fig. 3.7: SFM image after the histogram alignment routine. a) height image b) height histogram.

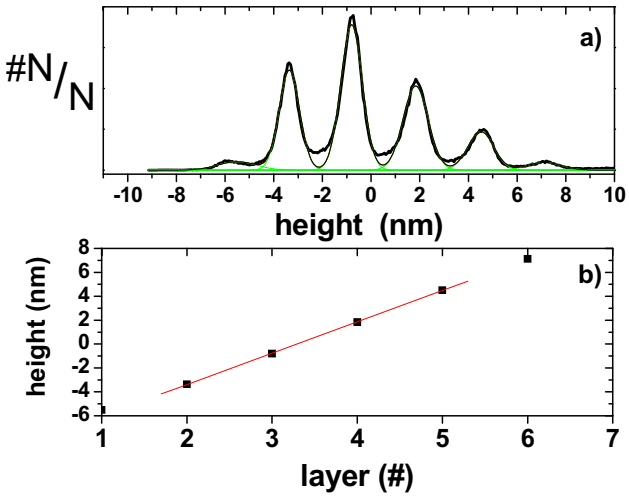

Fig. 3.8: a) The peaks of the height histogram are fitted with Gaussians. b) The peak center vs. peak number. The red line is the result of a linear fit to determine the average step heights.

3.4 Infrared spectroscopy

In this section I will describe the most simple model for molecular vibrations, the harmonic oscillator. This simple model enables us to understand the basic distinction into functional group and fingerprint region in the near infrared region NIR. In section 3.4.2 I will explain the mechanism of the Davidov splitting which is a direct effect of the molecular arrangement into organic crystals and of great importance for my work. I will then introduce the general setup of a Fourier transform Infrared spectrometer and finally describe the used setup.

3.4.1 Infrared active vibrations

The most simple molecules which can perform vibrations are diatomic ones. In the first approximation atoms are represented by two point masses m_1 and m_2 and are bound together by a spring with spring constant k. R is the separation between the atoms and R_0 the average separation. $V(R)$ *is* the *harmonic* potential $V(R) = \frac{1}{2}\, k(R-R_0)^2$. Its classical solution is a harmonic oscillation with frequency ω with the reduced mass $\mu = m_1 m_2/(m_1+m_2)$.

$$\omega = \sqrt{\frac{k}{\mu}}$$

equ. 3.5

However, to explain the light absorption the stationary solution of the Schrödinger equation (equu. 3.6) of the harmonic potential has to be used.

$$-\frac{\hbar^2}{2\mu}\frac{d^2\Psi}{dR^2}+V(R)\Psi = E\psi$$

equ. 3.6

The eigenvalues of the solutions are $E_n = (n+½)\hbar\omega$ with ω from the classical solution. The selection rule for the optical transition is $\Delta n = \pm 1$. A more realistic model for the potential between two atoms is the *Morse* potential which models the strong Pauli repulsion between two atoms and allows dissociation of bonds (Fig. 3.9). The harmonic oscillator is still a good approximation since at room temperature most molecules are in the ground state and for low energies morse potential and the harmonic potential match.

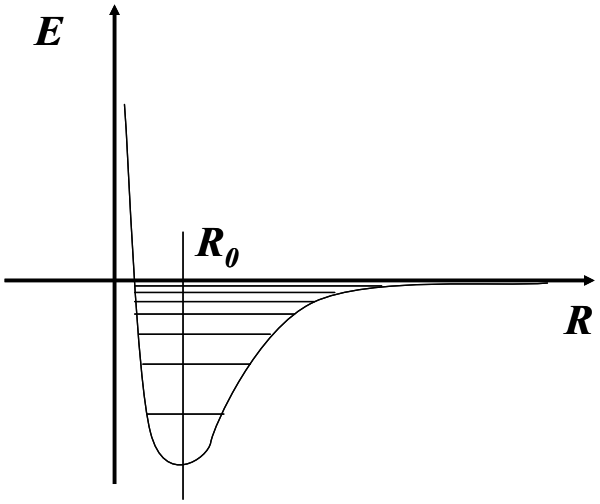

Fig. 3.9: Morse potential modeling the bond in a diatomic molecule. *E* is the energy, *R* is the separation R_0 average separation between the two atoms.

The first item which can be estimated from this model and equ. 3.5 is that vibrations of light atoms like hydrogen, bound to heavier atoms like carbon ($\mu \approx m_H$) oscillate in the high frequency range (1000 cm^{-1}– 3000 cm^{-1}) called functional group region. The vibrations of the whole molecule (large μ) are located at low frequencies (500 cm^{-1}– 1000 cm^{-1}) called fingerprint region, because they are characteristic for a certain molecule and can be used to identify substances from a database. The gross selection rule for the optical activity of molecular vibrations is that the electric dipole moment of the molecule must change when the atoms are displaced. (Fig. 3.10). A permanent dipole moment is not necessary.

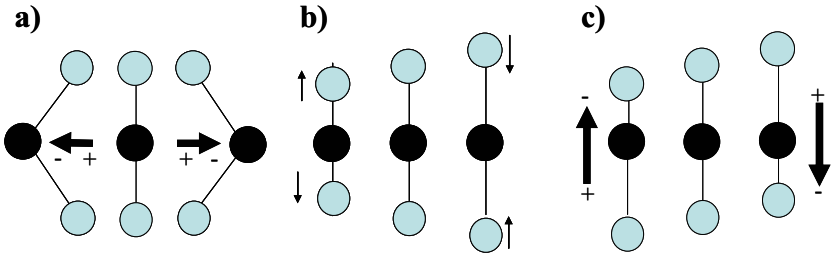

Fig. 3.10: Vibration of the carbon dioxide molecule. a) bending (IR active), b) symmetric stretch (IR inactive) c) asymmetric stretch (IR active). The bold arrows denote the dipole moment.

3.4.2 Davydov splitting

A.S. Davydov developed a substantial part of the theory of optical line shifts and splittings in organic crystals which is known under his name [68]. I start the discussion with a simple model dimer of equivalent molecules with ground state wave functions Φ_1 and Φ_2 and energies E_1, $E_2 = E_0$. The non coupled dimer has the energy $E_G = 2\,E_0$ and the wave function $\Phi_g = \Phi_1\,\Phi_2$. One of the molecules can be excited into Φ_1^* (with E^*) or Φ_2^* (with E^*) and with equal probability. The single excited dimer wave functions $\Phi_\pm^*$ are linear combination of excited and non excited wave functions. The energies of the exited dimer $E^*_\pm$ for $\Phi_\pm^*$ are degenerated $E^*_+ = E^*_- = E_0 + E^*$.

$$\Phi^*_\pm = \frac{1}{\sqrt{2}}(\Phi_1\Phi^*_2 \pm \Phi^*_1\Phi_2)$$

equ. 3.7

If an interaction V_{12} between the two molecules is turned on, the degeneracy is lifted. E^*_+ and E^*_- differ by the resonance interaction energy I_{12} describing an exchange of the excitation energy between molecule 1 and 2.

$$I_{12} = \left\langle \Phi^*_1\Phi_2 \middle| V_{12} \middle| \Phi_1\Phi^*_2 \right\rangle$$

equ. 3.8

The *Davydov* splitting is defined $\Delta_D = 2I_{12}$. The energy oscillates between the two molecules with $\omega = \Delta_D/\hbar = 2I_{12}/\hbar$. The ground state energy E_G gets an additional shift by the Coulomb interaction in the ground state D^0, which is identical to the van der Waals binding energy. (See Fig. 3.11). The exited state energies E^*_+ and E^*_- are additionally shifted by the Coulomb interaction energy D' of the excited molecule with the molecule in the ground state.

equ. 3.9

$$D^0 = \left\langle \Phi_1 \Phi_2 \left| V_{12} \right| \Phi_1 \Phi_2 \right\rangle$$

equ. 3.10

$$D' = \left\langle \Phi_1^* \Phi_2 \left| V_{12} \right| \Phi_1^* \Phi_2 \right\rangle$$

Normally $D^0 > D'$ and the optical transition is red shifted by the so called "solvent" shift $D = D'-D^0$. D is caused by the polarizability of the environment (molecule 2 can be a chromophore or a solvent molecule) whereas I_{12} can only be caused by the resonance interaction between two identical molecules.

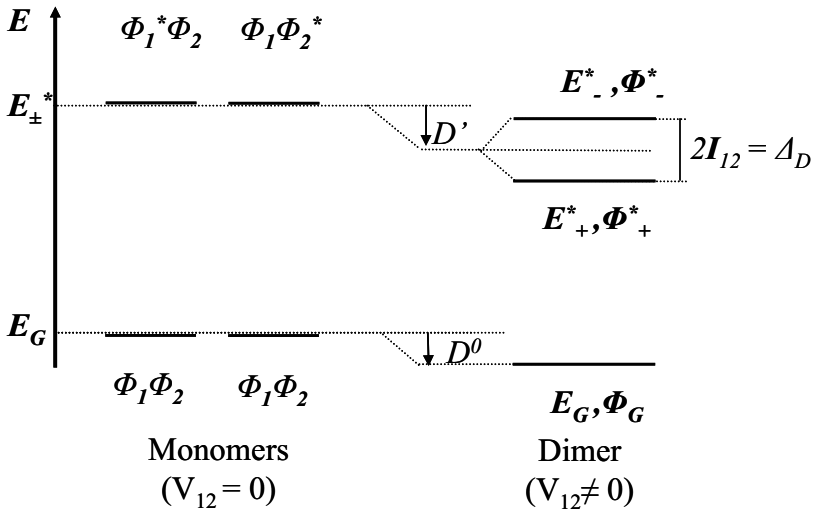

Fig. 3.11: The Davydov splitting Δ_D and the solvent shift $D = D'-D^0$ in respect to the monomer without interaction V_{12}.

The polarization of the optical transition into the Davydov levels is given by vector addition of the single molecule transition dipoles $\vec{M}^1$ and $\vec{M}^2$.

equ. 3.11

$$M^{\pm}_{S1-S0} = \left\langle \Phi_G \left| e \cdot \vec{r} \right| \Phi^*_{\pm} \right\rangle = \frac{1}{\sqrt{2}} \left\langle \Phi_1 \Phi_2 \left| e \cdot \vec{r} \right| \Phi_1 \Phi_2^* \pm \Phi_1^* \Phi_2 \right\rangle$$

$$= \frac{1}{\sqrt{2}} [\vec{M}^2 \pm \vec{M}^1]$$

The special case $\vec{M}^1 \parallel \vec{M}^2$ (Cf. Fig. 3.12 a) results in the allowed transition M^+ and the forbidden transition M^-. The non-parallel orientation of $\vec{M}^1$ and $\vec{M}^2$ (Cf. Fig. 3.12 b) leads to two allowed dimer transitions which are polarized perpendicular to each other (Since $\left|\vec{M}^1\right| = \left|\vec{M}^2\right|$).

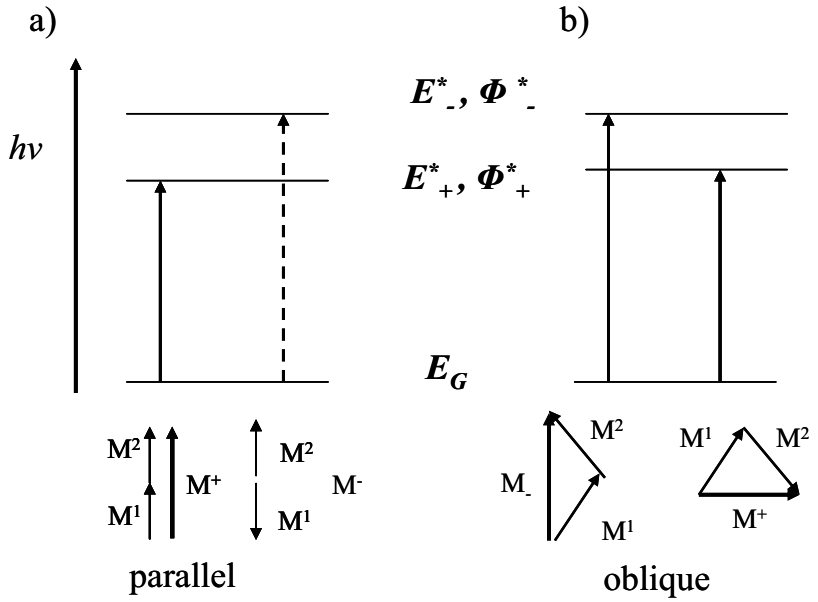

Fig. 3.12: Scheme of the Davydov shifted energy levels. a) A parallel orientation of the transition dipoles leads to a single red or blue shifted absorption line. The transition into the other Davydov component is forbidden (dotted line). b) A non-parallel orientation, shown at the right, results in two allowed transitions which are polarized perpendicular to each other.

The magnitude of I_{12} can be approximated as dipole interaction of the transition dipole moment of the excited molecule with the neighboring molecules in the ground state. See equ. 3.12 with M^i the transition dipole moment of the optical transition of the molecule and $R_{1,2}$ the distance between molecule 1 and 2.

$$I_{12} \propto \frac{M^i}{R_{1,2}^3}$$

equ. 3.12

The value of I_{12} ranges for optical singlet transitions normally between 10 cm^{-1} and 100 cm^{-1}. The measurement of the dimer spectra can be used to study the resonance interaction if the distance and orientation of the molecules is known. This can be realized with mixed single crystals of deuterated and non-deuterated molecules [69]. They intermix at all ratios, have the same crystal structure, but the optical transition have an offset of about 100 cm^{-1} which prevents the resonance interaction between deuterated and non-deuterated molecules. With increasing concentration of molecules in the deuterated matrix it is possible to measure the monomer, dimer, and crystal absorption spectra with known molecular orientation.

3.4.3 Christiansen effect

The *Christiansen* effect is a wavelength dependent scattering effect [70, 71, 72]. It is important for samples with strong differences in the index of refraction between sample and substrate material. In our case it is the difference in the index of refraction between organic thin film, silicon substrate and the surrounding vacuum. The effect increases with increasing roughness of the interface (Mie scattering [73]). It can alter the apparent position of absorption lines since anomalous dispersion is observed around all strong absorption lines (Fig. 3.13 a). A match of the sample and substrate index of refraction leads to a decrease of the scattering on one side of the absorption line (in this example low energy side), whereas the scattering becomes stronger at frequencies with increased refractive index difference (high energy side). This leads, in this example, to an effective blue shift of the apparent absorption line compared to the natural line position (blue in Fig. 3.13 b).

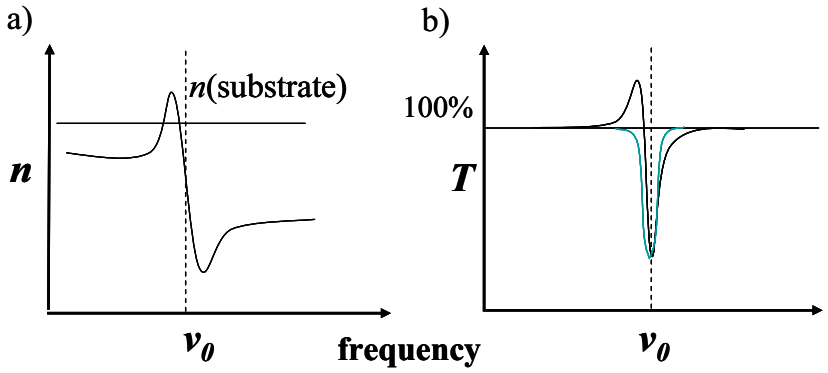

Fig. 3.13: Christiansen effect: a) Index of refraction at a strong absorption line shows anomalous dispersion. b) Frequency dependent scattering results in the typical apparent asymmetric absorption bands which differ from the symmetric natural absorption band (blue line).

3.4.4 Fourier transform infrared spectroscopy

3.4.4.1 Principles

Most modern commercial infrared spectrometer are Fourier-transform spectrometers. Instead of monochromators with dispersive elements normally used in the UV/VIS range, the major part of a FTIR spectrometer is a Michelson interferometer (See Fig. 3.14). In Michelson interferometers the incoming beam is divided by a beam splitter into beam I and II. After the reflection at mirror I and

II, the beams are united by the beam splitter, pass the sample and superimposed on to the detector. The path length difference x between the two beams is $x = 2\, x_{\text{mirror}}$, x_{mirror} is the displacement of mirror II.

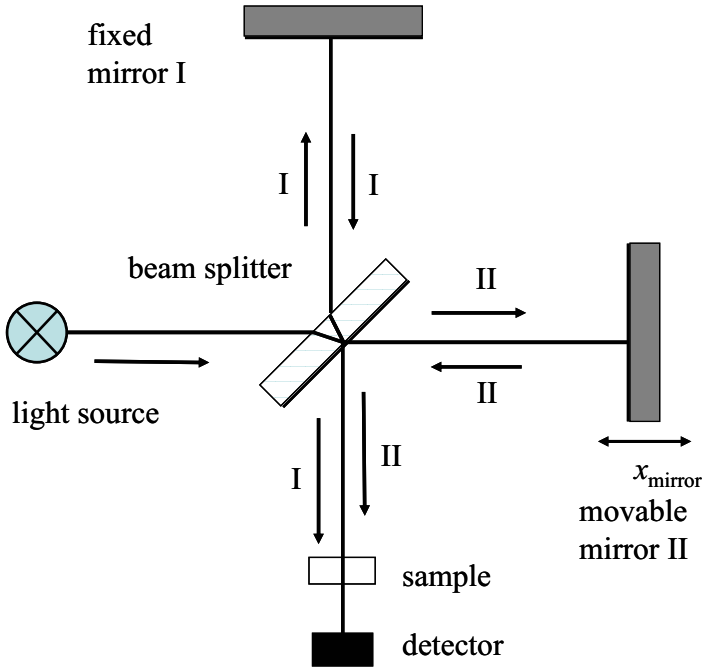

Fig. 3.14: Michelson interferometer: The light from the source is split into beam I and beam II, reflected by mirror I and II and superimposed at the beam splitter passes the sample to the detector. The difference in path length between beam I and II can be changed by moving mirror II.

I begin the detailed discussion [73] with the interference of two electro magnetic waves $E_{1/2}$ with frequency $\omega_{1/2}$, wave number $\nu_{1/2}$, path length $r_{1/2}$ and electric field amplitudes $\hat{E}_{1/2}$ at the detector.

equ. 3.13
$$E_{1/2} = \hat{E}_{1/2} \sin(\omega_{1/2} t - 2\pi \nu_{1/2} r_{1/2})$$

The electrical field at the detector is $E_D = E_1 + E_2$. Since the detector signal is proportional to the time averaged square of the wave amplitude $\langle E_D^2 \rangle$.

equ. 3.14
$$I = \varepsilon c \left\langle E_D^2 \right\rangle = \varepsilon c \left\{ \left\langle E_1^2 \right\rangle + \left\langle E_2^2 \right\rangle + 2 \left\langle E_1 E_2 \right\rangle \right\} = I_1 + I_2 + I_{12}$$

with

$$I_{12} = 2\varepsilon c \left\langle E_1 E_2 \right\rangle =$$
$$2\varepsilon c \hat{E}_1 \hat{E}_2 \left\langle \cos((\omega_1 - \omega_2)t + 2\pi(\nu_1 r_1 - \nu_2 r_2)) - \cos((\omega_1 + \omega_2)t + 2\pi(\nu_1 r_1 + \nu_2 r_2)) \right\rangle$$

The interference of two waves with different frequencies $\omega_1 \neq \omega_2$ leads to $I_{12} = 0$ since both cosine terms are time dependent and average to zero. For $\omega_1 = \omega_2$ and therefore $\nu_1 = \nu_2$ the first cosine term becomes time independent and results in.

equ. 3.15
$$I_{12} = 2\varepsilon c\hat{E}_1\hat{E}_2\cos(2\pi\nu(r_1 - r_2))$$

In the Michelson interferometer is $\varepsilon c\hat{E}_1\hat{E}_1 = I_1 = I_2 = S(\nu)$ and $r_2 = r_1 - x$ with $x = 2x_{mirror}$. For monochromatic light equ. 3.14 results in:

equ. 3.16
$$I_\nu(x) = 2S(\nu)(1 + \cos(2\pi\nu x))$$

The interferogram of light with a single frequency results in a cosine wave. This effect is used to monitor the mirror position with the help of a HeNe laser beam where each intensity maximum indicates a path difference of $x = \lambda_{HeNe} = 632$ nm. A continuous light source results in the following detected intensity.

equ. 3.17
$$I(x) = \int_0^\infty I_\nu(x)d\nu = \int_0^\infty S(\nu)d\nu + \int_0^\infty 2S(\nu)\cos(2\pi\nu x)d\nu$$

The first term is x independent and is the total intensity of all spectral components, the second term $I(x)$, called interferogram, is x dependent.

equ. 3.18
$$I(x) = \int_0^\infty S(\nu)\cos(2\pi\nu x)d\nu$$

The frequency spectrum $S(\nu)$ can be calculated from the measured interferogram $I(x)$ via inverse Fourier transformation.

equ. 3.19
$$S(\nu) = \int_0^\infty I(x)\cos(2\pi\nu x)dx$$

The resolution of a Fourier spectrometer can be estimated in the following way [74]. The source has two sharp emission lines λ_1 and λ_2 which are to resolve. Their interferogram is calculated in equ. 3.20 and plotted in Fig. 3.15.

equ. 3.20
$$I(x) = A(\cos(2\pi\nu_1 x) + \cos(2\pi\nu_2 x)) = 2A\cos(2\pi x\frac{(\nu_1 + \nu_2)}{2})\cos(2\pi x\frac{(\nu_1 - \nu_2)}{2})$$

To resolve both frequencies it is necessary to capture at least the first beat period x_{max} (equ. 3.21). For a higher resolution it is therefore necessary to capture a larger part of the interferogram.

$$x_{\max} = \frac{2}{(\nu_1 - \nu_2)} = \frac{2}{\Delta\nu}$$

$$\Delta\nu = \frac{1}{x_{mirror}}$$

equ. 3.21

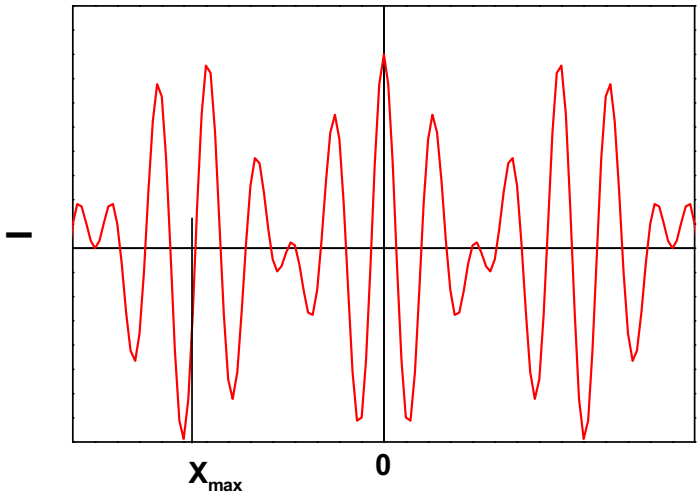

Fig. 3.15: Interferogram of two emission lines with wave numbers ν_1 and ν_2. It is necessary to evaluate the interferogram until the first beat maximum x_{max} to resolve the two sharp emission lines.

Since the interferogram can only be sampled at discrete steps and with limited path difference x_{max}, it is necessary to use the discrete Fourier transformation (DFT) equ. 3.22. The interferogram is sampled at equidistant steps $x = n\Delta x$. The inverse Fourier transform is shown in equ. 3.23. The spacing of the data points in frequency and real space are connected by equ. 3.24. The picket-fence-effect causing the apparent shift of an absorption line, if it is located between two sampling points in the frequency domain, can be suppressed by the so called Zero filling.

Zero filling means to at least double the interferogram size by adding zeros at interferogram tails. This increases the data points in the frequency domain and leads to a smother look of the spectrum. It is important that zero filling just increases the computation time but does not alter line shape nor creates artifacts.

Another problem which can arise from a too coarse sampling distance Δx is the so called aliasing [75]. Due to the symmetry of equ. 3.22, the DFT results in a superposition of the spectra S(kΔν) and its mirror image S((N-k)Δν). The spectrometer software normally deals with this problem. It has just to be taken care of that the intensity of the high frequency tail in the single channel spectrum (Fig. 3.16) is decayed, otherwise this tail is the superposition of the two spectra.

$$S(k \cdot \Delta\nu) = \sum_{n=0}^{N-1} I(n \cdot \Delta x) \exp(i 2\pi nk / N)$$

equ. 3.22

$$I(n \cdot \Delta x) = (\frac{1}{N}) \sum_{k=0}^{N-1} S(k \cdot \Delta\nu) \exp(-i 2\pi nk / N)$$

equ. 3.23

$$\Delta\nu = \frac{1}{N \cdot \Delta x}$$

equ. 3.24

Δx is normally given by the wave length of the HeNe laser λ_{HeNe} = 632 nm used for measuring mirror position. To save computation time the Fast Fourier transform (FFT) algorithm is used and restricts that the total number of sample points N is a power of two.

The increase of the path difference x_{max} to increase the resolution has the following experimental limitations:

1. The amplitude of the oscillation decreases very fast with x so the signal to noise ratio becomes weak. It is therefore necessary that the used detectors have a very large dynamic range and a good S/N ratio.
2. x_{max} is limited by the thickness d of the substrates used for the films [76].

A single channel spectrum (transmitted intensity in dependence of the wavenumber) of a 0.5 mm Si wafer taken with 2 cm^{-1} resolution exhibits regular oscillations (Fig. 3.16). The corresponding interferogram (Fig. 3.17) shows a second (ghost) burst peak. From equ. 3.22 it is deducible that a sharp peak in the interferogram $I(x = x_p)$ results in an oscillation in frequency spectra $S(\nu) = I(x_p) \exp(i 2\pi x_p \cdot \nu / N)$ which is observable in Fig. 3.16.

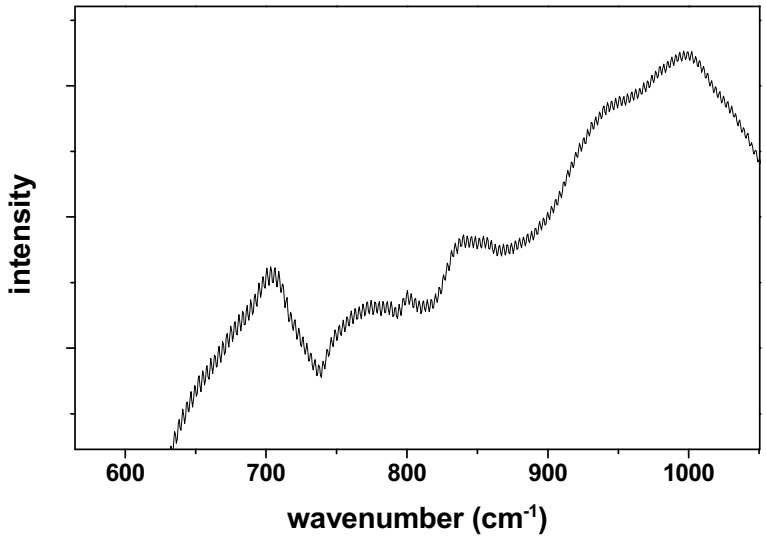

Fig. 3.16: Single channel spectrum (transmitted intensity in dependence of the wavenumber) of a 0.5 mm SiO_2 waver taken at 2 cm^{-1} resolution. Mind the oscillation which is not noise.

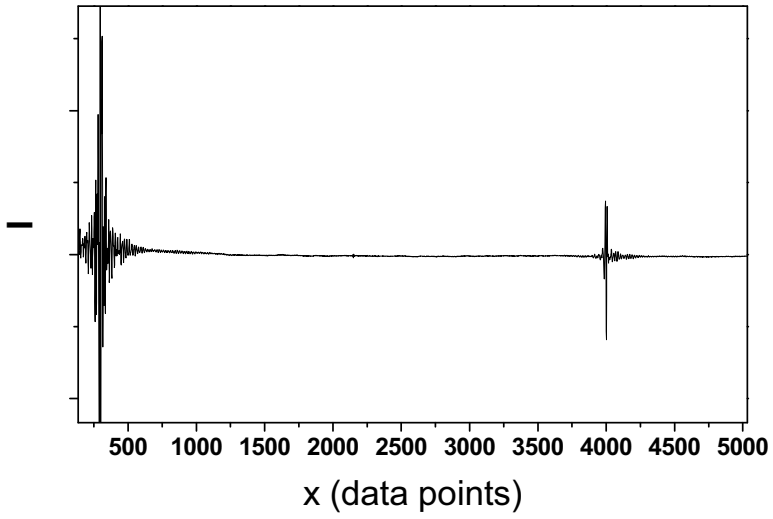

Fig. 3.17: Interferogram of a of a 0.5 mm SiO_2 waver taken at 2 cm^{-1} resolution. Mind the ghost peak at 4000 points.

This ghost burst peak can be explained by internal reflections of IR beam in the planar Si substrate. (Fig. 3.18). The light of the reflected beam *II* has the extra optical path $\Delta x_{sub} = 2\, n_{IR}\, d$, with n_{IR} refractive index, d thickness of the substrate, and interferes therefore constructive when beam *I* has a delay of $x = \pm\Delta x_{sub}$. This effect can be used [77] to measure the thickness d of the substrate. The positions

of two oscillation maxima are ν_1, ν_2, the IR refractive index is n_{IR}, and *m* is the number of oscillations between ν_1 and ν_2.

equ. 3.25
$$d = \frac{m}{2}\frac{1}{\nu_1 - \nu_2}\frac{1}{n_{IR}}$$

To be able to obtain spectra with a resolution of 2 cm^{-1} it is necessary to use custom made 1.5 mm thick Si wafer as substrates.

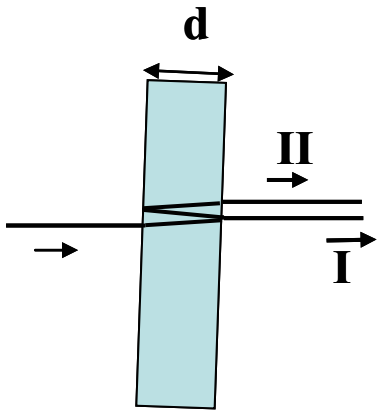

Fig. 3.18: Substrate dependence of the possible x_{max}. The light beam is split into beam *I* and *II* due to internal reflection. They have a path length difference of $\Delta x_{sub} = 2n_{IR}\,d$ with *d* the substrate thickness and n_{IR} the IR refraction index. The interference of beam *I* with beam *II* causes an ghost peak at $\pm\Delta x_{sub}$.

3.4.4.2 Setup

In this work an IFS 66v/s FTIR spectrometer by Bruker Optics was used. The whole path of rays was evacuated to about 1 mBar 10 min before the begin of the measurements, to reduce water and CO_2 absorption lines. A glow bar was used as light source, a liquid nitrogen cooled mercury cadmium telluride (MCT) diode served as detector. The optical setup consisted of *KBr* beam splitter and windows. The spectral range was 0 cm^{-1} - 4000 cm^{-1} (it should be mentioned that a larger spectral range should be used to prevent the aliasing effect [75]), the resolution was 2 cm^{-1}. 4000 scans were averaged for one spectrum. As substrate 1.5 mm thick Si wafers with native oxide layer (Siegert Consulting) were used.

3.5 X-ray diffraction

X-ray diffraction was used in this work on a basic level and therefore only the basic concepts are here explained here. The principle explanation for the diffraction of X-ray beams was given by W. L. Bragg. (Fig. 3.19). An incident monochromatic plane wave is elastically diffracted by parallel crystal lattice planes with an inter-planar distance d_{hkl}. The waves can only interfere constructively if the path difference of $2\delta = 2d_{hkl}\,sin(\theta)$ is an integral multiple of the incidence wavelength λ. This is denoted as Bragg's law (equ. 3.26) where n is an integer number.

equ. 3.26
$$n\lambda = 2d\sin(\theta)$$

Synchrotron radiation with a wavelength of 0.11808 nm as well as Cu K_α radiation of 0.1542 nm was used. *Bragg's law* correlates the wavelength to lattice spacing and the diffraction angles. To be independent from the wave length λ of the used radiation the scattered intensity is plotted in dependence of vector of momentum transfer $\vec{q}$ instead of the angle θ.

equ. 3.27
$$q = \frac{4\pi}{\lambda}\sin(\theta)$$

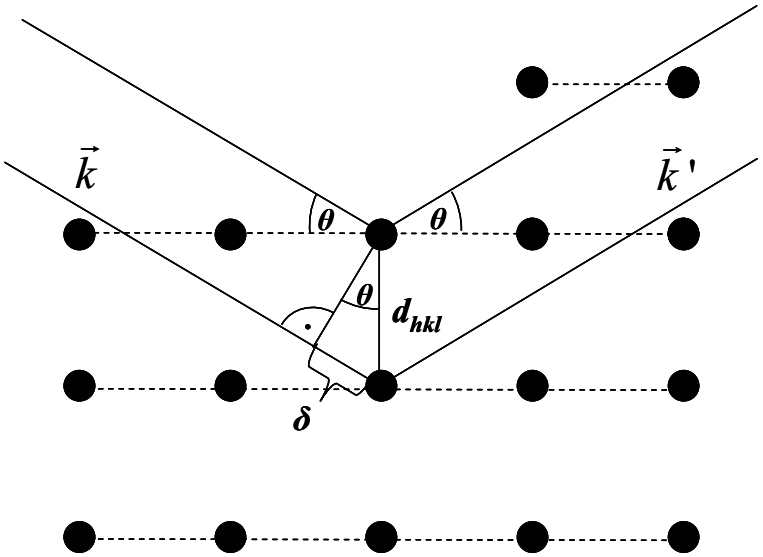

Fig. 3.19 The incoming X-rays with wave vector $\boldsymbol{k}$ are scattered by lattice planes with inter-planar distance d_{hkl}. The path difference between two beams $\boldsymbol{k'}$ scattered by neighboring planes is $2\delta = 2d_{hkl}\,sin(\theta)$.

A different description of the X-ray diffraction phenomenon is given by the Laue Bragg equations. An incoming plane wave with wave vector $\vec{k}$ is elastically scat-

tered into spherical waves by the atoms of a Bravais lattice. These spherical waves can only interfere constructively into a reflected plane wave with $\vec{k}'$, if the spherical waves have the same phase for very point of the Bravais lattice. This is only the case if the vector of momentum transfer $\vec{q} = \vec{k}' - \vec{k}$ fulfills equ. 3.28 for every the Bravais lattice vectors $\vec{R}$.

equ. 3.28 $$e^{i\vec{q}(\vec{r}+\vec{R})} = e^{i\vec{q}\vec{r}} \Rightarrow e^{i\vec{q}\vec{R}} = 1$$

Most notably, this condition is only fulfilled if $\vec{q}$ is a reciprocal lattice vector $\vec{K}$. In general, reciprocal lattice vectors are surface normals of the lattice planes of the direct lattice. They can be used to identify these planes using the notation of the Miller indices *h,k,l* taking into account the primitive vectors of the reciprocal lattice $\vec{b}_1, \vec{b}_2, \vec{b}_3$ and the integer indices *h,k,l*. $\vec{K} = h\vec{b}_1 + k\vec{b}_2 + l\vec{b}_3$.The distance between the planes is herein given by $d_{hkl} = \left|\frac{2\pi}{\vec{K}}\right|$. From equ. 3.27 and equ. 3.28 it can be deduced that $\vec{d}_{hkl}(\vec{k}' - \vec{k}) = 2\pi n$ is equivalent to the Bragg law.

In the general case of structures that do not exhibit single atoms at their lattice points, the scattered amplitudes depend on the *inner* structure of the unit cell, as it is intrinsically the case for (organic) molecular crystals. This property is described by the structure factor which is the Fourier transformation of the electron density $\rho(\vec{r})$ within the unit cell. *e* is the elementary charge.

equ. 3.29 $$F(\vec{k}) = -\frac{1}{e}\int d\vec{r} e^{i\vec{k}\vec{r}} \rho(\vec{r})$$

The scattering amplitude *A(q)* results from the sum of all unit cells in the crystal, where $\vec{a}_i$ are the base vectors of the lattice and A_e is the scattering amplitude of an electron.

equ. 3.30 $$A(\vec{q}) = A_e F(\vec{q}) \sum_{u,v,w} e^{i\vec{q}(u\vec{a}_1 + v\vec{a}_2 + w\vec{a}_3)}$$

The structure factor takes into account the symmetry operations of the unit cell, which may lead to the suppression of diffraction peaks.

3.5.1 Specular XRD

The method of *specular XRD* or *θ-2θ* XRD probes exclusively the periodicities parallel to the substrate surface. (Fig. 3.20 a). The plane of incident and reflected

beam is oriented perpendicular to the substrate surface and the reflected beam is detected at the same angle θ as the incident beam.

3.5.2 Kiessig fringes

In specular XRD scans on films with smooth surfaces internal reflections between the interfaces film/substrate and film/air may occur. Similar to *Bragg's law* we face constructive interference for the following conditions with D being the film thickness and n being an integer number.

$$n\lambda = 2D\sin(\theta) \qquad \text{equ. 3.31}$$

This results in the so-called Kiessig fringes which are only observable on films with very smooth interfaces. In the plot of the specular XRD scan (Fig. 3.21) they are located next to the totally reflected beam and can be used to derive the thickness D of the organic film where ΔK is the distance between two Kiessig fringes.

$$D = \frac{2\pi}{\Delta K} \qquad \text{equ. 3.32}$$

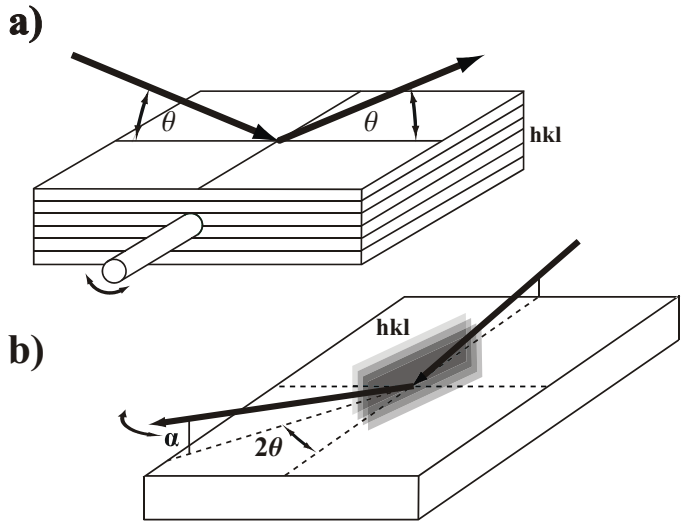

Fig. 3.20: a) Specular or θ-2θ X-ray diffraction geometry which probes lattice planes parallel to substrate surface. b) In-plane XRD geometry in which the X-ray beam is diffracted at lattice plane almost perpendicular to the substrate surface and then total internal reflected if α is smaller than the critical angle of internal reflection.

3.5.3 Laue oscillation

Since real structures like thin films have a finite thickness only a limited number N of lattice planes contributes to the diffraction. It is possible to calculate the resulting intensity as superposition of the waves scattered by each lattice plane. From Fig. 3.19 the path difference between two planes is $2d\ sin(\theta)$ leading to a phase shift of $\Phi = 2d\ sin(\theta)\ 2\pi/\lambda = q_z\ d$. The summation over all scattering planes results in:

equ. 3.33

$$E = \sum_{i=1}^{N} E_i = E_0(1 + e^{i\Phi} + e^{i2\Phi} + .. + + e^{i(N-1)\Phi})$$
$$= E_0 \frac{e^{iN\Phi/2}}{e^{i\Phi/2}} \frac{e^{-iN\Phi/2}}{e^{-i\Phi/2}} \left(\frac{1 - e^{iN\Phi}}{1 - e^{i\Phi}} \right) = E_0 e^{i(N-1)\Phi/2} \frac{\sin(\Phi N/2)}{\sin(\Phi/2)}$$

Since the detection process is limited to intensities, the signal is proportional to:

equ. 3.34

$$I \sim |E|^2 = |E_0|^2 \frac{\sin^2(\Phi N/2)}{\sin^2(\Phi/2)}$$

The intensity pattern has minima at a phase of $\Phi = 2\pi/N = q_z d$ resulting in Laue-oscillations with separation ΔL. (Fig. 3.21) The number of coherently scattering planes can be calculated with equ. 3.35.

equ. 3.35 $$\Delta L = \frac{2\pi}{dN} \Rightarrow N = \frac{2\pi}{d\Delta L}$$

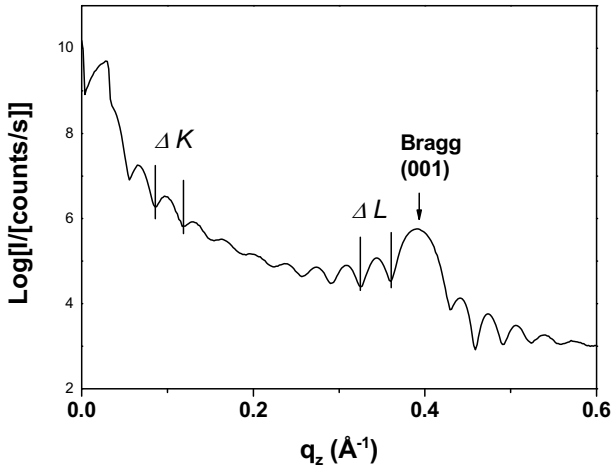

Fig. 3.21: Specular XRD scan of a 20 nm thick 4T/PEN film on SiO_2. *⊿K* denotes the Kiessig fringes, *⊿L* the Laue oscillations.

3.5.4 In-plane XRD

The technique of *Grazing incidence* or in-plane XRD combines diffraction on lattice planes almost perpendicular to the substrate surface with the total external reflection of the X-rays on the sample surface. (Fig. 3.20 b). This is possible since the X-ray refraction index of solids is slightly smaller than 1 and the angle *a* between incident beam and surface is smaller than the critical angle of total external reflection. The penetration depth of the X-rays into the sample ranges typical from 1 μm to 1 nm. In-plane XRD is therefore a very powerful tool to study very thin films.

3.6 Organic thin film transistors

In this work OFETs with three geometries were used. The devices were prepared by Ph.D. Piero Cosseddu in the group of Prof. Annalisa Bonfiglio at the Department of Electrical and Electronic Engineering of the University of Cagliari. The organic films were deposited in our lab in Berlin and the electrical measurements were performed back in Italy. All devices had a channel length *L* of 50 μm and channel width *Z* of 5mm (Fig. 2.8).

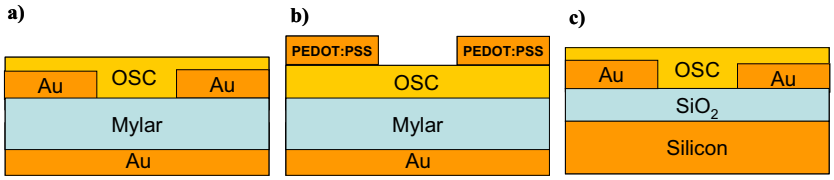

Fig. 3.22: OFET structures: a) bottom gold contacts on Mylar b) PEDOT:PSS top contacts. The Mylar acts as gate dielectric between OSC and gold gate. c) gold bottom contacts on silicon oxide. The 500 nm SiO_2 layer acts as gate dielectric and the heavily doped Si Wafer as gate electrode.

3.6.1 OFET on Mylar

I first start with the OFET realized on a 1.6 μm thick poly(ethylenetherephtalate) (PET) foil (Mylar, Du Pont) [78]. This material has a dielectric constant similar to SiO_2 ($\varepsilon_r \approx 3.0$), a high resistivity and a low permeability to oxygen, hydrogen, CO_2, and water. The freestanding foil served as gate dielectric and supporting layer. The foil was spanned on a metal ring of 1.5 cm diameter and fixed with *parafilm*. (See Fig. 3.23). A gold gate electrode is applied by vacuum evaporation through a shadow mask. The source and drain gold contacts are produced by standard photolithographic processes [60]. After the realization of all the required electrodes the organic semiconductor layer was deposited on top of source and drain electrodes. (C.f. Fig. 3.22 a) and Fig. 3.23.)

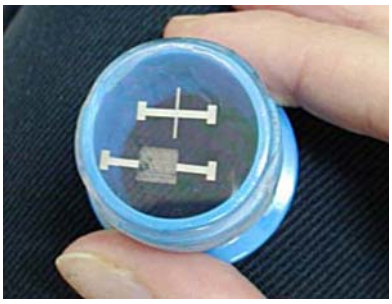

Fig. 3.23: Realization of two gold bottom contact OFETs on Mylar. Image taken from [60].

For top contact devices (Fig. 3.22 b) the organic layer is deposited on top of the substrate foil just after preparing the gold gate electrode. In this case, source and drain contacts were made out of poly(ethylene dioxythiophene):poly(styrene sulfonate) (PEDOT:PSS,Baytron P CPP 105D: H.C. Stark), and were patterned by means of soft lithography micro contact printing technique [79] on top of the organic layer. In this technique (Fig. 3.24) a thin film of PEDOT:PSS is spin casted on a stamp out of polydimethylsiloxane (PDMS) which prints a positive image of the source and drain contacts. The stamp is then brought in contact with the organic layer and the PEDOT:PSS is transferred from the stamp to the device only at places where the stamp has elevated features.

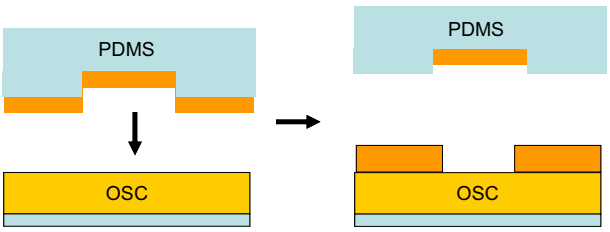

Fig. 3.24: Micro contact printing by soft lithography: A thin film of PEDOT:PSS is spin casted on the PDMS stamp and than printed on the organic semiconductor layer.

3.6.2 OFET on Silicon

Bottom contact OFETs were realized on highly doped silicon wafers acting as gate electrode with a 500 nm thermally grown silicon oxide layer acting as gate dielectric. (See Fig. 3.22 c). By means of the usual photolithographic processes gold source and drain electrodes were realized with a channel length $L = 50$ µm and channel width $W = 5$mm.

3.6.3 Electrical characterization

The electrical measurements were carried out with an Agilent HP 4155 Semiconductor Parameter Analyzer. A probe station with gold tips was used to contact the electrodes. The measurements were performed at room temperature under ambient conditions and under a controlled nitrogen atmosphere (0.1 ppm O_2). To investigate the role of oxygen doping part of the devices were annealed under a controlled atmosphere (0.1 ppm O_2) at a temperature of 120 °C. The electrical characterization was then performed after cooling the devices down to room temperature.

4. Results and discussion

The aim of this work is to reveal which molecular properties lead to phase separation or mixing of two kinds of rod-like conjugated molecules. For a systematic study of this question five different rod-like conjugated molecules were co-deposited: α-quaterthiophene (4T), pentacene (PEN), p-sexiphenyl (6P), α-sexithiophene (6T), and its alkylated analogue α,ω-dihexylsexithiophene (DH6T). With these five molecules that can be regarded as standard materials in the context of organic electronics it is possible to realize pairs of materials which differ in the parameters: monomer type, length of the conjugated core (CC), and overall molecular length. The film morphology of each material pair will be discussed separately. I will begin with the films grown on silicon oxide followed by certain 6T/DH6T films grown on Mylar. The attributes leading to mixing or phase separation will be discussed in the conclusion. In the last part of the result section I will describe the realization of organic field effect transistors (OFET) which are a tool for the characterization of the organic film mobility μ and an example for possible applications for the studied material systems.

4.1 Thin films on silicon oxide

In this chapter I present a detailed analysis of co-deposited film on silicon oxide. I produced for every material pair several films with 30 %, 50 %, and 70 % mixing ratio in terms of the number of molecules. For every mixing ratio films of 4.5 nm, 20 nm, and 40 nm thickness were produced. For special cases, in which the growth mode of the initial layer was interesting also sub mono layer films with 1.2 nm thickness were produced. All together over 350 samples have been produced and analyzed for this study. The molecule pairs are grouped according to the length of there conjugated core, since this seems to be, at the first glance, a k.o. criteria for the formation of mixed crystals of two different rod-like conjugated molecules.

4.1.1 Similarly sized conjugated cores

I start with molecule pairs which have similarly sized conjugated cores.

4.1.1.1 4T / PEN

I begin with the discussion of the results of the 4T/PEN material pair. The van der Waals lengths (vdWL) of 1.82 nm (4T) [29] and 1.64 nm (PEN) [22] differ by

0.18 nm (10 %), calculated from reported crystal structures with a hydrogen van der Waals radius of 0.12 nm. On insulators, both molecules exhibit the well-known thin film growth behavior of in layered structures with the long molecular axis standing almost perpendicular to the substrate surface. This can be seen in the AFM height image of 4T film growing in the Volmer-Weber (island) growth mode with well separated islands [80] (Fig. 4.1 a) and PEN growing in the layer-plus-island mode [81] (Fig. 4.1 c). Remarkably, the co-deposited 4T/PEN film (Fig. 4.1 b) also shows a layered surface morphology. The surface is less corrugated (~7 layers) compared with the pure 4T (~13 layers) and PEN (~12 layers) films. No phase separation into different material domains can be observed *via* AFM for mixing ratios of 11 % to 90 % 4T.

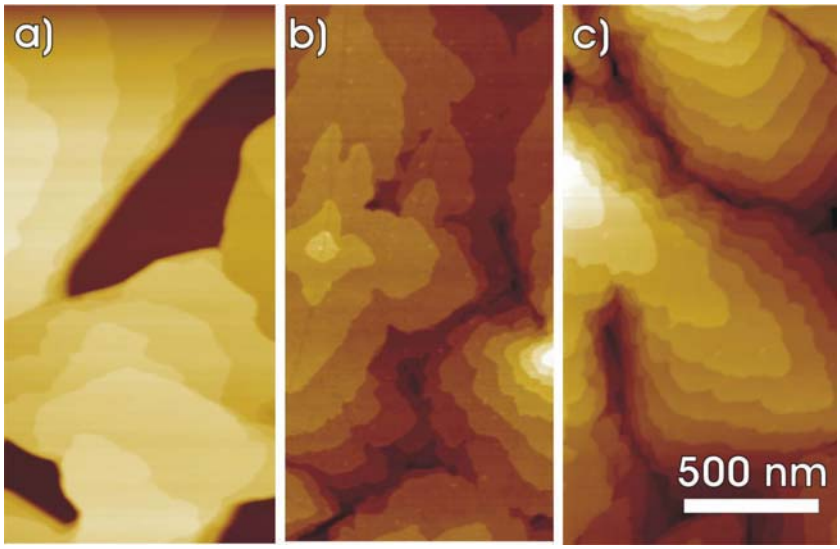

Fig. 4.1: AFM height images of 20 nm thick films deposited on SiO_2. a) 4T, b) co-deposited 4T/PEN with 42 % 4T and c) PEN. The measured step heights d are (1.50 ± 0.06) nm (4T), (1.56 ± 0.06) nm (4T/PEN) and (1.51 ± 0.06) nm (PEN).

The average interlayer step height d measured by AFM is the same (in the error margin) for the mixed film (1.56 ± 0.06) nm, the pure 4T (1.50 ± 0.06) nm, and PEN (1.51 ± 0.06) nm films. In order to probe the bulk interlayer spacing of the films, specular X-ray diffraction scans (Fig. 4.2) were performed on the pure material and co-deposited 4T/PEN samples. The specular XRD scan of the pure 4T film exhibits peaks at values of q_z = 0.4083 Å^{-1}, q_z = 0.8233 Å^{-1}, and q_z = 1.2196 Å^{-1} vertical momentum transfer, which we assign to the (0 0 l) reflections of a polymorph with d = (1.53 ± 0.01) nm, which is very similar to the LT-4T [18] (low temperature) polymorph of 4T with d = 1.52 nm. The pure

PEN film shows peaks at q_z = 0.4064 Å^{-1}, q_z = 0.8138 Å^{-1}, and q_z = 1.2196 Å^{-1} yielding d = (1.5 4 ± 0.01) nm. I assign them to the (0 0 *l*) reflections of the TF-PEN [20] (thin film) polymorph with an interlayer spacing of d = (1.54 ± 0.01) nm. The 4T / PEN co-deposited films with 63 % 4T and 30 % 4T exhibit peaks at q_z = 0.3913 Å^{-1}, q_z = 0.792 Å^{-1} and q_z = 1.1874 Å^{-1}. The (0 0 *l*) Bragg peaks can be assigned to a layered structure with d = (1.59 ± 0.01) nm. A 46 % 4T film measured *in-house* yielded d = (1.58 ± 0.03) nm (not shown).

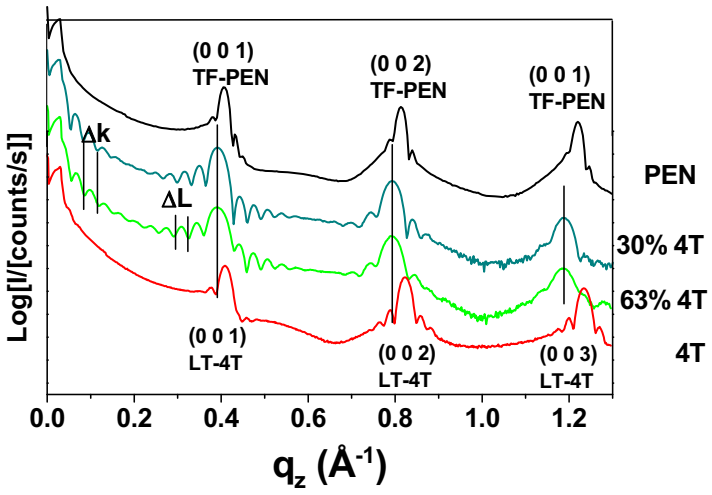

Fig. 4.2: Specular X-ray diffraction spectra of co-deposited PEN/4T film of 20 nm thickness on SiO_2. Δk is the interval of the Kiessig fringes and ΔL is the interval of the Laue oscillations.

This interlayer spacing is in good agreement with the step height measured by AFM and is, to my knowledge (Table 1), dissimilar to all 4T and PEN polymorphs. The existence of Kiessig fringes [82, 83] with Δk = 0.0308 Å^{-1} indicates that the mixed films are less corrugated than the pure 4T and PEN films (in agreement with AFM data) and have a thickness of 20 nm, which is identical to the nominal mass thickness of the film measured by the microbalance. The Laue oscillations [82, 83] with ΔL = 0.036 Å^{-1} indicate that the coherence length of the scattering crystallites is about 18 nm, i.e. it almost equals the nominal film thickness. This indicates that the co-deposited film is of high structural order. A phase separation into crystalline compounds can be excluded, because this would result in an overlap of different Bragg peaks, which is not the case. Also a separation into crystalline and amorphous phases would lead to a decrease in the z-extension of the scattering planes, which would result in a reduced coherence length observable by the Laue oscillations.

Table 1: Interlayer distance *d* of the 4T/PEN film compared with known PEN and 4T polymorphs. The measured *d* does not coincidences with any known 4T and Pentacene polymorph.

polymorph	*d* (nm)
66 %; 33 % 4T/PEN	1.59
PEN bulk [21]	1.45
PEN TF [20, 23, 24, 25]	1.54
PEN *Holmes* [26]	1.41
PEN *Minakata* [27]	1.50
4T HT [84]	1.43
4T LT [84]	1.52

To gather information about the local environment of the molecules, Fourier transform infrared absorption spectroscopy (IR) is performed on the respective films. The IR spectra of the pure 4T film (Fig. 4.3) shows a Davidov split peak [85] with the two peak maxima centered at 688.1 cm^{-1} and 702.4 cm^{-1}, which is associated with the $\gamma(C_\alpha\text{-H})$ out-of-plane (o.-o.-p.) [84] vibration of the hydrogen atoms at the end positions of the 4T molecule. In a co-deposited film with 63 % 4T, the Davidov splitting vanishes and a single peak appears centered at 691.9 cm^{-1}. This indicates that the molecular occupation of the crystal unit cell (in-plane structure of the co-deposited film) changed significantly. Note: I will show later in this thesis, that in phase separated films (i.e. 4T/DH6T film, section 4.1.4.1) the Davydov splitting of the peak prevails. This change of the local environment of the 4T molecules is also supported by the 4.6 cm^{-1} red shift of the $\gamma(C_\beta\text{-H})$ vibration [84] at 797.6 cm^{-1} associated with the hydrogen atoms at the β-positions of the 4T thiophene rings.

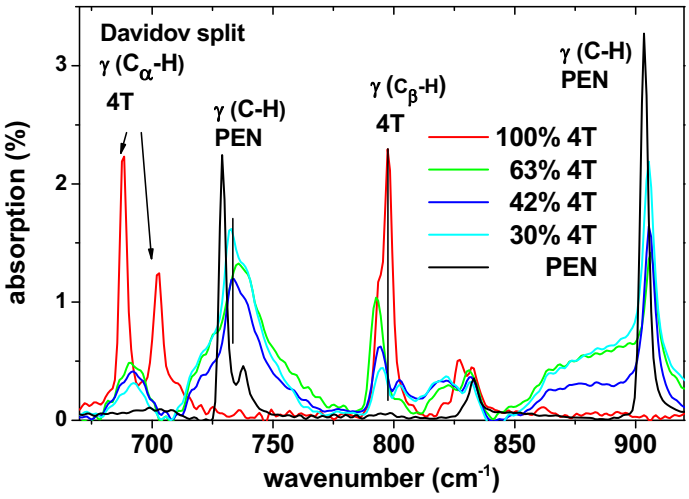

Fig. 4.3: IR absorption spectra of the γ (C-H) out-of-plane bending region of co-deposited 4T/PEN films on SiO_2.

I will now discuss the peak shifts of the PEN molecules caused by the co-deposition. The γ(C-H) o.-o.-p. vibration [86] of the pure PEN film at 729 cm^{-1} shows strong broadening and a maximal blue shift of 8 cm^{-1} in the 63 % 4T film. The increase of the broadening with decreasing PEN content indicates that the local environment of the PEN molecules becomes less homogeneous. This points to statistical mixing of PEN and 4T molecules in the molecular layers. The blue shift of 2.4 cm^{-1} of the PEN γ(C-H) vibration at 903.5 cm^{-1} is also indicative of the change in the film structure compared to the pure PEN film. These strong changes in the IR spectra for 4T and PEN together with the layered growth (from AFM and XRD) give strong evidence for an intimate mixing of 4T and PEN on a molecular scale. A collective change of the tilt angle between the long molecular axis and the substrate surface could explain the increase of the inter-layer spacing (Fig. 4.4). This could also point to the conclusion that *d* is independent of the 4T/PEN mixing ratio in the measured range.

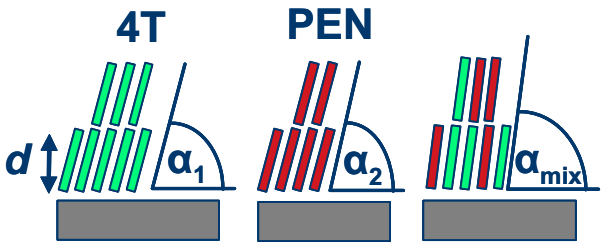

Fig. 4.4: Increase of the interlayer spacing *d* due to an increase of the tilt angle between long molecular axis and substrate in co-deposited 4T/PEN film. $\alpha_{mix} > \alpha_1, \alpha_2$.

4.1.1.2 6T / 6P

The vdWL of 6T [87] (2.61 nm) and 6P [88] (2.87 nm) differ by 0.26 nm (9 %), the absolute mismatch being 0.1 nm larger than for 4T/PEN. The AFM height image of the 6T/6P film (Fig. 4.5 b) shows layered structures similar to the 4T/PEN films. The pure 6T (Fig. 4.5 a) and 6P films (Fig. 4.5 c) exhibit their typical thin film morphology [87, 89] of layered structures. The co-deposited 6T/6P film with a 43 % 6T ratio exhibits an island density which is comparable to the 6P film. It is noteworthy that some edges of the islands enclose angles of (120 ± 20)°, similar to the angles found for the islands of the pure 6P film. This is an indication that the in-plane-ordering of the co-deposited film may be similar to that of the 6P film.

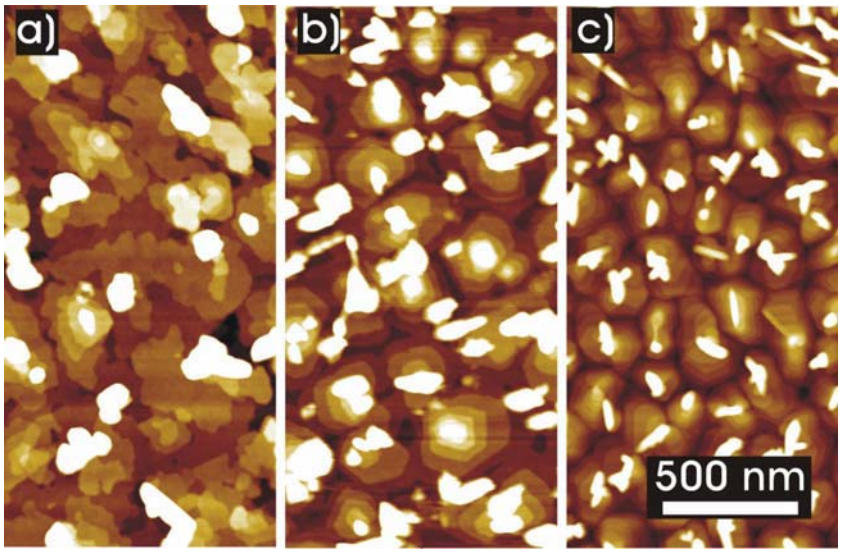

Fig. 4.5: AFM height images of 20 nm thick films deposited on SiO_2. a) 6T, b) co-deposited 6T/6P with 43 % 6T and c) 6P. The measured step heights *d* are 2.19 nm (6T), 2.57 nm (43 % 6T), and 2.69 nm (6P).

Next, the specular XRD scans (Fig. 4.6) are discussed, starting with the pure 6T film of 40 nm thickness. The 6T film exhibits sharp peaks of a (2n 0 0) series up to n = 6 leading to an interlayer distance of $d = (2.25 \pm 0.05)$ nm, similar to the LT-6T [90] (low temperature phase) ($d = 2.236$ nm) or γ-6T [91] phase ($d = 2.24$ nm). The series of broad peaks belonging to a spacing of $d = 2.42$ nm represents the β-phase [91] of 6T (2.44 nm).

The 74 % 6T film of 20 nm thickness shows - compared to the pure 6T film - weaker peaks of the (2n 0 0) series of the LT-6T [90] polymorph. The peaks at $q_z = 0.4715$ Å^{-1} and $q_z = 0.728$ Å^{-1}, marked with dashed lines, are assigned to contributions of a mixed phase with $d = (2.59 \pm 0.1)$ nm. The 40 nm 58 % 6T film exhibits a (h 0 0) series belonging to $d = (2.60 \pm 0.05)$ nm. The 52 % 6T (30 nm thick) and 42 % 6T (20 nm) films lead to interlayer spacings of $d = (2.62 \pm 0.05)$ nm and $d = (2.66 \pm 0.05)$ nm. The specular scan of a 26 % 6T film (40 nm) (not shown) measured *in-house* with Cu K_α radiation resulted in $d = (2.68 \pm 0.05)$ nm. The pure 6P (10 nm) film exhibits regular (0 0 l) peaks with $d = (2.74 \pm 0.05)$ nm similar to the γ-6P [92] phase with $d = 2.72$ nm.

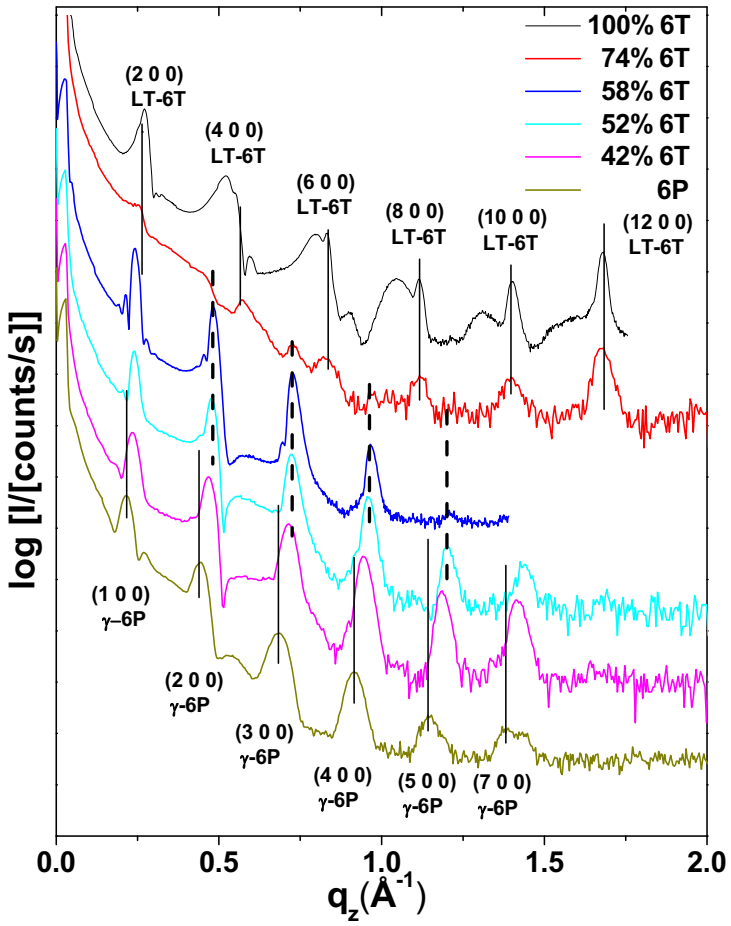

Fig. 4.6: Specular X-ray diffraction scans of co-deposited 6T/6P films on SiO_2. The thin solid lines mark the peaks of the (2n 0 0) series of the LT-6T polymorph and the (0 0 *l*) reflections of the γ-6P polymorph.

The interlayer spacing *d* and the step heights on the film surfaces measured by AFM are plotted in dependence of the 6T content in Fig. 4.7. From 0 % 6T to 60 % 6T content, *d* shows a weak monotone decreasing dependence on the mixing ratio. The specular scan of the 74 % 6T film shows the co-existence of a pure LT-6T phase and a mixed phase. I measured the step heights on individual islands of the 75 % 6T film *via* AFM. The step height cumulate at ~2.25 nm, which I associate to pure 6T islands and ~ 2.45 nm associated to a mixed phase. Both phases are observable in the specular XRD scan. Additional a broad distribution around 2.6 nm is observable which can be associated with 6P rich islands. It is to mention that is hard to measure the step heights of individual islands with high precision because of it small extension.

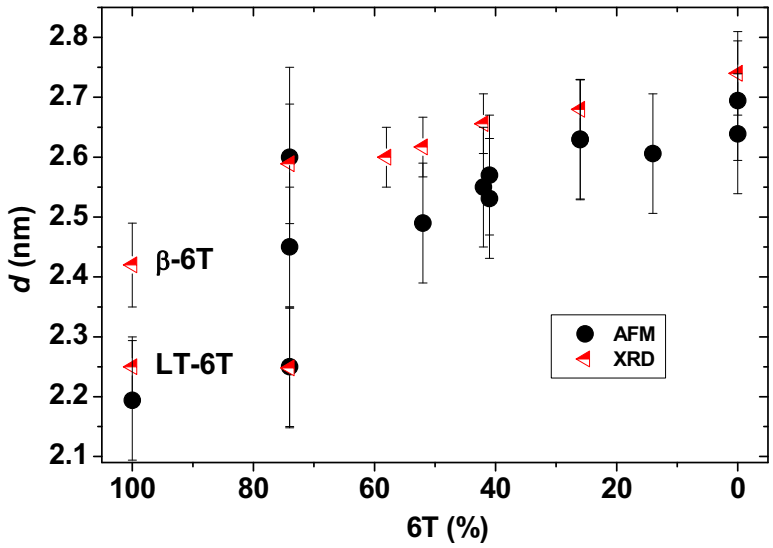

Fig. 4.7: Inter-layer distance *d* of co-deposited 6P/6T films on SiO_2 measured by AFM and XRD as a function of the 6T content.

Additional information about the local environment of the molecules in the film can be derived from IR spectroscopy (Fig. 4.8). First, the γ(C-H) o.-o.-p. vibration peaks [93] of the 6P molecules are addressed. The γ(C_α-H) vibration of the 6P-end-rings at 760 cm^{-1} exhibits a blue-shift of 3 cm^{-1} with increasing 6T content. The γ(C_p-H) vibration of the para-substituted rings shows a comparable blue-shift (2.9 cm^{-1}) from 814.2 cm^{-1} (6P) to 817.1 cm^{-1} (74 % 6T) film.

Remarkably, the γ(C_β-H) vibration peak [94] of the 6T molecule at 791.6 cm^{-1} loses its fine structure when a small amount of 6P is co-deposited. With further increase of the 6P content, this peak shows a pronounced blue-shift of 3.4 cm^{-1} (26 % 6T). Of particular importance is the Davidov split [85] 6T γ (C_α-H) o.-o.-p bending peak at 688 cm^{-1} and 702 cm^{-1}. The 74 % 6T film shows only a broad peak around 686 cm^{-1}, which is a superposition of the 6P δ(C_α-H) ring deformation vibration peak at 689.5 cm^{-1} and the non-splitted broad 6T γ(C_α-H) peak around 682.5 cm^{-1} that was measured for intercalated films of 6T/DH6T [95]. As discussed earlier in this work, the vanishing of this Davidov splitting indicates that the local environment of the 6T molecules changed suddenly with the co-deposition of 6P.

However, it is possible that the IR spectrum of the 74 % 6T film may contain a small contribution of the Davidov split 6T γ(C_α-H) peak and is therefore not in contradiction to the detection of pure 6T domains in the 74 % 6T film by XRD.

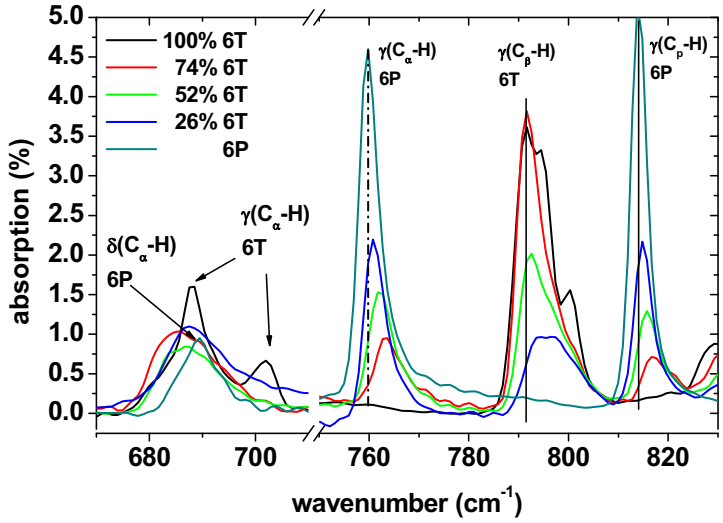

Fig. 4.8: IR absorption spectra of the γ(C-H) o.-o.-p. bending region of co-deposited 6T/6P films on SiO_2. The absorption is scaled to a film thickness of 40 nm.

The data suggest that the 6T / 6P co-deposited films exhibit co-existence of pure 6T and mixed 6T / 6P domains for a high 6T content of >60 % 6T (Fig. 4.9). Since the vdWL of 6P is slightly longer than the vdWL of 6T, intercalation of the smaller 6T molecules into the 6P structure becomes possible, leaving only small holes that do not hamper the growth of the next layer. In the reverse case, a 6P molecule intercalated into a 6T layer would stick out of the 6T surface, since the 6P molecules are forced to exhibit similar orientation to the surrounding 6T molecules, thus hampering the growth of the next 6T layer. This causes the phase separation into pure 6T and 6P rich mixed domains. Therefore, it is expected that 6P-rich films show no phase separation. To test this model, it is necessary to co-deposit molecules with different van der Waals lengths, which should result in either a phase separation, or in an amorphous growth.

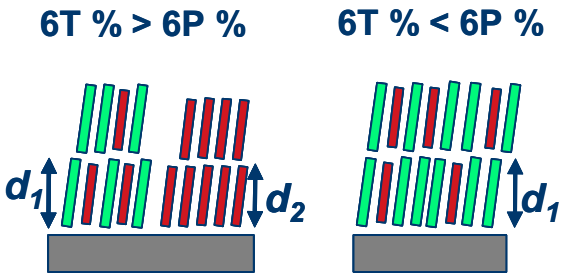

Fig. 4.9: Cartoon of the mutual molecular arrangement. For 6T rich films phase separation into a pure 6T phase (d_2) and 6P rich intercalated 6T/6P phase (d_1) was found. The 6P rich film did not exhibit phase separation.

4.1.2 Similarly sized conjugated cores + alkyl-end-chain

So far only well ordered mixed films of molecule pairs of similar conjugated core sizes are observed. The next step is to modify one part of the pair slightly with an alkyl-chain-end-substitution to test if the steric hindrance causes phase separation.

4.1.2.1 6T / DH6T

First, I discuss the results for co-deposited thin films of 6T and DH6T, for which the conjugated molecular moiety is identical. Representative AFM images of pure 6T and DH6T, as well as of co-deposited 6T/DH6T films of 20 nm nominal thickness, are depicted in Fig. 4.10. For pure DH6T (0% 6T; Fig. 4.10 a), islands exhibiting three distinct height levels can be observed. Some islands were interconnected and exhibited a "liquid-like" appearance. A rather similar morphology was observed for 17 % 6T (Fig. 4.10b), however, with smaller and less interconnected islands. The 57 % 6T film (Fig. 4.10 c) exhibited a more granular appearance with less round island shapes compared to Fig. 4.10a. The morphology of the 78 % 6T film (Fig. 4.10 c) displays more pyramid-like islands, with more apparent height levels of individual terraces. Finally, pure 6T (Fig. 4.10 e) also showed the characteristic pyramid-like morphology with at least seven exposed molecular layers, however, with reduced island density and heavily fringed island edges. Films of 40 nm - 50 nm nominal thickness had very similar morphologies (not shown).

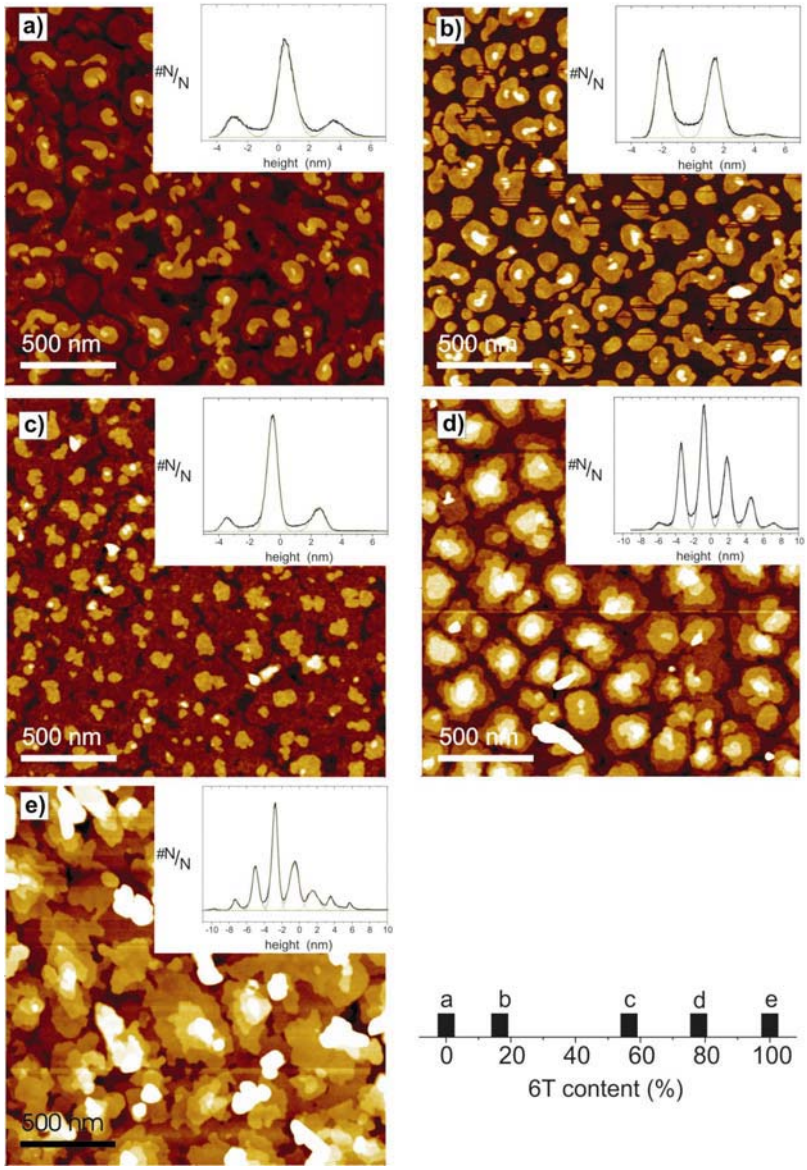

Fig. 4.10: Tapping mode AFM images of co-deposited films 6T/DH6T films on SiO_2 of 20 nm nominal thickness: a) 0 % 6T; b) 17 % 6T; c) 57 % 6T; d) 78 % 6T; e) 100 % 6T. The insets show the height distribution of the images ($\#N/N$ relative number of pixels per height interval; the first peak corresponds to the bottom-most visible layer). The height scale is adjusted for maximum contrast.

Apparently, the surface morphology changed gradually depending on the ratio between DH6T and 6T. In general, DH6T-rich films exhibited interconnected smooth-edged islands with only two to three layers forming terraces; 6T-rich films showed more pronounced fringed-island formation with more molecular layers forming the surface-exposed pyramid terraces. A detailed analysis of the AFM image height distributions allows one to asses the step height of terraces

with high precision. The height distributions for all samples (insets in Fig. 4.10) showed well-defined peaks, whose distance corresponds to the distinct step height of island terraces. (The background between peaks is attributed to the convolution of sample morphology with the AFM tip shape. The very bright spots seen in some images are attributed to surface contamination, which do not contribute to the step-height evaluation since they are higher than 10 nm.) The peaks could adequately be fitted with Gaussian distributions. To derive the average step height, the resulting peak maxima were plotted as a function of peak number, and a linear fit was applied. The results of this analysis routine are summarized in Fig. 4.12, together with data from additional samples not depicted in Fig. 4.10.

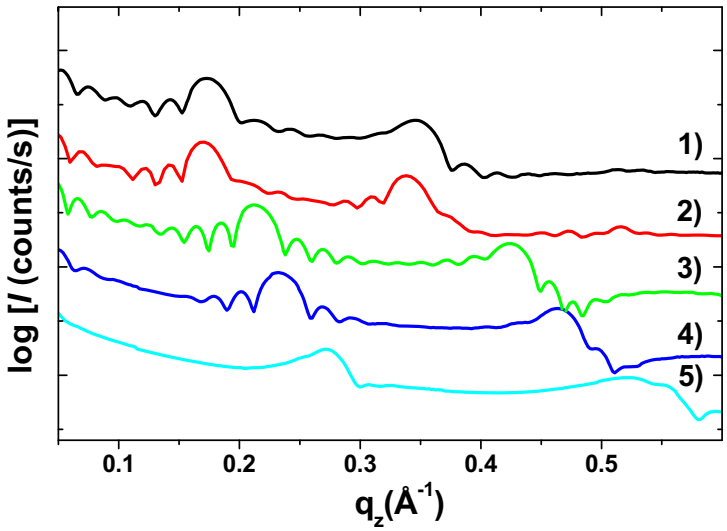

Fig. 4.11: Specular XRD scan of co-deposited 6T / DH6T layers on SiO2: 1) 0 % 6T; 2) 7 % 6T; 3) 60 % 6T; 4) 79 % 6T 5) 100 % 6T. The spectra are shifted vertically for clarity. q_z is the vertical momentum transfer vector and *log(I)* is logarithm of the count rate.

The plot of the specular XRD scan of the pure DH6T film on a native silicon oxide exhibited two peaks at $q_z = 0.173$ Å^{-1} and $q_z = 0.345$ Å^{-1} (see Fig. 4.11), which we assign to the (0 0 1) and (0 0 2) diffractions of a DH6T polymorph with a lattice spacing of $d = 3.64$ nm. This spacing is similar to the $d = 3.6$ nm spacing observed for small DH6T crystallites by Lovinger et al. [96] and to other reported *d*-values of DH6T on SiO_2 (3.55 nm [38], 3.54 nm [39], and 3.6 nm [96]). A film with 7 % 6T exhibited two peaks at 0.170 and 0.339 Å^{-1}, which are assigned to (0 0 1) and (0 0 2) diffractions of a single material phase (which will

be supported below by infrared spectroscopy results) with a lattice constant of $d = 3.71$ nm. A sample with 60 % 6T exhibited peaks at 0.212 and 0.414 Å^{-1}, corresponding to $d = 2.96$ nm. The typical appearance of (0 0 1) and (0 0 2) diffractions is continued for a film with 79 % 6T, resulting in $d = 2.7$ nm. However, pure 6T films exhibited polymorphism, as recognized by a broad (0 0 1) peak centered at 0.26 Å^{-1} and a (0 0 2) peak at 0.52 Å^{-1}, corresponding to $d = 2.42$ nm (representing the known β-phase of 6T [91] with $d = 2.44$ nm). Sharper (0 0 1) and (0 0 2) peak components at 0.279 and 0.558 Å^{-1} (yielding $d = 2.25$ nm) agree with the 6T γ-phase ($d = 2.24$ nm)[91].

All interlayer spacing values for the pair 6T/DH6T are summarized in Fig. 4.12, including values obtained independently from AFM measurements. We note that d values derived from AFM data at 6T proportions smaller than 50 % have a larger error due to the comparably small number of visible island steps. (C.f. Fig. 4.10) The dependence of d on the 6T content directly suggests a substrate-independent linear relation throughout the entire range investigated (except for pure DH6T, due to a different intralayer structure). These data alone provide already strong indications for a mixing of 6T and DH6T.

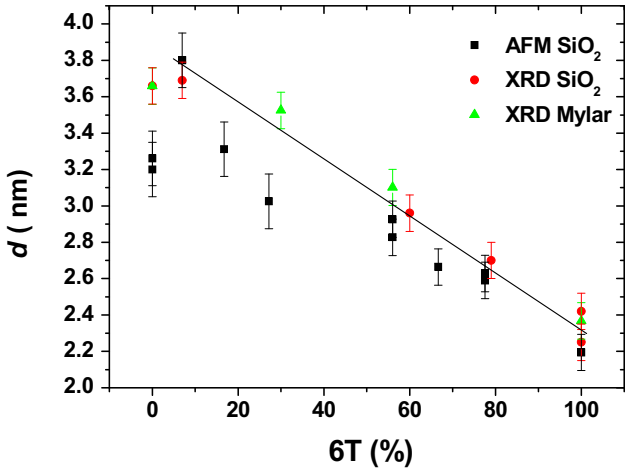

Fig. 4.12: Interlayer distance d of 6T/DH6T co-deposited films on SiO_2 and Mylar measured by AFM and XRD as a function of 6T content. The line is a guide for the eye of the linear dependence. The films deposited on Mylar are discussed at p. 98.

More direct evidence for this intercalation was obtained from IR measurements (Fig. 4.13). For pure 6T, the γ(C_α-H) out of plane bending mode of the 6T terminal rings is located in the spectral region of 660-720 cm^{-1}, which exhibited Davy-

dov splitting into two peaks at 688 and 702 cm^{-1}. [85] On the other hand, 6T samples co-deposited with DH6T exhibited no clear-cut splitting and only one red-shifted asymmetric peak at 682 cm^{-1} was observed. DH6T showed no such peak since hexyl chains are attached to the α-position of the terminal rings. This means that DH6T intercalation of 21 % was sufficient to change the unit cell of 6T molecules, thus subduing the Davydov splitting of pristine 6T. Furthermore, these spectra directly rule out the coexistence of DH6T and 6T crystallites (or layers) in mixed films. Changes of the in-plane structure (unit cell) of mixed 6T/DH6T samples compared to pure 6T samples were confirmed by preliminary grazing incidence X-ray diffraction experiments, which will be reported in detail elsewhere.

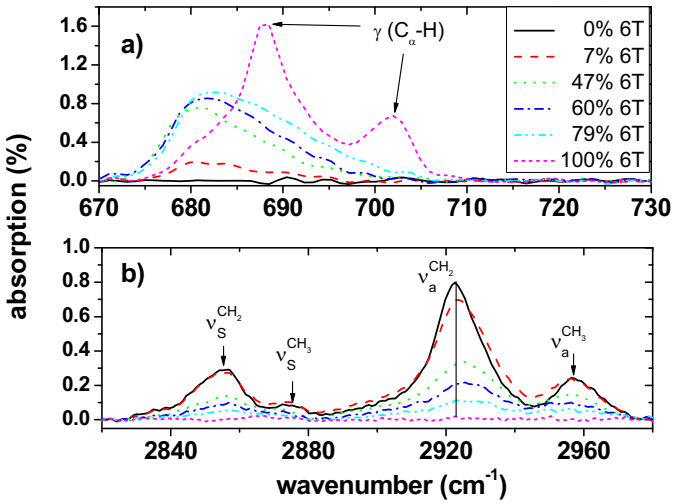

Fig. 4.13: IR absorption spectra of co-deposited thin films on SiO_2: a) γ($C_α$-H) deformation region; b) alkyl C-H stretching region of 6T/DH6T.

For DH6T, Garnier, et al. [38], proposed that strong π-π interactions between the rigid conjugated sexithiophene cores and van der Waals interactions between the flexible alkyl chains leads to a separation of these subunits into alkyl and sexithiophene domains within one molecular layer. [96] The observed linear dependence of the interlayer spacing on the 6T content (Fig. 4.12) can be related to this motif of intralayer phase separation. The observed changes in *d* could then be explained by two mechanisms: (i) The angle between hexyl chains and substrate, as well as the angle between sexithiophene-moieties and substrate, may depend on the intercalation level. (ii) The conformation of hexyl chains in co-deposited films changes, as free volume in the hexyl domain is created by replac-

ing a DH6T molecule by 6T within one layer. As a consequence, hexyl domains should be less ordered in mixed films, e.g., by alterations of the tilt angle between conjugated core and hexyl chains or by some C-C bonds of the hexyls being in cis conformation (in densely packed pristine DH6T, hexyl chains are supposedly in the all-trans conformation [38]). While mechanism (i) is most likely the reason for the abrupt increase of *d* when going from pure DH6T to mixed films, the gradual decrease of *d* for increasing 6T content can be related to mechanism (ii).

Support for this explanation is provided by IR data in the region of 2820 cm^{-1} - 2980 cm^{-1} (Fig. 4.13 b), where C-H stretching vibrations of the hexyl groups of DH6T are located. First, the pure DH6T (0 % 6T) spectrum is discussed. The strongest peaks at 2855 and 2923 cm^{-1} can be assigned to the symmetric and anti-symmetric C-H stretching bands of CH_2.[97] The small peaks at 2874 and 2958 cm^{-1} are due to the symmetric and anti-symmetric C-H_3 stretching band of the terminal methyl group of the DH6T hexyl chain. [97] The asymmetric CH_2 stretching peak exhibited a gradual blue-shift of up to 3 cm^{-1} (for the 79 % 6T co-deposited sample) for increasing 6T content in DH6T (Fig. 4.13 b). No energy shift was observed for the other alkyl stretching bands. Park et al. [97] reported that decreasing order and packing density of self-assembled monolayers of alkanethiols on Au led to a blue shift of the methyl C-H_3 stretching band. Therefore, it can be concluded that in the co-deposited 6T/DH6T layers the order and packing density of the DH6T hexyl chains is lower compared to the pure DH6T films.

4.1.2.2 6P / DH6T

I now turn towards the material pair 6P/DH6T, whose CC length of 6T [87] (2.61 nm) and 6P [88] (2.87 nm) differ by 0.26 nm (9 %). I will show that such co-deposited films exhibit the same behavior as 6T/DH6T films. Representative AFM images of co-deposited 6P/DH6T films of 20 nm nominal thickness are depicted in Fig. 4.14. The AFM height image of pure DH6T was depicted in Fig. 4.10. The morphology evolution for films with different molar ratios is similar for 6P/DH6T as for 6T/DH6T. For 18 % 6P (Fig. 4.14 a) smaller islands were observed compared to pure DH6T. The 44 % 6P film (Fig. 4.14 b) exhibited a more granular appearance with still rather round island shapes. The morphology of the 73 % 6T film (Fig. 4.14 c) displays more pyramid-like islands and with more apparent height levels of individual terraces. Pure 6P (Fig. 4.14 d) showed the characteristic pyramid-like morphology with seven exposed molecular layers, however, with increased island density and rather smooth island edges compared

to pure 6T. Thus, the surface morphology of mixed 6P/DH6T films also changed gradually depending on the ratio between DH6T and 6P.

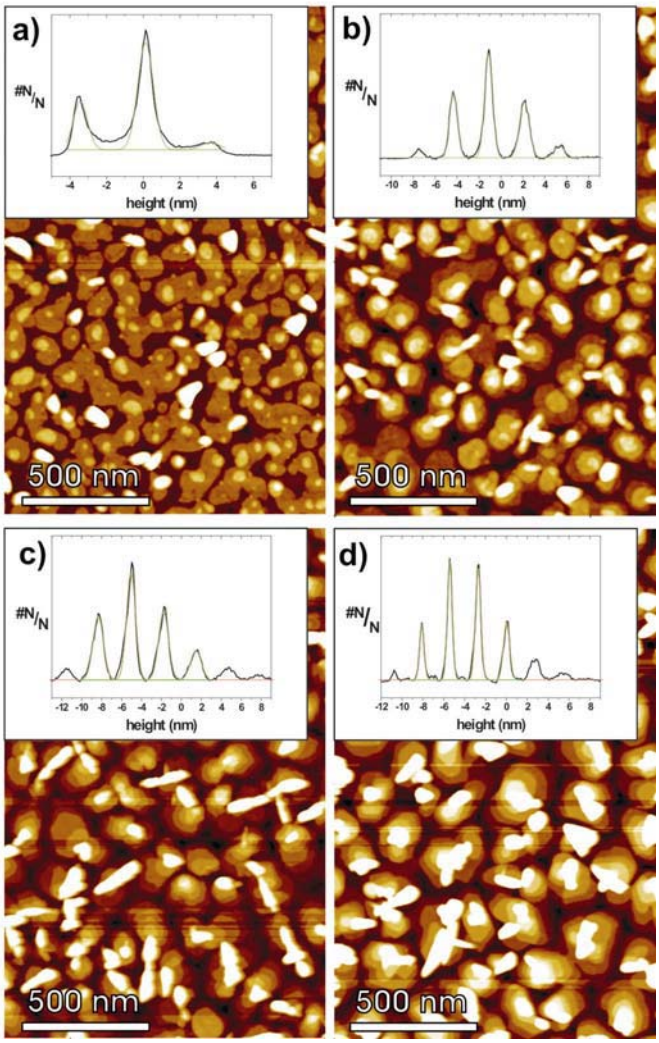

Fig. 4.14: AFM height images of 20 nm thick co-deposited films of 6P and DH6T on SiO_2: a) 18 % 6P; b) 44 % 6P; c) 73 % 6P; d) 100 % 6P. The insets show the height distribution of the images after background subtraction. The height scale is adjusted for maximum contrast.

The interlayer distance *d* between molecular layer parallel to the substrate surface are probed by specular XRD (Fig. 4.15). The 16 % 6P sample showed (0 0 1) and (0 0 2) reflections (q_z = 0.169 and 0.338 Å^{-1}, respectively; corresponding to *d* = 3.72 nm. Similar assignments yielded *d* = 3.44 nm for 33 % 6P and *d* = 3.06 nm for 73 % 6P. The pure 6P film showed two slightly asymmetric (001) and (002) peak series, corresponding to the coexistence of the γ-phase [92] (*d* = 2.72 nm) and a small fraction of the β-phase [92] (*d* = 2.60 nm).

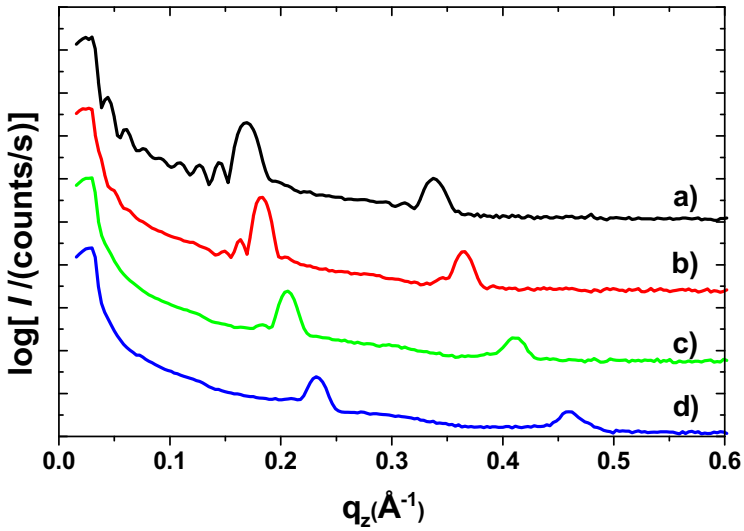

Fig. 4.15: Specular X-ray diffraction of co-deposited 6P/DH6T layers on SiO_2: a) 16 % 6P, b) 33 % 6P, c) 73 % 6P, d) 100 % 6P. The spectra are shifted vertically for clarity. q_z is the vertical momentum transfer vector, and log I is the logarithm of the count rate.

The interlayer spacings measured by AFM are included in the compilation of the X-ray data as function of 6P content in Fig. 4.16. The intralayer spacing d for 6P/DH6T films thus shows the same linear dependence on 6P content as the 6T/DH6T films (with the dependence on 6T content).

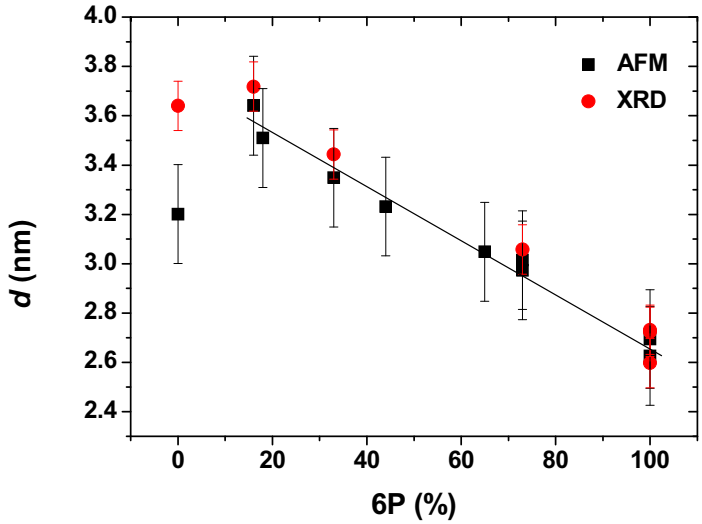

Fig. 4.16: Interlayer distance *d* of 6P/DH6T co-deposited films on SiO_2 measured by AFM and XRD as a function of 6P content. The line is a guide for the eye of a linear dependence.

The IR data in the region of 2820 cm^{-1} - 2980 cm^{-1} (Fig. 4.17 a), where C-H stretching vibrations of the hexyl group of DH6T are located, show exactly the same trend as those for 6T/DH6T samples. The asymmetric CH_2 stretching peak gradually blue shifts by up to 3 cm^{-1} (for 72 % 6P) for increasing 6P content in DH6T. Consequently, I conclude an intercalation of 6P and DH6T, facilitated by the flexibility of DH6T hexyl chains, in full analogy to the above discussion of 6T/DH6T samples (c.f. schematic of both structures shown in Fig. 4.18). The γ(C-H) o.-o.-p. vibrations [93] of 6P (Fig. 4.17 b) at 759.8 cm^{-1} and 814.3 cm^{-1} show a blue shift of 2.2 cm^{-1} and 1.2 cm^{-1} indicating the local environment of the 6P molecules changes with the co-deposition of DH6T. In general, it thus appears that the strong π-π-interactions between even dissimilar conjugated cores are responsible for the observed intercalation behavior. Phase separation, instead, would result in the mixture of inhomogeneous layer thickness (i.e., alkylated versus non-alkylated domains) within one nominal layer, which seems energetically unfavorable, in particular in three-dimensional growth. A systematic change in the tilt angle of the molecules for different film compositions as reason for the observed *d* variation can be ruled out as this would require two different tilt angles for DH6T and 6T within a sample, which would lead to phase separation. The opposite was observed.

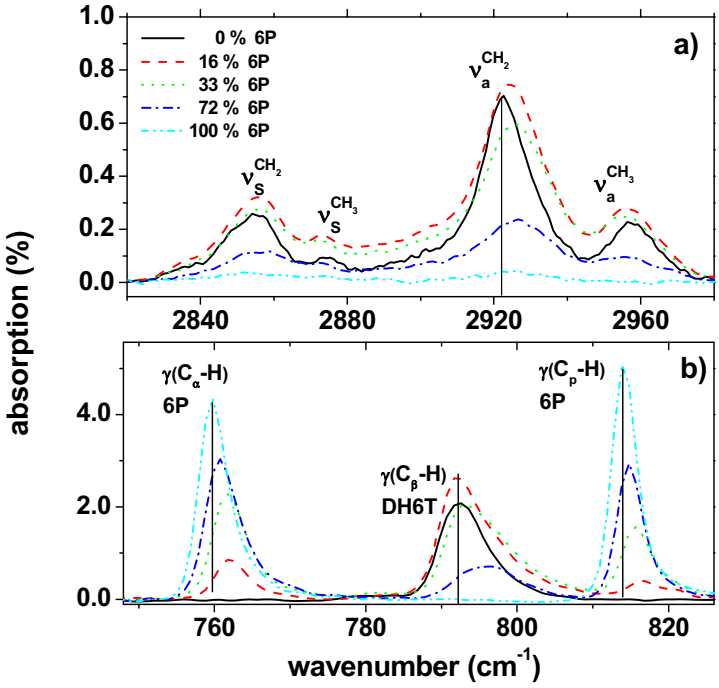

Fig. 4.17: IR absorption spectra of co-deposited 6P/DH6T thin films on SiO_2: a) alkyl C-H stretching region of DH6T b) γ(C-H) deformation region.

Conclusion

I prepared co-deposited thin films of the material pairs 6T/DH6T and 6P/DH6T with varying molecular ratios (19 % to 80 %). In contrast to my first assumption, the alteration of the total van der Waals length of 6T molecule by attachment of an alkyl-end-chain lead not to phase separation due to steric hindrance.

Instead, AFM and X-ray measurements show that the films grow in well ordered, mixed, and layered structures. It is possible to control the interlayer distance *d* by the DH6T content of the film. I will show that this behavior is not only observable on inert substrate with very low surface roughness but even on a rough polymer films like Mylar c.f. section 4.2. This indicates that this growth mode seems not to depend on a specific substrate. The *d* dependence is attributed to the mutual mixing of 6T and DH6T or 6P and DH6T within layers, due to the strong π-π interaction of the conjugated molecular cores and the flexibility of DH6T hexyl chains, as evidenced by IR investigations. Thus, vacuum co-

deposition of a rigid conjugated molecule with an alkylated rod-like molecule can be a practical method to fabricate mixed layers containing two conjugated moieties with vastly different electronic properties with the additional possibility to tune interlayer distances with sub nanometer precision. This type of self-assembly of organic molecules on a substrate from the vapor phase will enable detailed investigations of intermolecular coupling between conjugated layer stacks, separated by controlled insulating layers. Normally mixed crystals between molecules consisting out two different isotopes e.g. C_{12} und C_{13} were used for such studies. The two isotopic molecules form mixed crystals at all ratios, but have slightly different optical properties [69].

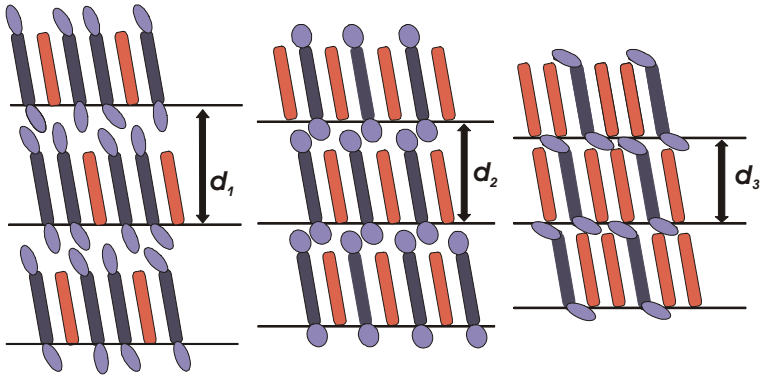

Fig. 4.18: Schematic molecular arrangements for mixed films, indicating different interlayer spacings $d_1 > d_2 > d_3$.

4.1.3 Differently sized conjugated cores

The four material pairs described so far in this work have the ability to form well ordered layered mixed structures. All pairs have in common that the conjugated cores of the pairs were similarly sized. To determine if a matching length of the CC is a necessary prerequisite for the mixing, I co-deposited materials with different CC length.

4.1.3.1 4T / 6T

I started with two materials with the same *type* of CC but different vdWL. The vdWL of 4T (1.82 nm) [29] and 6T (2.61 nm) [87] differ by 0.79 nm (30 %). The surface of the 20 nm thick 62 % 4T film (Fig. 4.19) exhibits three different kinds of features: layered structures of 2.3 nm step height (Fig. 4.19 a) covering a small amount of the surface, 1000 nm × 250 nm (typical values) footprint-area islands of 150 nm – 200 nm height, and 50 nm high frayed islands (Fig. 4.19 b) plus some small needle-like islands of 40 nm - 50 nm height. This complex surface morphology gives the first information that the 4T/6T sample does not consist of one homogeneous mixed film.

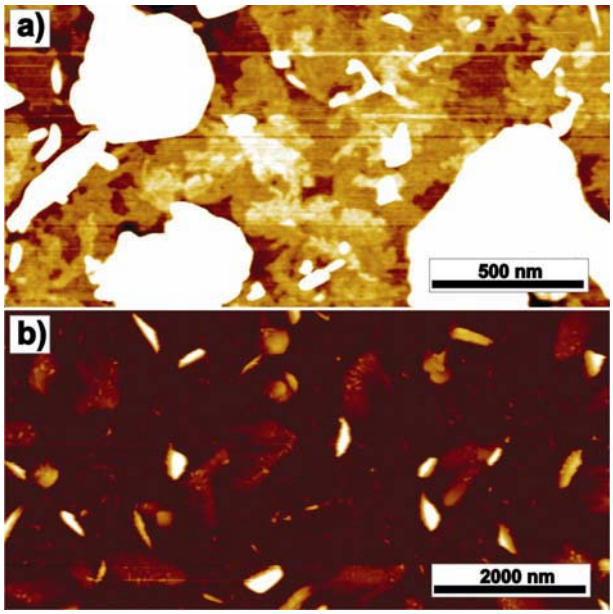

Fig. 4.19: AFM height images of 62 % 4T/6T film of 20 nm thickness on SiO_2. a) Height scaled to show layered structure with 2.3 nm step height b) Height scaled to the show island morphology: high needle-like islands (150 nm - 200 nm height), frayed islands (50 nm), and small needle-like island (40 nm – 50 nm).

The specular XRD scans, measured with Cu K_α radiation, are shown in Fig. 4.20. The scan of the pure material films are shown in Fig. 4.2 and Fig. 4.6. The 22 % 4T film shows unshifted peaks of the (0 0 2n) series of the LT-6T [90] or γ-6T [91] polymorph, indicating standing molecules. The peak at $q_z = 1.42$ Å^{-1} can be identified as a superposition of the (0 0 10) and (4 1-1) peak of the LT-6T phase, indicating a molecular orientation almost perpendicular and almost parallel to the substrate surface. The small sharp peak at $q_z = 1.599$ Å^{-1} is the (0 2 0) reflex of LT-6T representing lying molecules. The broad peak at $q_z = 1.67$ Å^{-1} is a superposition of the (0 0 12) LT-6T peak at $q_z = 1.6868$ Å^{-1} and the 4T-LT [84] (0 0 8) at $q_z = 1.65$ Å^{-1}.

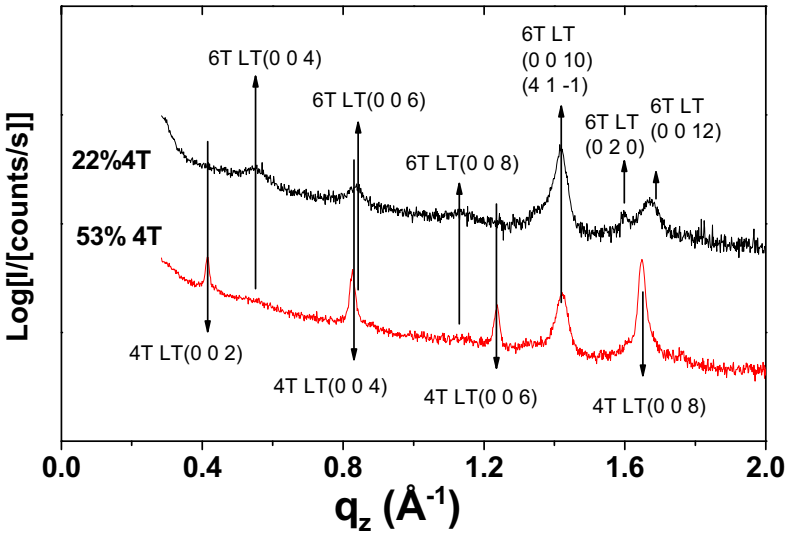

Fig. 4.20: Specular XRD scans of co-deposited 40 nm thick films of 4T/6T on SiO_2.

The 53 % 4T film exhibits an unshifted (0 0 2n) series of the LT-4T polymorph indicating that the 4T molecules are oriented perpendicular to the substrate surface. The peak at $q_z = 1.4231$ Å^{-1} can be identified as (4 1-1) of the LT-6T phase. The XRD data shows no sign of a mixed phase of 4T and 6T. The low intensity of the peaks leads to the following possible interpretations. (i) A large amount of 4T and 6T is not ordered and, as a result, causes no diffraction peaks. (ii) The scattering planes are not oriented parallel to the substrate surface and, therefore, cannot be detected in the θ-2θ specular scan.

The amorphous growth assumed in (i) would lead to strong changes in the IR spectra, since the local molecular environment is different for every single molecule similar to the situation in solution. Fig. 4.21 shows that the IR spectra of co-deposited films are just superpositions of the pure material film spectra. Of special interest is the fact that the Davidov [85] splitting of the γ(C_α-H) vibration peak of 4T and 6T does not vanish in the co-deposited film. This indicates that the local crystal structure of the 4T and 6T molecule is unchanged in the co-deposited film in contradiction to (i). This supports (ii) which indicate that a larger part of the co-deposited film consists of ordered phase separated domains of 4T and 6T which have no preferential orientation to the substrate surface causing the low scattering intensities (XRD) and "tilted" islands (AFM).

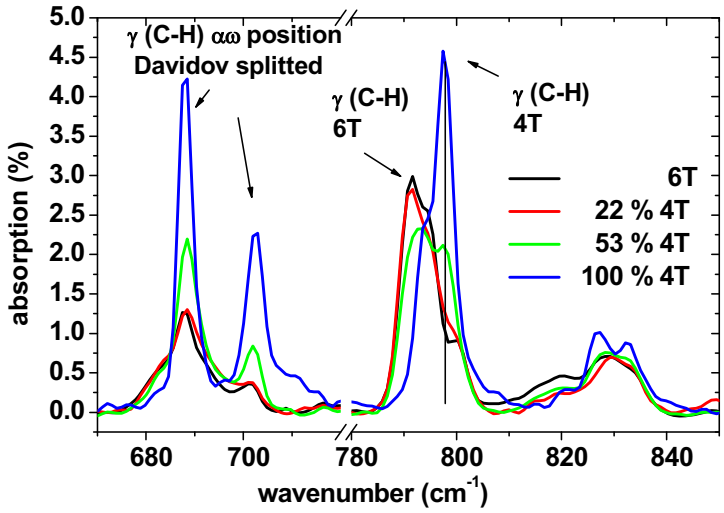

Fig. 4.21: IR absorption spectra of the γ(C-H) out-of-plane bending region of co-deposited films of 4T/6T on SiO_2. Please note that the mixed film spectra are superpositions of the pure film spectra.

The following material pair differs in it's CC length and additionally in the type of the conjugated core.

4.1.3.2 4T / 6P

Similarly to the preceding pair of 4T/6T, the vdWL of 4T [29] (1.82 nm) and 6P [88] (2.87 nm) differ by 1.05 nm (37 %). The specular XRD scan (Fig. 4.22) of the 28 % 4T co-deposited film shows only a weak peak at q_z = 0.7023 Å^{-1} that can be assigned to (0 0 2) of almost standing 6P molecules in the γ-phase[92]. The standing 4T molecules in the LT-4T phase[84] are represented by the (0 0 *l*) series with a pronounced (0 0 4) peak. There are two strong peaks at q_z = 1.376 Å^{-1} and q_z = 1.415 Å^{-1} that can be assigned to (-1 1 1) and (-1 1 2) reflections of the β-phase [88] or γ-phase [92] of 6P and the HT-phase [18] of 4T, because the foot print of the 4T and 6P unit cells are very similar. These peaks indicate that the cleavage planes of the crystallites that are oriented parallel to substrate.

The 55 % 4T film exhibits a more pronounced (0 0 *l*) series of LT-4T [84] and a consequently weaker (0 0 2) peak of the 6P γ-phase. The peaks at q_z = 1.376 Å^{-1} and 1.415 Å^{-1} show similar strength for both mixing ratios, indicating that both 4T and 6P contribute to these peaks.

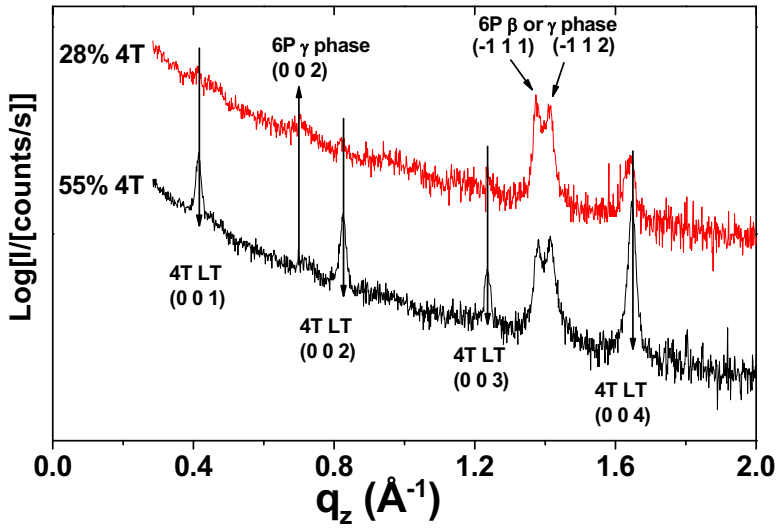

Fig. 4.22: Specular XRD scan of 40 nm thick 4T/6P films on SiO_2

The AFM height image of a 4.6 nm 56 % 4T film (Fig. 4.23 a) exhibits layered structures with 2.86 nm step height (similar to vdWL of 6P) and a "round" shape similar to DH6T thin films (Fig. 4.10 a). Note the numerous holes in the islands, which could be 4T inclusion in 6P islands and could explain the low XRD signal of standing 6P. The white spot is a 25 nm high island with no depletion zone around it, indicating that the layered structures and the high islands grow independently. This suggests that the 4T separates into the high islands from the first layer on. The surface of a 20 nm thick film (Fig. 4.23 b) exhibits three different features: layered structures covering the substrate that can be related to the domains of standing 6P, 40 nm high needle-like islands and islands of 60 nm - 90 nm height and 500 nm footprint with ether flat (standing molecules) or tilted surfaces (lying molecules). It is possible to relate the latter island type to 4T since their number increases with increasing 4T content of the film.

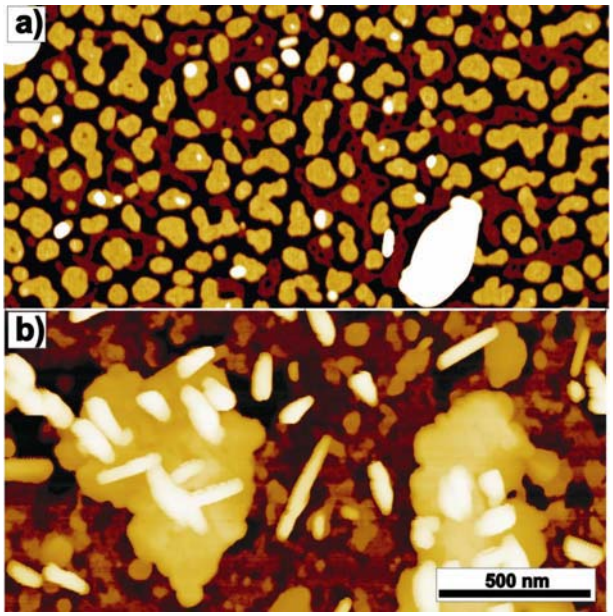

Fig. 4.23: AFM height images of co-deposited films of 4T and 6P grown on SiO_2. a) 56 % 4T film of 4.6 nm thickness. Please note the small holes in the layered structures and the 30 nm high island. b) 60 % 4T film of 20 nm thickness shown in a non linear height scale. Note the three different morphologies: Layered structures covering the ground, 40 nm – 60 nm high 4T-like islands, and 40 nm - 50 nm high needles.

The IR spectrum (Fig. 4.24) shows only weak peak shifts of about 0.5 cm^{-1}. As discussed before, the persistence of the Davidov splitting of the 4T $\gamma(C_\alpha\text{-H})$ [85] vibration around 655 cm^{-1} in the co-deposited film spectra, indicates that most of the material is in the pure material state and indicates a good phase separation into ordered domains of 4T and 6T. The 6P peaks [93] show only weak blue shifts (~0.5 cm^{-1}) and no line broadening indicating that the local environment of the 6P molecules is similar in the 6P and mixed films. This indicates a pronounced phase separation into ordered domains of 4T and 6P. The AFM and XRD data indicate that a large part of the 4T grows in ordered domains of standing molecules, where as the 6P grows in ordered domains with molecular orientation nearly parallel and perpendicular to substrate surface.

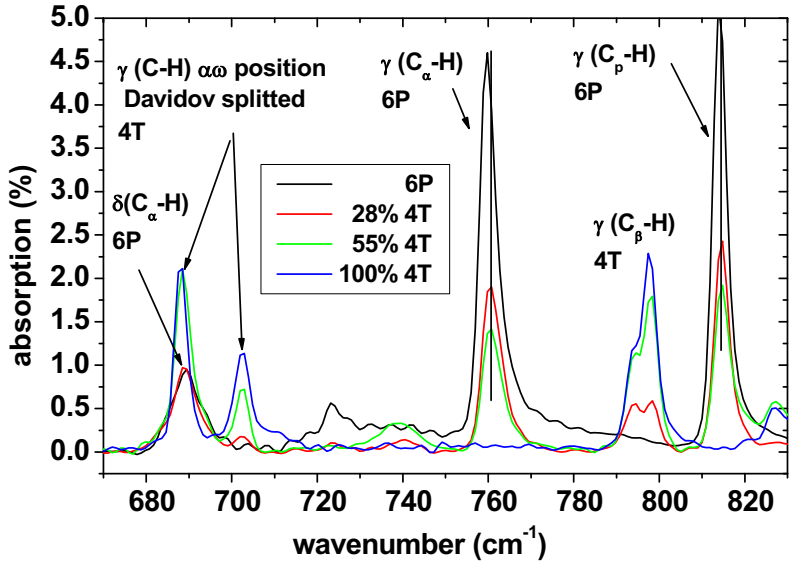

Fig. 4.24: IR spectrum of co-deposited thin films of 4T/6P on SiO_2 of 40 nm thickness. Note that the 4T $\gamma(C_\alpha\text{-H})$ vibration is Davidov split for all 4T contents. All other peaks show only weak blue shifts (~ 0.5 cm^{-1}).

4.1.3.3 PEN / 6T

The material pair PEN/6T has with vdWLs of 1.64 nm (PEN [22]) and 2.61 nm (6T [87]) exhibits an identical van der Waals length difference of 37 % (0.97 nm) to the preceding material pair. However, it exhibits a very different growth behavior. The AFM image of a 55 % PEN film of 4.7 nm thickness (~ 2 mono layer) is shown in Fig. 4.25a. The film consists of an almost closed first layer with a smooth surface. A second layer, consisting out of loosely packed islands with a height of 1.6 nm to 2 nm, is located on top. This height variation already indicates mixing and/or phase separation on the nm scale, at least in the second layer. The third distinct height level comprises small islands of a typical height of 10 nm. It should be mentioned that the loosely packed second layer poses a rough surface for the following molecules. That is different to the phase separating material pairs discussed before, which showed pronounced phase separation already in the 1 to 2 monolayer range. The 20 nm thick 46 % PEN film (Fig. 4.25 b) exhibits a very high surface corrugation. It consists of small 30 nm - 80 nm high islands with a high islands density.

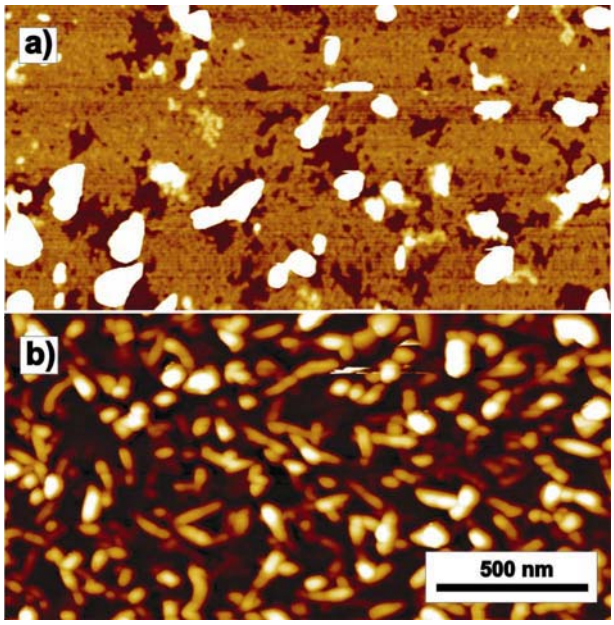

Fig. 4.25: AFM images of co-deposited PEN/6T films with a) 55 % PEN and 4.7 nm thickness, b) 46% PEN and 20 nm thickness on SiO_2.

I now turn to the specular XRD scan (Fig. 4.26) of a 40 nm 45 % PEN film. It shows rather broad features. The one at q_z = 0.3037 Å^{-1} (corresponding to d = 2.07 nm) could either be assigned to the (0 0 1) peak of HT-6T phase [87] (with d = 2.048 nm) or to the presence of a mixed phase. The peak at q_z = 0.7968 Å^{-1} (d = 0.79 nm) might be associated with the (0 0 3) peak of the β-6T [91] phase and (0 0 2) of the TF-PEN [20] (thin film) phase.

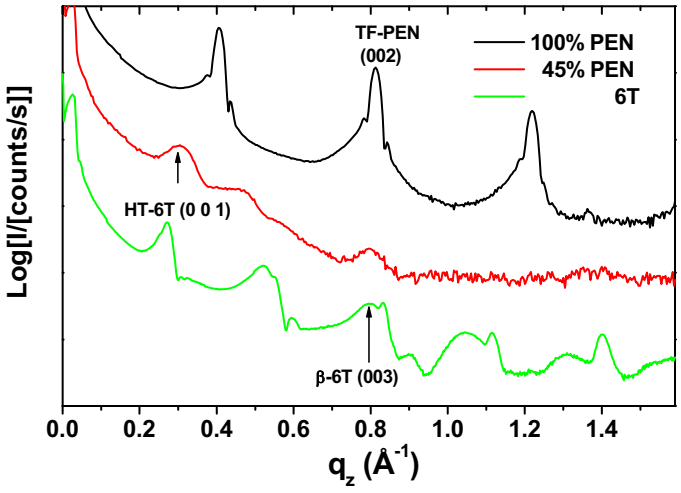

Fig. 4.26: Specular XRD scans of 40 nm thick PEN/6T film on SiO_2

The in-plane XRD scan (Fig. 4.27) clarifies the situation. No peaks related to PEN are observable in the spectra of the co-deposited film. The weak peaks at q_{xy} = 1.6167 Å^{-1} and q_{xy} = 1.9627 Å^{-1}of the co-deposited film can also be found in the 6T in-plane scan. A peak at q_{xy} = 1.3669 Å^{-1} is located between the peaks at 1.315 Å^{-1} and 1.383 Å^{-1} of the pure 6T film. From the XRD measurement, it can be deduced, that a small part of the film has a periodicity similar to the 6T film. In contrast, no indication for ordered PEN can be found.

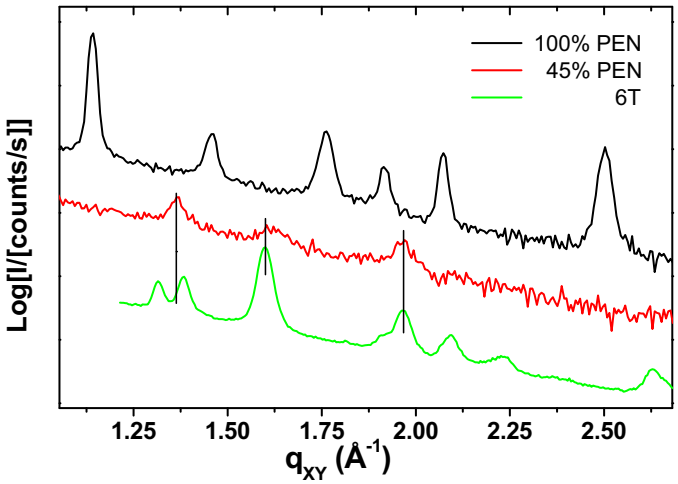

Fig. 4.27: In-plane XRD scans of 40 nm thick PEN/6T film on SiO_2.

Since XRD only probes ordered sample portions with lattice planes oriented perpendicular and parallel to the substrate surface, I analyze the IR spectra of the

γ(C-H) o.-o.-p. bending region of 6T and PEN (Fig. 4.28) to test for the presence of eventually unordered phases. The films with low PEN content (30 % and 45 % PEN) (Fig. 4.28 a) show a pronounced broadening of the peak at 729 cm^{-1}, which has a similar line shape as in fully mixed PEN/4T film (Fig. 4.3) discussed earlier in this thesis. This indicates that the local environment of the PEN molecules is amorphous. The 75 % PEN film shows a superposition of the split-peak found in the pure PEN spectra and the broad peak indicating a co-existence of ordered and amorphous phase. The PEN peak at 903.5 cm^{-1} doubles its line width and shows a blue shift of 1.8 cm^{-1}, which can be partly attributed to the Christiansen effect [71, 98].

In contrast, the 6T γ(C-H) o.-o.-p. bending peaks (Fig. 4.28 b) do not exhibit strong broadening. The Davidov splitting [85] of the γ(C_α-H) vibration around 688.7 cm^{-1} still exists in all of the co-deposited films. The peak at 791.8 cm^{-1} shows almost no shift and no change of the line shape as it was observed for mixing material pairs like 6T/DH6T [95] and 6T/6P (Fig. 4.8). Both observations strongly indicate that most of the 6T molecules grow in a phase very similar to that of the pure material film.

The IR data suggest that the film phase separates into domains of amorphous PEN and ordered 6T. The low intensities found in the XRD data of the mixed film may point to low texture of the 6T domains. A possible reason for the low order of the co-deposited film can be the rough substrate formed by the first two monolayers for subsequent film growth. This may prevent the following material from forming ordered layered structures.

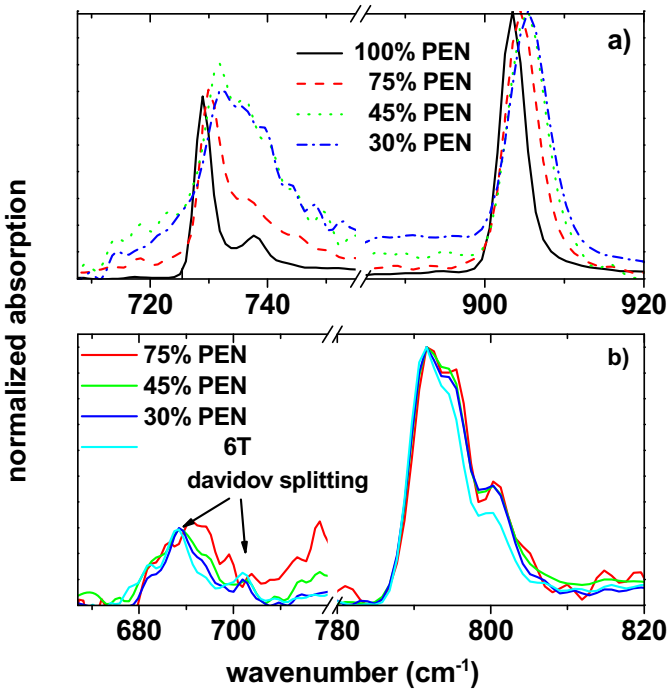

Fig. 4.28: IR spectra of 40 nm thick films grown SiO_2. γ(C-H) o.-o.-p. bending vibration peaks of PEN a) and 6T b) normalized to the peak maximum.

4.1.3.4 PEN / 6P

The vdWL of PEN [22] (1.64 nm) and 6P [88] (2.87 nm) differ by 1.2 nm (42 %) and a similar morphology as observed for PEN/6T films could therefore be expected and is actually observed. The AFM height image of a 1.2 nm thick (sub monolayer) 49 % PEN film is shown in Fig. 4.29 a). It exhibits loosely packed islands of about 3 nm height, which may indicate a phase separation of standing PEN and 6P domains on the few 10 nm scale. (Cf. Fig. 4.25 PEN/6T). This layer (1.5 nm RMS roughness) forms a rough substrate for subsequent molecular layers. The 20 nm thick 46 % PEN film (Fig. 4.29 b) exhibits close-packed, needle-like, and about 70 nm high islands. This surface morphology with a RMS roughness of 16 nm to 20 nm does not significantly change its islands height, size, and shape in the range of 70 % to 27 % PEN content. It has been reported that PEN and 6P grow in needle-like structures when deposited on rough substrates like indium tin oxide (ITO) [99] or polycrystalline gold [100].

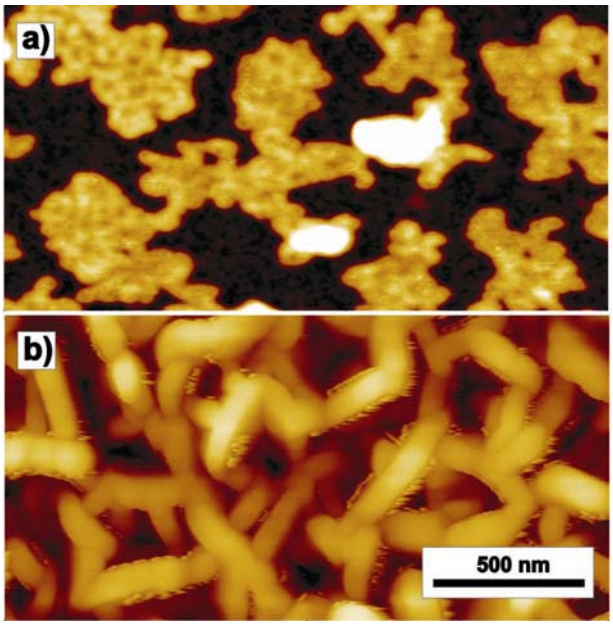

Fig. 4.29: AFM height images of co-deposited PEN/6P films on SiO_2. a) 49 % PEN film of 1.2 nm thickness. b) 20 nm thick 46 % PEN film. The height of the needle-like structures rages from 50 nm to 90 nm.

The IR spectra of the PEN γ(C-H) o.-o.-p. bending vibration region (Fig. 4.30 a) provide information on the bulk properties of the film. The peaks at 729.1 cm^{-1} and 737.7 cm^{-1} are significantly broadened upon co-deposition with 6P. The main peak (729.1 cm^{-1}) shows a pronounced blue-shift of 1.7 cm^{-1} (58 % PEN) and 2.4 cm^{-1} (27 % PEN). (Note: The background intensity oscillation in the (27 % PEN) spectrum is due to internal reflections in the sample and was amplified by the normalization procedure.) The peak at 903.4 cm^{-1} is blue-shifted by 2.1 cm^{-1} and its line width is almost doubled. This shifts can be partly attributed to the Christiansen [71, 98] effect, since the surface corrugation of the co-deposited films (Fig. 4.29 b) is significantly larger compared to the films of pure materials. (cf. Fig. 4.1 c, Fig. 4.5 c) However both, the broadening and the loss of the line splitting clearly point towards an amorphous local environment of the PEN molecules.

On the other hand, the 6P γ(C-H) o.-o.-p. bending peaks (Fig. 4.31 b) at 759.9 cm^{-1} and 814.2 cm^{-1} only show blue-shifts of 1.5 cm^{-1} and 0.7 cm^{-1} upon co-deposition with PEN. This shifts are small compared with the 3 cm^{-1} blue shifts observed for the (mixing) material pair 6P/6T (Cf. Fig. 4.8). This shift can be clearly attributed to the Christiansen effect [71, 98] caused by the high surface corrugation of the PEN/6P films indicating phase separation into ordered 6P domains and partly amorphous PEN domains.

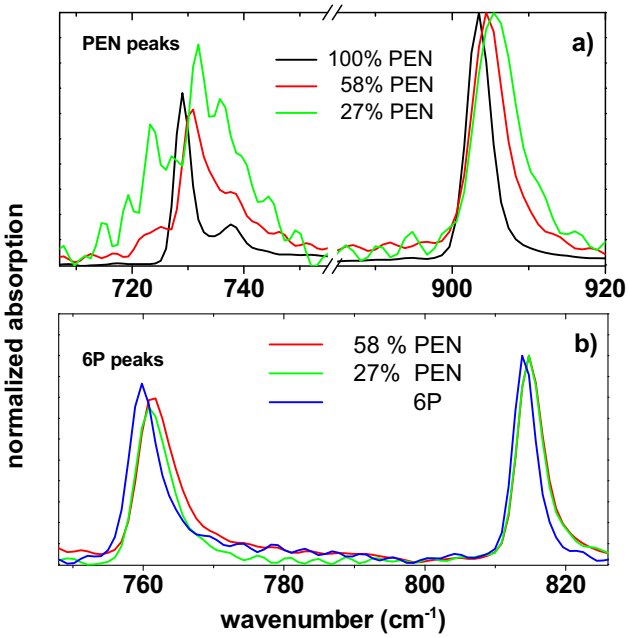

Fig. 4.30: IR spectra of PEN/6P films of 40nm thickness grown SiO_2. γ(C-H) o.-o.-p. bending vibration peaks of a) PEN and b) 6P are normalized to the peak maximum

The spatial order of the film was further investigated via specular XRD (Fig. 4.31). The intensity of the (001) and (002) peak of the TF-PEN [20] phase, measured at q_z = 0.4069 Å^{-1} and q_z = 0.8143 Å^{-1} for the pure PEN film, decreases to ~1 % of the original intensity for the 58 % PEN film. This indicates that maximal 1 % of the PEN portion in the co-deposited film has an orientation similar to the pure PEN. In the 27% PEN film the TF-PEN (001) and (002) peaks are even *not* observed.

In contrast, the intensity of the (1 0 0) peak of the γ-6P phase [92] decreases in the co-deposited film (27 % PEN / 73 % 6P film) to only 36 % of the pure 6P film value. That means that a large amount of the 6P molecules are in a similar orientation as in the pure 6P film. In the 58 % PEN the (1 0 0) γ-6P peak is very weak and broadened. The (3 0 0) peak of the γ-6P phase at q_z = 0.6836 Å^{-1} is shifted to q_z = 0.7035 Å^{-1} (27 % PEN). This shift can be explained by a superposition with the β-6P (3 0 0) peak [92] with d = 2.59 nm and a q_z = 0.7258 Å^{-1}. The broad peak at q_z = 0.8837 Å^{-1} can be associated with the (0 0 3) peak of PEN bulk phase [21] superimposed with the (4 0 0) γ-6P peak measured at 0.9164 Å^{-1}.

The intensity of the peaks around q_z = 1.394 Å^{-1}, which are associated with PEN and 6P molecules in an orientation almost parallel to substrate surface is slightly smaller than in the pure 6P film.

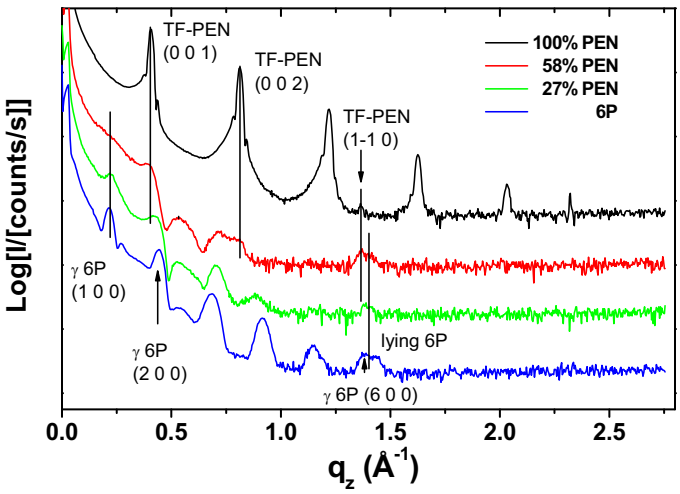

Fig. 4.31: Specular XRD scan of 40 nm thick PEN/6P films on SiO_2.

In contrast, the in-plane XRD scans show a much clearer picture (Fig. 4.32). The pure 6P film exhibits three major peaks at q_{xy} = 1.3847 Å^{-1}, at q_{xy} = 1.6231 Å^{-1}, and at q_{xy} = 1.9741 Å^{-1}. In the co-deposited film these peaks are only mildly broadened and exhibit shifts below 0.004 Å^{-1}. On the other hand, none of the PEN in-plane peaks could be observed in the spectra of the co-deposited films.

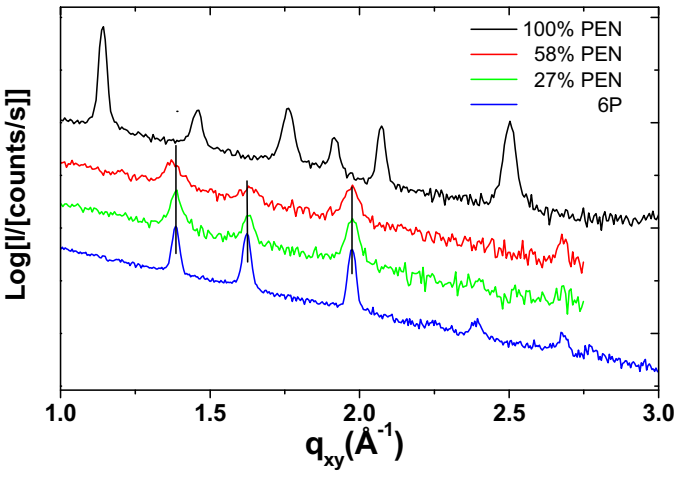

Fig. 4.32: In-plane XRD scans of 40 nm thick PEN/6P films on SiO_2.

The co-deposition of PEN and 6P leads to strongly corrugated films with a needle-like surface morphology and high corrugation (16 nm – 20 nm RMS roughness for 20 nm thick films). This growth mode is attributed to the roughness of the first molecular layer which hinders the subsequently deposited molecules to grow in textured and well phase separated structures. The difference in the initial two layers seems to be the reason, which distinguishes the growth of PEN/6T and PEN/6P from the phase separating material pairs 4T/6T and 4T/6P which grow in well ordered and phase separated films

Conclusion

In this section I presented the results on thin films of co-deposited pairs of rod-like conjugated molecules, which differ in about 30 % of their conjugated core length. In general, the films showed phase separation between the two components. In detail, two different growth behaviors were observed. First, films containing 4T (4T/6T and 4T/6P) showed pronounced phase separation into ordered domains of nearly standing or lying molecules starting from the first molecular layer on.

Second, the pairs containing PEN (PEN/6T) and (PEN/6P) showed a pronounced effect of substrate-molecule interactions on the growth of the first layers. This leads to mixing / micro-phase-separation on the nm-scale of the first layers forming a rough substrate for the subsequent molecular layers. This finally leads to films of needle-like texture and high surface corrugation. The XRD and

IR data indicate that in these films 6T and 6P are mostly ordered but untextured, whereas pentacene is mostly unordered.

4.1.4 Differently sized conjugated cores + alkyl end chain

Material pairs with differently sized CC, as discussed in the preceding section, exhibit phase separation. In contrast, molecular pairs with different total van der Waals lengths but similarly sized CC (6T/DH6T and 6P/DH6T [95]) preferential grow in well ordered mixed layered structures. One can therefore assume that the molecular alkyl-end-substitution promotes the growth of well-ordered mixed structures.

4.1.4.1 4T / DH6T

To test this assumption, 4T and DH6T were co-deposited, since they exhibit the same CC as the phase separating pair 4T/6T. The AFM height image of a 20 nm 53 % 4T co-deposited thin film (Fig. 4.33 b) is displayed in a nonlinear height scale to resolve the typical DH6T-like morphology (Fig. 4.33 c) covering the substrate. The DH6T-like film exhibits step heights of about 3 nm, similar to $d = (3.2 \pm 0.2)$ nm of the pure DH6T [95] film. The 15 nm – 150 nm high islands are of similar shape like the islands in the 4T films (Fig. 4.33 a). The steps on top of the high islands have a height of about 1.5 nm, similar to the $d = (1.50 \pm 0.06)$ nm measured for the pure 4T film. This seems to indicate phase separation into domains of standing 4T and DH6T molecules.

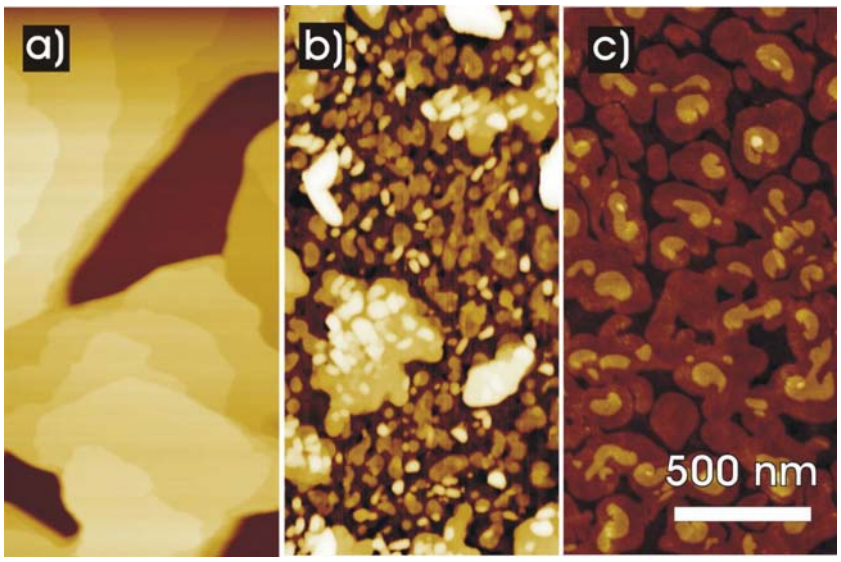

Fig. 4.33: AFM height images of 20 nm thick 4T/DH6T films on SiO_2: a) 4T, b) 53 % 4T, c) DH6T. The co-deposited film b) is shown with nonlinear height scale to show the DH6T-film-like morphology covering the substrate with ~3.05 nm steps and the 15 nm – 150 nm high 4T-like islands.

The specular XRD scan (Fig. 4.34) of the co-deposited films with 80 % 4T and 38 % 4T exhibits the (0 0 1) and (0 0 2) peak of the LT-4T phase [84] without shift. The weak (0 0 2) peak of the high temperature phase of 4T (HT-4T) [18] with d = 1.423 nm appears more pronounced in the spectra of the co-deposited film. The (0 0 1) and (0 0 2) peaks of the DH6T film belonging to d = 3.64 nm are present in the co-deposited film scan, though of weak intensity and significantly broadened. The XRD spectra show no peaks pointing to a lying molecular orientation.

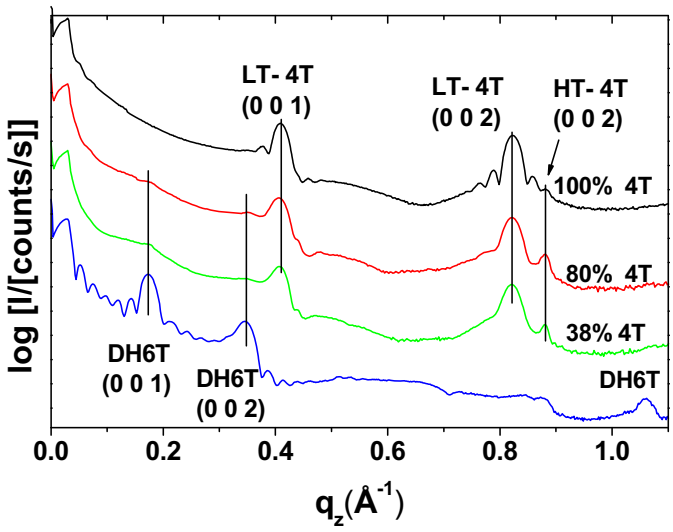

Fig. 4.34: Specular XRD scans of co-deposited 4T/DH6T films on SiO_2. The nominal thickness of the DH6T film is 40 nm; all other films are 20 nm thick.

The IR spectra of the γ(C-H) o.-o.-p. bending region [84, 85] (Fig. 4.35) show that the spectra of the co-deposited films are just superpositions of the pure material film spectra. This indicates that phase separation into domains of pure 4T and DH6T occurs. AFM and XRD data congruently show that most of the film layers are oriented parallel to the substrate. It can therefore be concluded that 4T/DH6T films grow in phase separated, ordered domains of standing molecules, very similar to the respective pure films.

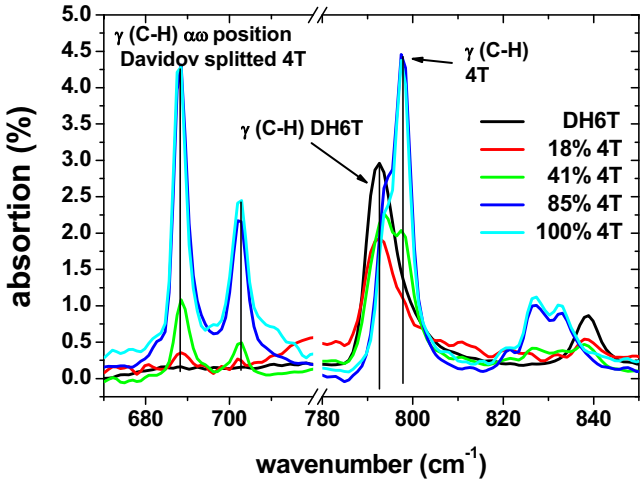

Fig. 4.35: IR absorption spectra of the γ (C-H) o.-o.-p. bending region of co-deposited films of 4T/DH6T of 20 nm thickness on SiO_2. Note that the mixed film spectra are superpositions of the pure material film spectra.

4.1.4.2 PEN / DH6T

PEN/DH6T is the most diverse material with respect to the vdWL of CC, the monomer type, and the alkyl-chain substitution. The vdWL of the CC differ by about 1 nm, with 1.64 nm for PEN [22] and 2.61 nm for DH6T, if the vdWL of the unsubstituted 6T molecule [87] is taken as reference. The AFM micrograph shown in Fig. 4.36 depicts three films with increasing PEN content. The substrate is covered in the 26 % PEN film (Fig. 4.36 a) with a two layer structure with ~ 3.1 nm step height, similar to the step height of $d = (3.2 \pm 0.2)$ nm measured with AFM for pure DH6T [95] films. Additionally, the film exhibits 10 nm - 20 nm high islands. The film with 62 % PEN (Fig. 4.36 b) shows 20 nm high islands of very diverse shape and 30 nm high elongated islands. The diverse shape of the islands indicates that they consist of different compositions. The 79 % PEN (Fig. 4.36 c), in contrast, shows interconnected islands of 20 nm height and additional 40 nm high small islands.

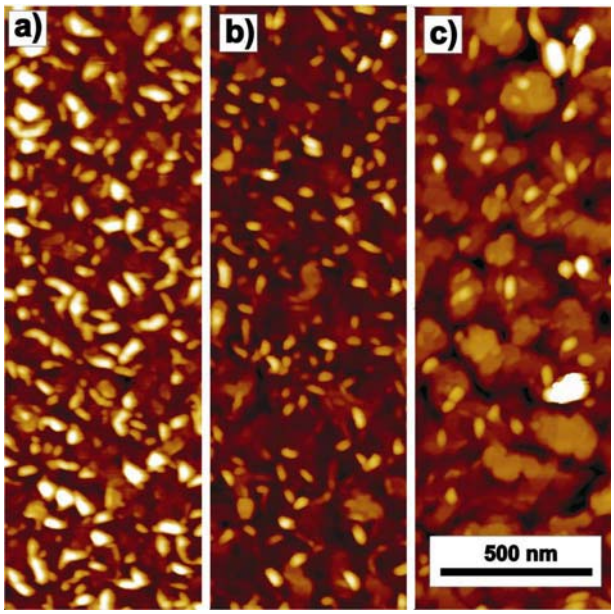

Fig. 4.36: AFM image of 20 nm thick co-deposited PEN/DH6T films: a) 26 % PEN, b) 62 % PEN and c) 79 % PEN.

The specular XRD scan (Fig. 4.37) of a pure PEN film shows the (0 0 *l*) peak series of the TF-PEN phase [20]. Co-deposition of DH6T leads to a weak and broad peak at $q_z = 0.1744$ Å^{-1}, which is assigned to the (0 0 1) peak of DH6T [95] with $d = 3.6$ nm. As the (0 0 1) peak of the TF-PEN [20] phase and the (0 0 2) peak of DH6T are superimposed at very similar q_z values, it is impossible to identify possible small changes of the interlayer spacing. The peak maximal intensities

of the (0 0 1) peaks of PEN and DH6T decreases proportional to respective content in the film. This appoints to phase separation into domains of standing PEN and DH6T molecules

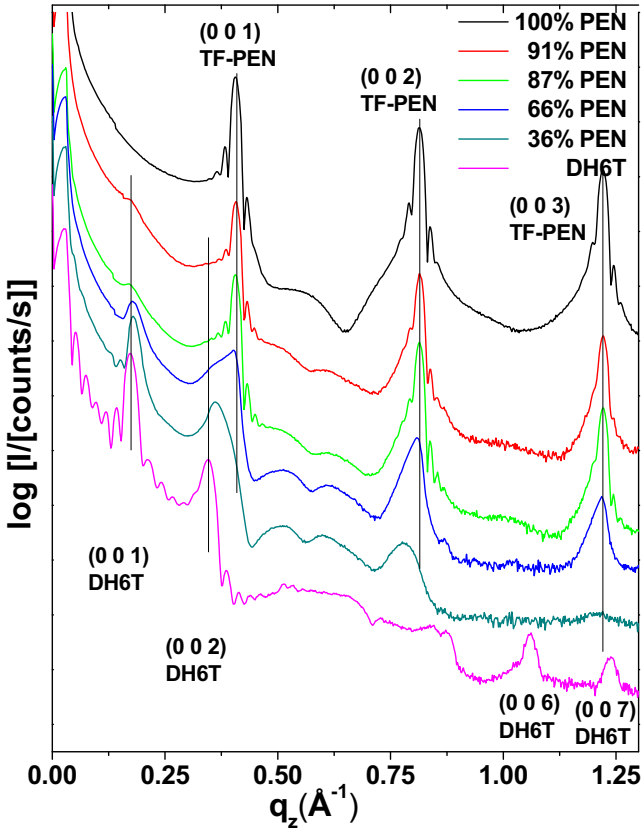

Fig. 4.37: Specular XRD scans of PEN/DH6T co-deposited films on SiO_2 of 40 nm nominal thickness.

The IR spectra (Fig. 4.38) of the DH6T γ(C-H) o.-o.-p. bending vibration peak [84, 85] exhibits an almost negligible blue shift of 1 cm^{-1} compared to 2.5 cm^{-1} for DH6T/6P (Fig. 4.17). The PEN γ(C-H) o.-o.-p peak [19] only shifts by 2 cm^{-1} compared to the strong shift of 5 cm^{-1} and the accompanied strong broadening in the mixed-film spectra of PEN/4T (Fig. 4.3). From all these observations it can be concluded, that PEN and DH6T grow phase separated in ordered domains of standing PEN and standing DH6T.

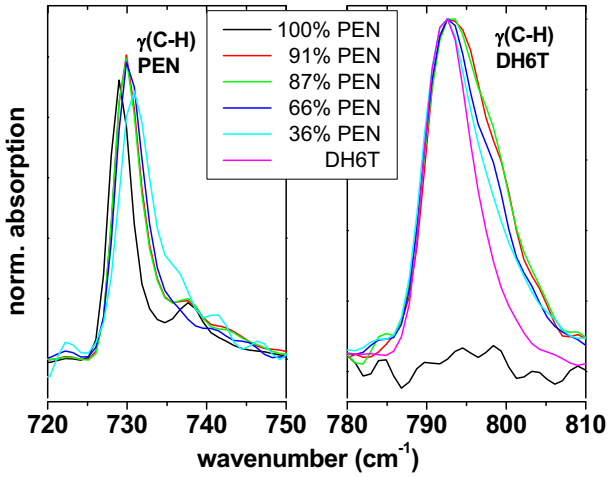

Fig. 4.38: γ(C-H) o.-o.-p vibration peaks of PEN and DH6T are normalized to the peak maximum.

Conclusion

Thin films of the material pairs 4T/DH6T and PEN/DH6T exhibited phase separation of both components. In contrast to the material systems PEN/6T and PEN/6P (cf. section 4.1.3), well ordered domains of standing PEN molecules were observed for PEN/DH6T. The reduced grain size of the PEN/DH6T co-deposited films compared to the 4T/DH6T films indicates stronger substrate - molecule interactions for PEN compared to 4T. This decreases the ability of PEN molecules to diffuse on the substrate leading to a higher nucleation density [50].

4.1.5 Conclusion

Five different rod-like conjugated molecules were co-deposited on silicon oxide substrates. With these five molecules it was possible to form molecular pairs, which differ in the following parameters: electronic properties, the length of the conjugated core, and alkyl-chain-substitution. An overview of the experimental results is given in Table 2. and in Fig. 4.39.

Co-deposition of molecular pairs with similarly sized conjugated cores like 4T/PEN and 6T/6P (section 4.1.1) lead to well ordered layered structures with a molecular orientation almost perpendicular to the substrate surface. These molecules mix over a wide range of mixing ratios (30 % - 70 %).

Co-deposition of molecules with similarly sized CC but alkyl-chain-substitution, DH6T/6T and DH6T/6P lead to well ordered films with interconnected islands. An especially appealing property of these films is the possibility to control the interlayer distance *d* with sub-nanometer precision by changing the DH6T content of the film. This effect can be explained by phase separation into an alkyl and aromatic domain for every layer. (Cf. Fig. 4.18) A decrease of the DH6T content in the film leads to less dense packing of the alkyl domain, which results in a decrease of the total interlayer distance *d* due to the flexibility of the alkyl chain. Both, the high degree of order and the interconnected islands of the DH6T/6T films make them predetermined for the use as active layer in organic field effect transistor. This was realized in this work, see section 4.3.

Films of material pairs with differently sized CC in general showed phase separation of the components. A significant difference between films containing 4T or PEN is observed. Films containing 4T showed phase separation from the sub monolayer on, which seeds the growth in separated domains of standing molecules.

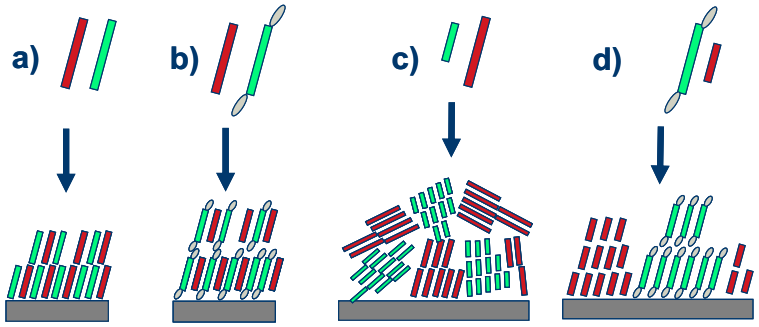

Fig. 4.39: Scheme of experimental findings: a) pairs with similarly sized CC yield ordered mixed films, b) similarly sized CC and alkyl-end-chains yield ordered mixed film, c) dissimilarly sized CC yield phase separation d) additional alkyl chain substitution leads to domains of standing molecules.

In contrast, films containing pentacene showed mixing / micro phase separation for the first one or two layers. This indicates a stronger molecule - substrate interaction of PEN compared to 4T. This is expected, because the strength of the molecule-substrate interaction is (in first order) proportional to the density of binding sites at the molecules [50]. Due to the molecular structure, standing PEN molecules exposes two binding sites towards the substrate, whereas 4T, 6T, and 6P only expose one. For subsequent growth, the resulting mixed / micro phase separated first layer acts as rough substrate, which results in phase separated films of high corrugation and small domain size.

The material pairs with dissimilar CC length and alkyl-chain-substitution, DH6T/4T and DH6T/PEN, showed phase separation into well ordered domains. The alkyl chain substitution seems to promote phase separation into well ordered domains of standing molecules compared to molecular pairs with dissimilar CC length and lacking alkyl-chain-substitution.

Table 2: Phase separation and mixing between rod-like conjugated molecules in co-deposited thin films grown on silicon oxide.

	PEN	**4T**	**6T**	**6P**	**DH6T**
PEN		**Mixing**	Phase separation	Phase separation	Phase separation
4T	**Mixing**		Phase separation	Phase separation	Phase separation
6T	Phase separation	Phase separation		**Mixing**	**Mixing**
6P	Phase separation	Phase separation	**Mixing**		**Mixing**
DH6T	Phase separation	Phase separation	**Mixing**	**Mixing**	

4.2 Thin films on Mylar

The DH6T/6T co-deposited films on silicon oxide show a range of special properties which can be beneficial for the use as active layer in an OFET (cf. section 2.5.2): the growth in interconnected islands, the large domain size, and the possibility to change the inter-layer distance *d* by controlling the mixing ratio. The flexibility of DH6T alkyl chain, which is responsible for the gradual change of *d,* can possibly be able to adapt to the roughness of the substrate. This would lead to an increased order in the aromatic domain of the film which is a prerequisite for high charge carrier mobility. It is therefore of high interest to study the morphology of this films on a rather rough substrate like the PET foil Mylar, which is used to build all organic FETs [101]. The bare Mylar substrate has a RMS-roughness of about 1 to 2 nm. For tapping mode AFM measurements the backside of the Mylar was supported by a thick, casted layer of epoxy resin. This is necessary because the very thin Mylar foil would act as microphone membrane without the rigid support. The resulting AFM height images are shown in Fig. 4.40. The pure DH6T film and the 37 % 6T film exhibit a very similar topology to the films grown on SiO_2. (Cf. Fig. 4.10). The typical 3 layer high interconnected islands are observable with a similar grain density. The pure 6T film exhibits, on the other hand, only half the grain size compared to the 6T films on SiO_2. Further, several fibrous structures are observable. It seems that the alkyl chain substitution actually improves the order of the film on rough substrates.

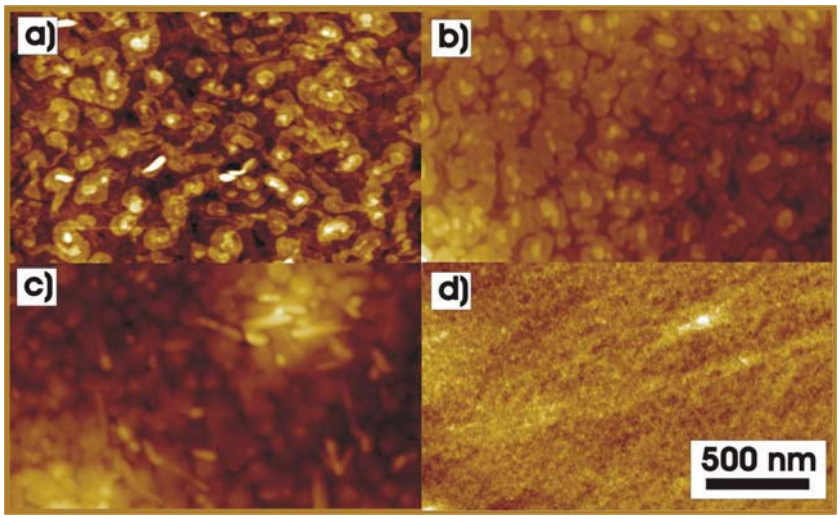

Fig. 4.40: AFM images of co-deposited 6T/DH6T films of 20 nm thickness on Mylar: a) DH6T, b) 37 % 6T, c) 100 % 6T, and d) neat Mylar substrate with RMS-roughness of 1 - 2 nm.

The specular XRD scan (Fig. 4.41) shows only first order reflections at q_z = 0.1708 Å^{-1} (DH6T), q_z = 0.1763 Å^{-1} (37 % 6T), q_z = 0.2035 Å^{-1} (64 % 6T) and q_z = 0.2666 Å^{-1} (100 % 6T). The resulting interlayer distances d in dependence of the 6T content are shown in Fig. 4.12. The lower intensity of the pure 6T diffraction peak manifest the lower order of the 6T compared to the DH6T containing films. The higher order of the mixed films can be explained by the flexibility of the DH6T alkyl chain which can adjust to the rough substrate.

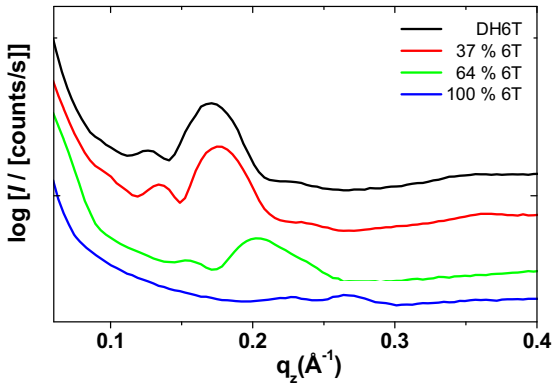

Fig. 4.41: Specular XRD scan of co-deposited 6T/DH6T films of 20 nm thickness on Mylar.

4.3 Application in organic thin film transistors

In this section it will be shown how a proper engineering of the organic active layer can be used as a tool for fine tuning the electrical properties in OFETs. In particular it will be shown that using co-deposited films of DH6T and 6T as active layer with different mixing ratios leads to a wide and predictable tunability of the threshold voltage V_T without negatively affecting charge carrier transport within the device channel. It will be demonstrated that this unique property is correlated with the ability of DH6T and 6T to inter-mix and to form well ordered layers of standing molecules. These properties were even observed using two very different substrates like Mylar and SiO_2 which allows the generalization of these results for many OFET structures.

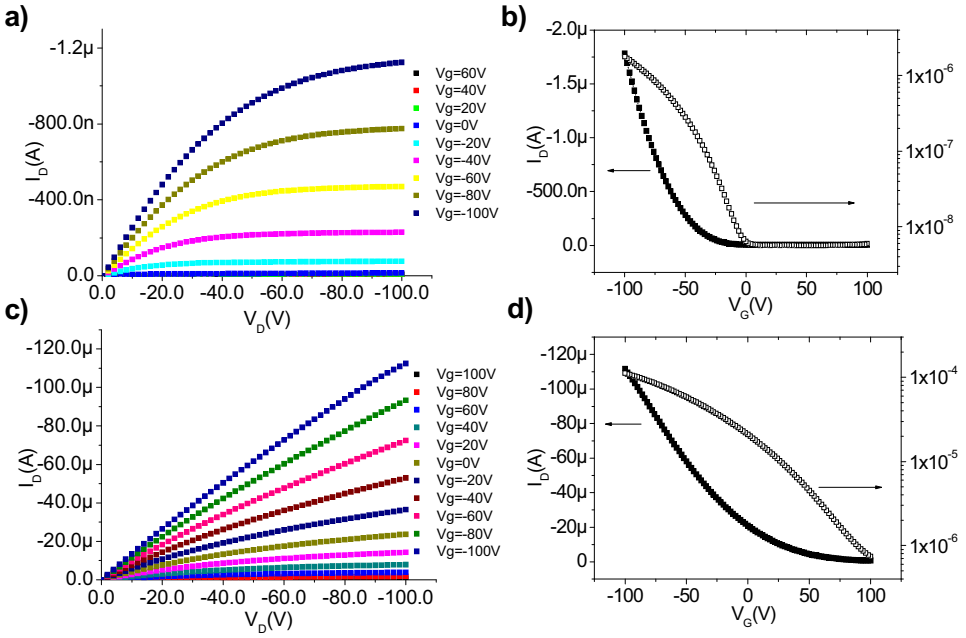

Fig. 4.42: Electrical measurement recorded on bottom contact devices with Au source and drain electrodes assembled on Mylar: a) I_D vs. V_D, b) I_D vs. V_G of a 100 % 6T device, c) I_D vs. V_D, and d) I_D vs. V_G of a 100 % DH6T device. From [Adv.Mater.[102]]

Despite their very similar chemical structure, 6T and DH6T gave rise to a very different electrical behavior, see Fig. 4.42 and data reported in Table 3. The reported mobility values are comparable with the data already reported in the literature [38, 39]. The higher mobility of DH6T was attributed to the alkyl chain substitution by Garnier et al. [38] and Facchetti et al. [39]. The general lower mobility on Mylar can be explained by the higher surface roughness (~1 nm) compared to

SiO_2 (~0.2 nm). This causes a lower order and smaller grain size in the film especially for the pure 6T film. However, also a very pronounced difference in the threshold voltages V_T of the two employed materials can be pointed out. In fact, 6T devices usually showed a slightly negative V_T and seem to work as unipolar OFETs in the enhancement regime. On the other hand, DH6T devices always showed a high positive V_T. This means that, charge carriers are accumulated at the gate dielectric interface even without applying any gate bias, and a high positive gate bias is required to fully deplete the channel from charge carriers. As a result, in this case, the devices are reproducible working in the depletion regime using very different devices geometries and gate dielectrics.

Table 3: Mobility and threshold voltage of devices of pure 6T and pure DH6T active layer. From [Adv.Mater.[102]]

Substrate	Active material	μ (cm^2/Vs)	V_T (V)
Mylar	6T	2.6×10^{-3}	-15
	DH6T	3.5×10^{-2}	+71
Silicon	6T	1.75×10^{-2}	+2
	DH6T	7.5×10^{-2}	+42

This behavior can have two reasons: a more efficient charge injection and a more pronounced p-type doping induced by oxygen since the device comes into contact with oxygen after device preparation. In fact, both mechanism are effects of the lower ionization energy (IE) of DH6T (4.8 eV) compared to the one of 6T (5.0 eV) [37]. The lower IE of DH6T results in a lower hole injection barrier compared to the 6T-electrode interface. The more efficient charge injection results in a higher hole concentration. On the other hand, the p-type doping of DH6T is more efficient than for 6T because of the lower IE. This could be proven by annealing of the devices in an inert gas atmosphere. (Fig. 4.43). The DH6T devices show a pronounced V_T shift to lower positive voltages. The 6T devices show instead no significant shifts. The effect of the oxygen doping is proven by the fact that this process is fully reversible, since the exposure to ambient conditions leads to a strong increase of the threshold voltage (Cf. inset Fig. 4.43).

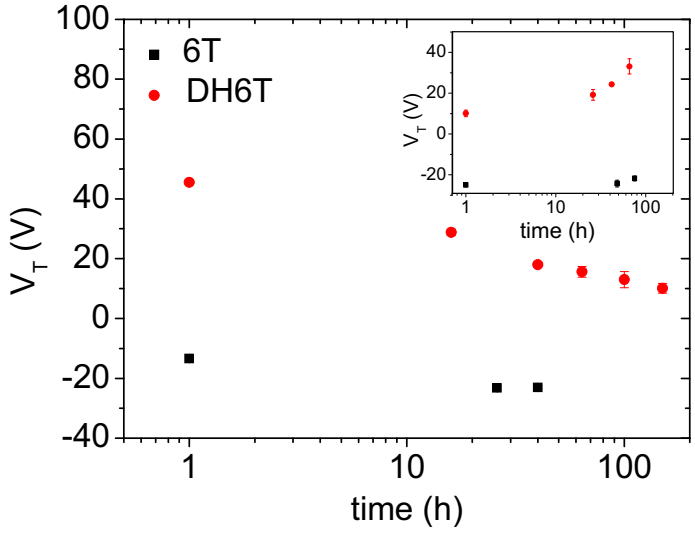

Fig. 4.43: Effect of the annealing in inert atmosphere at 120°C on V_T of the devices with pure 6T and DH6T active layer. The subsequent exposure of the devices to air re-establishes the initial high V_T values (inset), i.e. the doping is fully reversible. [Adv.Mater. [102]]

Starting from these considerations, a set of OFETs, with different gate dielectrics and different geometries, using co-deposited 6T/DH6T as active layer are realized. Very interestingly, as can be noticed by the plots reported in Fig. 4.44 and Fig. 4.45, an almost linear dependence of the V_T as a function of the 6T content within the active layer can be found. Moreover, the charge carrier mobility does not seem to be strongly influenced by the co-deposition process. All the measured devices, with mixed active layers, show an almost constant mobility. This feature is found to be reproducible for all the different sets of devices that were realized and measured. As a result, this seems to be an intrinsic property of the employed active layer, and to be independent of the geometry and gate dielectric of the assembled devices.

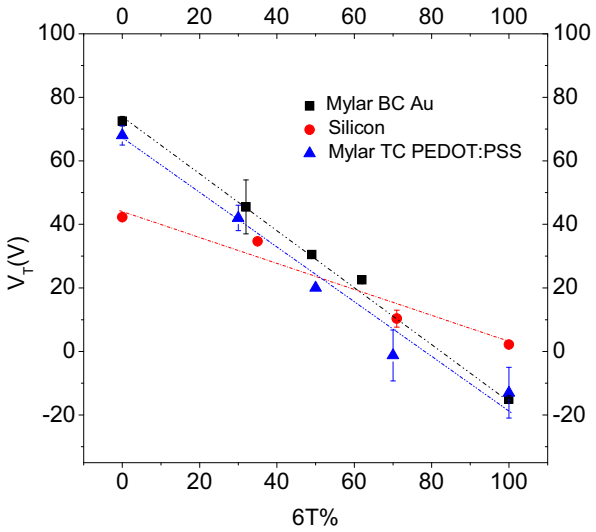

Fig. 4.44: Threshold voltage V_T vs. 6T content in the DH6T/6T OFET active layer. The measured OFETs are top (TC) and bottom contact (BC) devices on Mylar and bottom contact device realized on silicon oxide. From [Adv.Mater. [102]]

This weak dependence of μ on the film composition (Fig. 4.45) can be rationalized by the observation that co-deposited mixed films of 6T and DH6T adopt well ordered layered structures, without phase separation, for all mixing ratios [95]. As a result, no degradation of mobility is provoked by structural and morphological changes induced by co-deposition.

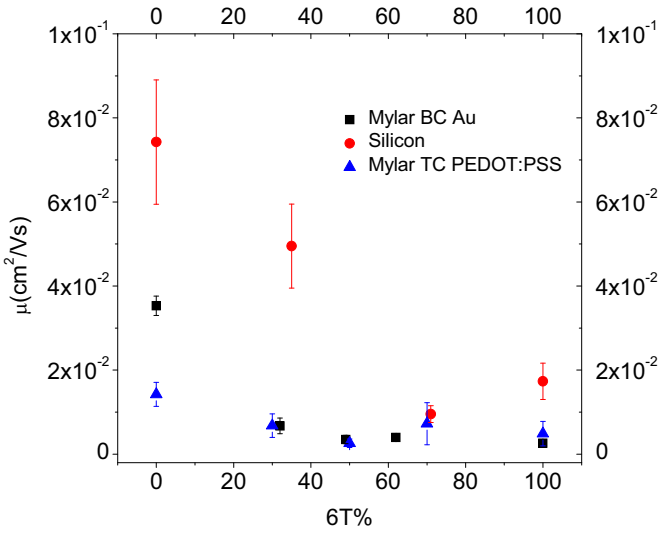

Fig. 4.45: Mobility μ vs. 6T content in the OFET DH6T/6T active layer. Measured on top (TC) and bottom contact (BC) devices on Mylar and bottom contact device on silicon. From [Adv.Mater.[102]]

In conclusion, I have demonstrated that it is possible to finely tune the electronic properties of OFETs with an active layer formed by two mixed organic semiconductors that: (i) have a different ionization energy (resulting in a different affinity towards oxygen doping and in a different hole injection barrier); (ii) are able to uniformly mix over a large range of mixing ratios and on various substrates. The key effect is to control the density of mobile charge carriers in the OFET channel region by oxygen doping, which can be precisely tuned by controlling the layer composition. This is comparable to the p-type doping in inorganic electronics. I expect that this has the advantage of a lower diffusion in the organic layer compared to commonly used dopants like Iodine [103].

This is a rational approach to precisely control OFET performance. Moreover, this approach had been applied even to not ideal gate dielectrics (as Mylar®), and it is therefore suitable for tuning the electrical properties in flexible plastic devices, providing a considerable extension of the application-potential of organic electronics.

5. Conclusion and Outlook

In the first part of this work I have shown that the organic - organic interface is especially important for applications. This work is therefore a thorough study devoted to investigate the molecular properties leading to phase separation and mixing in co-deposited films. In other words: how is it possible to actively control the organic-organic heterolayer morphology by choosing molecules with the proper properties.

This was done by the co-deposition of five rod-like conjugated molecules well known in the context of organic electronics, which differ in the parameters: optical and electric properties, conjugated core length, and alkyl-chain substitution.

For molecule pairs with differently sized conjugated cores, I observed pronounced phase separation (Cf. Table 2). Some material pairs (4T/6T, 4T/6P, 4T/DH6T, PEN/DH6T) showed phase separation into domains of well ordered molecules. So far the domain sizes do not fulfill the optimal requirements for organic heterojunction solar cells, but I am hopeful that it is possible to optimize domain size and island density by optimizing the process parameters deposition rate and substrate temperature.

However, molecule pairs with similarly sized conjugated cores (4T/PEN, 6T/6P) show very well ordered mixed layered structures of standing molecules over a wide range of mixing ratios. This is a surprising result, since mixed crystals and films have so far only been reported in the context of charge transfer complexes (organic metals) [104], solution processed films in the monolayer range [5, 105, 106, 107, 108, 109], and isotopic mixed crystals [69]. The layered mixed films could be of use as a guest-matrix system in which the guest molecules are embedded in a highly ordered way. It would be possible to study the guest-guest interaction under different concentrations as it was done in studies of the Davidov splitting [69] in isotopic mixed crystals.

The co-deposited films of the alkylated DH6T with non alkylated 6T and 6P show a very appealing feature. It is possible to control the interlayer distance *d* with sub-nm precision by controlling the ratio between the components. As example for a possible application the material pair 6T/DH6T was used as active layer in an OFET. The measurements showed that it was possible to tune the OFET from the enhancement to the depletion regime by changing the composition of the active layer while preserving a high charge carrier mobility. This could

be explained by the difference in the ionization energy of DH6T and 6T which leads to different susceptibilities to p-type doping by ambient oxygen. The co-deposition of the two materials enables us to control the density of free charge carriers in the OFET channel by oxygen doping. The high order of the mixed films results in an high charge carrier mobility. It has been shown that it is possible to control one of the most important OFET parameters by changing the composition of the active layer which is comparable to the p-type doping in inorganic electronics.

Another possible application for mixed layered structures could be to study the interaction between the aromatic core and the metal substrate in dependence of separation between conjugated core and substrate in a photoemission experiment.

This work has focused on a part of *organic electronics* which has not been studied in detail yet. It has been shown that the co-deposition of two materials can lead to phase separation or mixing between two components. Further efforts have to be undertaken to systematically study which material properties are responsible for the different film growth behaviors. The DH6T/6T OFETs have shown that a small change in the molecular ionization energy can have a large effect. It is therefore of future interest to study intermixing systems with larger difference in the electrical properties.

Publications

- "Sub-nanometer Control of the Interlayer Spacing in Thin Films of Intercalated Rodlike Conjugated Molecules" **Jörn-Oliver Vogel, Ricarda Opitz, Ingo Salzmann, Steffen Duhm, Bert Nickel, Jürgen P. Rabe, and Norbert Koch** The Journal of Physical Chemistry B (2007), 111, 14097
- "Continuous Tuning of Organic Transistor Operation from Enhancement to Depletion Mode" **Piero Cosseddu, Jörn-Oliver Vogel, Beatrice Fraboni, Jürgen P. Rabe, Norbert Koch, and Annalisa Bonfiglio** Advanced Materials (2009), 21, 3, 344
- "Photocurrent studies of sexythiophene-based OFETs" **B. Fraboni R. DiPietro, A. Cavallini, P. Cosseddu, A.. Bonfiglio, andJ.-O. Vogel** Applied Physics A (2009), 95 ,37
- "Highly ordered hetero films of co-deposited rod-like conjugated molecules" **Jörn-Oliver Vogel, Ingo Salzmann, Steffen Duhm, Jürgen P. Rabe, and Norbert Koch** Journal of Materials Chemistry (in preparation)

Contributions to conferences

- Talk: "Sub-nm control of the inter-layer spacing in thin films of intercalated rod-like conjugated molecules" **Jörn-Oliver Vogel, Ricarda Opitz, Ingo Salzmann, Steffen Duhm, Bert Nickel, Jürgen P. Rabe, and Norbert Koch** DPG Frühjahrstagung in Regensburg 2007
- Talk: "Co-deposited thin films of rod-like conjugated molecules: from phase separation to intercalation" **Jörn-Oliver Vogel, Ricarda Opitz, Ingo Salzmann, Steffen Duhm, Bert Nickel, Jürgen P. Rabe, and Norbert Koch** European Conference on Molecular Electronics 2007 in Metz, France
- Talk: "Mixing and phase-separation in co-deposited films of rod-like conjugated molecules" **Jörn-Oliver Vogel, Ricarda Opitz, Ingo Salzmann, Steffen Duhm, Bert Nickel, Jürgen P. Rabe and Norbert Koch** DPG Frühjahrstagung 2008 in Berlin, Germany
- Talk: "Intercalation and phase separation in thin films of rodlike conjugated molecules: Controlling the local molecular environment" **Jörn-Oliver Vogel, Ingo Salzmann, Steffen Duhm, Jürgen P. Rabe, and Norbert Koch** E-MRS 2008 Spring Meeting in Strasbourg, France

- Poster: "Mixing and phase-separation in co-deposited films of rod-like conjugated molecules" **Jörn-Oliver Vogel, Ingo Salzmann, Steffen Duhm, Jürgen P. Rabe, and Norbert Koch** The 8th International Symposium on Functional π-Electron Systems in Graz, Austria
- Poster: "Intercalation and Phase Separation in Co-Deposited thin Films of Rodlike Conjugated Molecules" **Jörn-Oliver Vogel, Ingo Salzmann, Steffen Duhm, Jürgen P. Rabe, and Norbert Koch** Materials Science and Engineering 2008 in Nürnberg, Germany
- Poster:" Co-deposited Films of Rod-like Conjugated Molecules: Mixing versus Phase Separation." **Jörn-Oliver Vogel, Ingo Salzmann, Steffen Duhm, Bert Nickel, Jürgen P. Rabe, and Norbert Koch** MRS 2009 Spring Meeting in San Francisco, USA

Bibliography

[1] Pochettino, A (1906): Acad.Lincei,Rendiconti (volume 15), pp. 355.

[2] Aviram, A. and Ratner, M. A. (1974): Molecular Rectifiers, Chemical Physics Letters (volume 29), issue 2, pp. 277-283. URL: ISI:A1974U851400031

[3] Herwig, P. T. and Müllen, K. (1999): A soluble pentacene precursor: Synthesis, solid-state conversion into pentacene and application in a field-effect transistor, Advanced Materials (volume 11), issue 6, pp. 480-+. URL: ISI:000080306400016

[4] Lehn, J. M. (1994): Supramolecular Chemistry (Reprinted from Science, Vol 260, Pg 1762-1763, 1993), Proceedings of the Indian Academy of Sciences-Chemical Sciences (volume 106), issue 5, pp. 915-922. URL: ISI:A1994QG60600002

[5] Jackel, F.; Wang, Z.; Watson, M. D.; Mullen, K. and Rabe, J. P. (2004): Prototypical single-molecule transistors with supramolecular gates: varying dipole orientation, Synthetic Metals (volume 146), issue 3, pp. 269-272. URL: ISI:000225302800009

[6] Chen, J.; Reed, M. A.; Rawlett, A. M. and Tour, J. M. (1999): Large on-off ratios and negative differential resistance in a molecular electronic device, Science (volume 286), issue 5444, pp. 1550-1552. URL: ISI:000083768300055

[7] Rand, B. P.; Xue, J. G.; Uchida, S. and Forrest, S. R. (2005): Mixed donor-acceptor molecular heterojunctions for photovoltaic applications. I. Material properties, Journal of Applied Physics (volume 98), issue 12. URL: ISI:000234339700075

[8] Kuhlbrandt, W. (1995): Structure and Function of Bacterial Light-Harvesting Complexes, Structure (volume 3), issue 6, pp. 521-525. URL: ISI:A1995RH53500001

[9] Dekker, J. P. and Van Grondelle, R. (2000): Primary charge separation in Photosystem II, Photosynthesis Research (volume 63), issue 3, pp. 195-208. URL: ISI:000089986800002

[10] Wolfe, S. L (1993): Molecular and Cellular Biology, Wadsworth Publishing Company, ISBN: 978-0534124083.

[11] Barth, J. V.; Costantini, G. and Kern, K. (2005): Engineering atomic and molecular nanostructures at surfaces, Nature (volume 437), issue 7059, pp. 671-679. URL: ISI:000232157900041

[12] Nishiyama, F.; Yokoyama, T.; Kamikado, T.; Yokoyama, S.; Mashiko, S.; Sakaguchi, K. and Kikuchi, K. (2007): Interstitial accommodation of C-60 in a surface-supported supramolecular network, Advanced Materials (volume 19), issue 1, pp. 117-+. URL: ISI:000243619500015

[13] Yang, F.; Shtein, M. and Forrest, S. R. (2005): Morphology control and material mixing by high-temperature organic vapor-phase deposition and its application to thin-film solar cells, Journal of Applied Physics (volume 98), issue 1. URL: ISI:000231062200117

[14] Peumans, P.; Uchida, S. and Forrest, S. R. (2003): Efficient bulk heterojunction photovoltaic cells using small-molecular-weight organic thin films, Nature (volume 425), issue 6954, pp. 158-162. URL: ISI:000185236000036

[15] Han, E. M.; Do, L. M.; Yamamoto, N. and Fujihira, M. (1996): Crystallization of organic thin films for electroluminescent devices, Thin Solid Films (volume 273), issue 1-2, pp. 202-208. URL: ISI:A1996UM53400036

[16] Porzio, W.; Giovanella, U.; Pasini, M.; Botta, C.; Destri, S. and Provasi, C. (2004): Thiophene-fluorene oligomer films growth in ultra high vacuum for efficient energy transfer, Thin Solid Films (volume 466), issue 1-2, pp. 231-237. URL: ISI:000224019300035

[17] Salzmann, I.; Opitz, R.; Rogaschewski, S.; Rabe, J. P.; Koch, N. and Nickel, B. (2007): Phase separation in vacuum codeposited pentacene/6,13-pentacenequinone thin films, Physical Review B (volume 75), issue 17. URL: ISI:000246890500036

[18] Siegrist, T.; Kloc, C.; Laudise, R. A.; Katz, H. E. and Haddon, R. C. (1998): Crystal growth, structure, and electronic band structure of alpha-4T polymorphs, Advanced Materials (volume 10), issue 5, pp. 379-382. URL: ISI:000072913500002

[19] Lee, J.; Kim, S. S.; Kim, K.; Kim, J. H. and Im, S. (2004): Correlation between photoelectric and optical absorption spectra of thermally evaporated pentacene films, Applied Physics Letters (volume 84), issue 10, pp. 1701-1703. URL: ISI:000189384900027

[20] Dimitrakopoulos, C. D.; Brown, A. R. and Pomp, A. (1996): Molecular beam deposited thin films of pentacene for organic field effect transistor applications, Journal of Applied Physics (volume 80), issue 4, pp. 2501-2508. URL: ISI:A1996VD53200078

[21] Campbell, R. B.; Trotter, J. and Monteath, J. (1962): Crystal Structure of Hexacene, and A Revision of Crystallographic Data for Tetracene and Pentacene, Acta Crystallographica (volume 15), issue 3, pp. 289-&. URL: ISI:A19621311A00004

[22] Siegrist, T.; Kloc, C.; Schon, J. H.; Batlogg, B.; Haddon, R. C.; Berg, S. and Thomas, G. A. (2001): Enhanced physical properties in a pentacene polymorph, Angewandte Chemie-International Edition (volume 40), issue 9, pp. 1732-1736. URL: ISI:000168630100043

[23] Nabok, D.; Puschnig, P.; Ambrosch-Draxl, C.; Werzer, O.; Resel, R. and Smilgies, D. M. (2007): Crystal and electronic structures of pentacene thin films from grazing-incidence x-ray diffraction and first-principles calculations, Physical Review B (volume 76), issue 23. URL: ISI:000251986500081

[24] Yoshida, H.; Inaba, K. and Sato, N. (2007): X-ray diffraction reciprocal space mapping study of the thin film phase of pentacene, Applied Physics Letters (volume 90), issue 18. URL: ISI:000246210000061

[25] Schiefer, S.; Huth, M.; Dobrinevski, A. and Nickel, B. (2007): Determination of the crystal structure of substrate-induced pentacene polymorphs in fiber structured thin films, Journal of the American Chemical Society (volume 129), issue 34, pp. 10316-+. URL: ISI:000249035200009

[26] Holmes, D.; Kumaraswamy, S.; Matzger, A. J. and Vollhardt, K. P. C. (1999): On the nature of nonplanarity in the [N]phenylenes, Chemistry-A European Journal (volume 5), issue 11, pp. 3399-3412. URL: ISI:000083640300033

[27] Minakata, T.; Ozaki, M. and Imai, H. (1993): Conducting Thin-Films of Pentacene Doped with Alkaline-Metals, Journal of Applied Physics (volume 74), issue 2, pp. 1079-1082. URL: ISI:A1993LM78200049

[28] Hopmeier, M.; Gebauer, W.; Oestreich, M.; Sokolowski, M.; Umbach, E. and Mahrt, R. F. (1999): Relaxation dynamics of excitons in thin quaterthiophene films on different substrates, Chemical Physics Letters (volume 314), issue 1-2, pp. 9-15. URL: ISI:000083955300002

[29] Antolini, L.; Horowitz, G.; Kouki, F. and Garnier, F. (1998): Polymorphism in oligothiophenes with an even number of thiophene subunits, Advanced Materials (volume 10), issue 5, pp. 382-385. URL: ISI:000072913500003

[30] Sun, H.; Zhao, Z.; Spano, F. C.; Beljonne, D.; Cornil, J.; Shuai, Z. and Bredas, J. L. (2003): Absorption and emission in quaterthienyl thin films, Advanced Materials (volume 15), issue 10, pp. 818-+. URL: ISI:000183246100015

[31] Fichou, D. (2000): Structural order in conjugated oligothiophenes and its implications on opto-electronic devices, Journal of Materials Chemistry (volume 10), issue 3, pp. 571-588. URL: ISI:000085886200001

[32] Garnier, F.; Horowitz, G.; Peng, X. H. and Fichou, D. (1990): An All-Organic Soft Thin-Film Transistor with Very High Carrier Mobility, Advanced Materials (volume 2), issue 12, pp. 592-594. URL: ISI:A1990ER11100006

[33] Gundlach, D. J.; Lin, Y. Y.; Jackson, T. N. and Schlom, D. G. (1997): Oligophenyl-based organic thin film transistors, Applied Physics Letters (volume 71), issue 26, pp. 3853-3855. URL: ISI:000071184700036

[34] Yanagi, H.; Okamoto, S. and Mikami, T. (1997): Organic electroluminescent device with epitaxial p-sexiphenyl films, Synthetic Metals (volume 91), issue 1-3, pp. 91-93. URL: http://www.sciencedirect.com/science/article/B6TY7-3W0G003-1C/2/5ae9753134d9d51114e5ff173a452c2c

[35] Tasch, S.; Brandstatter, C.; Meghdadi, F.; Leising, G.; Froyer, G. and Athouel, L. (1997): Red-green-blue light emission from a thin film electroluminescence device based on parahexaphenyl, Advanced Materials (volume 9), issue 1, pp. 33-&. URL: ISI:A1997WE10200003

[36] Resel, R. (2003): Crystallographic studies on hexaphenyl thin films - a review, Thin Solid Films (volume 433), issue 1-2, pp. 1-11. URL: ISI:000183716900002

[37] Duhm, S.; Glowatzki, H.; Rabe, J. P.; Koch, N. and Johnson, R. L. (2006): Influence of alkyl chain substitution on sexithienyl-metal interface morphology and energetics, Applied Physics Letters (volume 88), issue 20. URL: ISI:000237682100072

[38] Garnier, F.; Yassar, A.; Hajlaoui, R.; Horowitz, G.; Deloffre, F.; Servet, B.; Ries, S. and Alnot, P. (1993): Molecular Engineering of Organic Semiconductors - Design of Self-Assembly Properties in Conjugated Thiophene Oligomers, Journal of the American Chemical Society (volume 115), issue 19, pp. 8716-8721. URL: ISI:A1993LZ13300026

[39] Facchetti, A.; Mushrush, M.; Yoon, M. H.; Hutchison, G. R.; Ratner, M. A. and Marks, T. J. (2004): Building blocks for n-type molecular and polymeric electronics. Perfluoroalkyl-versus alkyl-functionalized oligothiophenes (nT; n=2-6). Systematics of thin film microstructure, semiconductor performance, and modeling of majority charge injection in field-effect transistors, Journal of the American Chemical Society (volume 126), issue 42, pp. 13859-13874. URL: ISI:000224685200066

[40] Koch, N. (2007): Organic electronic devices and their functional interfaces, Chemphyschem (volume 8), issue 10, pp. 1438-1455. URL: ISI:000248251100001

[41] Atkins, P. W. (1998): Physical Chemistry, 6. edition , oxford, ISBN: 019850102.

[42] Schwoerer, Markus and Wolf, H (2007): Organic Molecular Solids, Wiley-VCH, ISBN: 978-3-527-40540-4.

[43] Borsenberger, P. M.; Pautmeier, L. and Bassler, H. (1991): Hole Transport in Bis(4-N,N-Diethylamino-2-Methylphenyl)-4-Methylphenylmethane, Journal of Chemical Physics (volume 95), issue 2, pp. 1258-1265. URL: ISI:A1991FV97600066

[44] (1996): Kittel,Charles, Wiley, ISBN: 0-471-11181-3.

[45] Vissenberg, M. C. J. M. and Matters, M. (1998): Theory of the field-effect mobility in amorphous organic transistors, Physical Review B (volume 57), issue 20, pp. 12964-12967. URL: ISI:000073999400046

[46] Hertel, D. and Bassler, H. (2008): Photoconduction in amorphous organic solids, Chemphyschem (volume 9), issue 5, pp. 666-688. URL: ISI:000255082600001

[47] Koch, N. (2008): Energy levels at interfaces between metals and conjugated organic molecules, Journal of Physics-Condensed Matter (volume 20), issue 18. URL: ISI:000255661200010

[48] Facchetti, A.; Yoon, M. H.; Stern, C. L.; Hutchison, G. R.; Ratner, M. A. and Marks, T. J. (2004): Building blocks for N-type molecular and polymeric electronics. Perfluoroalkyl- versus alkyl-functionalized ligothiophenes (nTs; n=2-6). Systematic synthesis, spectroscopy, electrochemistry, and solid-state organization, Journal of the American Chemical Society (volume 126), issue 41, pp. 13480-13501. URL: ISI:000224500000067

[49] Locklin, J.; Roberts, M. E.; Mannsfeld, S. C. B. and Bao, Z. N. (2006): Optimizing the thin film morphology of organic field-effect transistors: The influence of molecular structure and vacuum deposition parameters on device performance, Polymer Reviews (volume 46), issue 1, pp. 79-101. URL: ISI:000240473300005

[50] Verlaak, S.; Steudel, S.; Heremans, P.; Janssen, D. and Deleuze, M. S. (2003): Nucleation of organic semiconductors on inert substrates, Physical Review B (volume 68), issue 19. URL: ISI:000187163000098

[51] Yanagisawa, H.; Tamaki, T.; Nakamura, M. and Kudo, K. (2004): Structural and electrical characterization of pentacene films on SiO2 grown by molecular beam deposition, Thin Solid Films (volume 464-65), pp. 398-402. URL: ISI:000223988000091

[52] Wu, Y.; Toccoli, T.; Koch, N.; Iacob, E.; Pallaoro, A.; Rudolf, P. and Iannotta, S. (2007): Controlling the early stages of pentacene growth by supersonic molecular beam deposition, Physical Review Letters (volume 98), issue 7. URL: ISI:000244250300043

[53] Durr, A. C.; Nickel, B.; Shan-Fia, V.; Taffner, U. and Dosch, H. (2006): Observation of competing modes in the growth of diindenoperylene on SiO2, Thin Solid Films (volume 503), issue 1-2, pp. 127-132. URL: ISI:000236440500020

[54] Heringdorf, F. J. M. Z.; Reuter, M. C. and Tromp, R. M. (2001): Growth dynamics of pentacene thin films, Nature (volume 412), issue 6846, pp. 517-520. URL: ISI:000170202900039

[55] Knupfer, M. (2003): Exciton binding energies in organic semiconductors, Applied Physics A-Materials Science & Processing (volume 77), issue 5, pp. 623-626. URL: ISI:000184503400004

[56] Forrest, S. R. (2005): The limits to organic photovoltaic cell efficiency, Mrs Bulletin (volume 30), issue 1, pp. 28-32. URL: ISI:000226355800017

[57] Manunza, I. and Bonfiglio, A. (2007): Pressure sensing using a completely flexible organic transistor, Biosensors & Bioelectronics (volume 22), issue 12, pp. 2775-2779. URL: ISI:000247555300001

[58] Rost, H and Mildner, W (2008): On the Way to Printed Electronics, Kunststoffe International (volume 6), pp. 98.

[59] Wang, Y.; Liu, Y. Q.; Song, Y. B.; Ye, S. H.; Wu, W. P.; Guo, Y. L.; Di, C. A.; Sun, Y. M.; Yu, G. and Hu, W. P. (2008): Organic field-effect transistors with a low pinch-off voltage and a controllable threshold voltage, Advanced Materials (volume 20), issue 3, pp. 611-+. URL: ISI:000253325500043

[60] Cosseddu, P. (2007): Correlation between interface-dependent properties and electrical performances in OFETs . URL: www.diee.unica.it/DRIEI/

[61] Serway, Raymond (1990): Physics for Scientists and Engineers with Modern Physics, Saunders College Publishing. URL: http://hyperphysics.phy-astr.gsu.edu/hbase/kinetic/menfre.html#c2

[62] Binning, G.; Rohrer, H.; Gerber, C. and Weibel, E. (1982): Surface Studies by Scanning Tunneling Microscopy, Physical Review Letters (volume 49), issue 1, pp. 57-61. URL: ISI:A1982NV44300017

[63] Binnig, G.; Quate, C. F. and Gerber, C. (1986): Atomic Force Microscope, Physical Review Letters (volume 56), issue 9, pp. 930-933. URL: ISI:A1986A543600013

[64] Meyer, G. and Amer, N. M. (1988): Novel Optical Approach to Atomic Force Microscopy, Applied Physics Letters (volume 53), issue 12, pp. 1045-1047. URL: ISI:A1988Q163900008

[65] Meyer, E.; Jarvis, S. R. and Spencer, N. D. (2004): Scanning probe Microscopy in materials science, Mrs Bulletin (volume 29), issue 7, pp. 443-448. URL: ISI:000222764200012

[66] Israelachvili, j (1985): Intermolecular and Surface Forces, Academic Press, London.

[67] Stifter, T.; Marti, O. and Bhushan, B. (2000): Theoretical investigation of the distance dependence of capillary and van der Waals forces in scanning force microscopy, Physical Review B (volume 62), issue 20, pp. 13667-13673. URL: ISI:000165556400053

[68] Davydov, A. S. (1962): Therory of molecular excitons, Mc Graw Hill, New York.

[69] Port, H.; Rund, D. and Wolf, H. C. (1981): Triplet-States in Isotopically Mixed Anthracene-Crystals - High-Resolution Optical Spectroscopy, Chemical Physics (volume 60), issue 1, pp. 81-98. URL: ISI:A1981MH65400007

[70] Christiansen, c (1884): Ann.Phys.Chem. (volume 23), pp. 298.

[71] Franz, M.; Fischer, B. M. and Walther, M. (2008): The Christiansen effect in terahertz time-domain spectra of coarse-grained powders, Applied Physics Letters (volume 92), issue 2. URL: ISI:000252470900007

[72] Price, W. C. and Tetlow, K. S. (1948): Infra-Red Christiansen Filter Effect in Slurries of Organic Crystals, Journal of Chemical Physics (volume 16), issue 12, pp. 1157-1162. URL: ISI:A1948XV18300009

[73] Pedrotti, F.; Pedrotti , L.; Bausch, W. and Schmidt, H. (2008): Optik: Eine Einführung, Pearson Education Deutsch, ISBN: 978-3827295101.

[74] Herres, W. and Gronholz, J. (1984): Datenverarbeitung in der FTIR-Spektroskopien, Teil 1: Datenaufnahme, Computer Anwendung im Labor (volume 5), pp. 352.

[75] Herres, W. and Gronholz, J. (1984): Datenverarbeitung in der FTIR-Spektroskopie, Teil 2: Einzelheiten in der

Spektrenberechnung, Computer Anwendung im Labor (volume 6), pp. 418.

[76] Herres, W. and Gronholz, J. (1985): "Datenverarbeitung in der FTIR-Spektroskopie, Teil 3: Über einige nützliche

Operationen im Interferogramm- und Zeitbereich, Computer Anwendung im Labor (volume 5), pp. 230.

[77] Günzler, H. and Heise, M. (1996): IR - Spektroskopie: Eine Einführung , 3. edition , ISBN: 3527287590.

[78] Bonfiglio, A.; Mameli, F. and Sanna, O. (2003): A completely flexible organic transistor obtained by a one-mask photolithographic process, Applied Physics Letters (volume 82), issue 20, pp. 3550-3552. URL: ISI:000182823300058

[79] Cosseddu, P. and Bonfiglio, A. (2006): Soft lithography fabrication of all-organic bottom-contact and top-contact field effect transistors, Applied Physics Letters (volume 88), issue 2, pp. 23506. URL: ISI:000234606900081

[80] Ackermann, J.; Videlot, C.; Dumas, P.; El Kassmi, A.; Guglielmetti, R. and Safarov, V. (2004): Control of growth and charge transport properties of quaterthiophene thin films via hexyl chain substitutions, Organic Electronics (volume 5), issue 4, pp. 213-222. URL: ISI:000222042400007

[81] Zorba, S.; Shapir, Y. and Gao, Y. L. (2006): Fractal-mound growth of pentacene thin films, Physical Review B (volume 74), issue 24. URL: ISI:000243195800105

[82] Durr, A. C.; Schreiber, F.; Munch, M.; Karl, N.; Krause, B.; Kruppa, V. and Dosch, H. (2002): High structural order in thin films of the organic semiconductor diindenoperylene, Applied Physics Letters (volume 81), issue 12, pp. 2276-2278. URL: ISI:000177911200045

[83] Warren, B. (1990): X-Ray diffraction, Dover, ISBN: 0-486-66317-5.

[84] Hermet, P.; Bantignies, J. L.; Rahmani, A.; Sauvajol, J. L. and Johnson, M. R. (2005): Polymorphism of crystalline alpha-quaterthiophene and alpha-sexithiophene: Ab initio analysis and comparison with inelastic neutron scattering response, Journal of Physical Chemistry A (volume 109), issue 18, pp. 4202-4207. URL: ISI:000228983000023

[85] Kramer, M. and Hoffman, V. (1998): Infrared spectroscopic characterization of orientation and order of thin oligothiophene films, Optical Materials (volume 9), issue 1-4, pp. 65-69. URL: ISI:000072743500012

[86] Szczepanski, J.; Wehlburg, C. and Vala, M. (1995): Vibrational and Electronic-Spectra of Matrix-Isolated Pentacene Cations and Anions, Chemical Physics Letters (volume 232), issue 3, pp. 221-228. URL: ISI:A1995QC33700006

[87] Siegrist, T.; Fleming, R. M.; Haddon, R. C.; Laudise, R. A.; Lovinger, A. J.; Katz, H. E.; Bridenbaugh, P. and Davis, D. D. (1995): The Crystal-Structure of the High-Temperature Polymorph of Alpha-Hexathienyl (Alpha-U-6T/Ht), Journal of Materials Research (volume 10), issue 9, pp. 2170-2173. URL: ISI:A1995RQ71400004

[88] Baker, K. N.; Fratini, A. V.; Resch, T.; Knachel, H. C.; Adams, W. W.; Socci, E. P. and Farmer, B. L. (1993): Crystal-Structures, Phase-Transitions and Energy Calculations of Poly(P-Phenylene) Oligomers, Polymer (volume 34), issue 8, pp. 1571-1587. URL: ISI:A1993KZ00400001

[89] Zojer, E.; Koch, N.; Puschnig, P.; Meghdadi, F.; Niko, A.; Resel, R.; Ambrosch-Draxl, C.; Knupfer, M.; Fink, J.; Bredas, J. L. and Leising, G. (2000): Structure, morphology, and optical properties of highly ordered films of para-sexiphenyl, Physical Review B (volume 61), issue 24, pp. 16538-16549. URL: ISI:000088008400039

[90] Horowitz, G.; Bachet, B.; Yassar, A.; Lang, P.; Demanze, F.; Fave, J. L. and Garnier, F. (1995): Growth and Characterization of Sexithiophene Single-Crystals, Chemistry of Materials (volume 7), issue 7, pp. 1337-1341. URL: ISI:A1995RK99300010

[91] Servet, B.; Horowitz, G.; Ries, S.; Lagorsse, O.; Alnot, P.; Yassar, A.; Deloffre, F.; Srivastava, P.; Hajlaoui, R.; Lang, P. and Garnier, F. (1994): Polymorphism and Charge-Transport in Vacuum-

Evaporated Sexithiophene Films, Chemistry of Materials (volume 6), issue 10, pp. 1809-1815. URL: ISI:A1994PM63000039

[92] Resel, R.; Koch, N.; Meghdadi, F.; Leising, G.; Athouel, L.; Froyer, G. and Hofer, F. (2001): A polymorph crystal structure of hexaphenyl observed in thin films, Crystal Research and Technology (volume 36), issue 1, pp. 47-54. URL: ISI:000167697000006

[93] Fauvarque, J. F.; Petit, M. A.; Digua, A. and Froyer, G. (1987): Electrochemical Synthesis of Poly(1,4-Phenylene) Films, Makromolekulare Chemie-Macromolecular Chemistry and Physics (volume 188), issue 8, pp. 1833-1839. URL: ISI:A1987K978100007

[94] Louarn, G.; Buisson, J. P.; Lefrant, S. and Fichou, D. (1995): Vibrational Studies of A Series of Alpha-Oligothiophenes As Model Systems of Polythiophene, Journal of Physical Chemistry (volume 99), issue 29, pp. 11399-11404. URL: ISI:A1995RK55000016

[95] Vogel, J. O.; Salzmann, I.; Opitz, R.; Duhm, S.; Nickel, B.; Rabe, J. P. and Koch, N. (2007): Sub-nanometer control of the interlayer spacing in thin films of intercalated rodlike conjugated molecules, Journal of Physical Chemistry B (volume 111), issue 51, pp. 14097-14101. URL: ISI:000251792500006

[96] Lovinger, A. J.; Katz, H. E. and Dodabalapur, A. (1998): Direct imaging of conducting and insulating submolecularly wide pathways in an organic semiconductor, Chemistry of Materials (volume 10), issue 11, pp. 3275-+. URL: ISI:000077129200007

[97] Park, J. S.; Vo, A. N.; Barriet, D.; Shon, Y. S. and Lee, T. R. (2005): Systematic control of the packing density of self-assembled monolayers using bidentate and tridentate chelating alkanethiols, Langmuir (volume 21), issue 7, pp. 2902-2911. URL: ISI:000228042400043

[98] Prost, R. (1973): Influence of Christiansen Effect on Ir-Spectra of Powders, Clays and Clay Minerals (volume 21), issue 5, pp. 363-368. URL: ISI:A1973S137000011

[99] Koch, N. (1997): Morphologie und elektronische Eigenschaften von dünnen, elektrolumineszierenden Filmen aus p-hexaphenyl, Technische Universität Graz.

[100] Koch; Nickel, B.; Ghjisen, J.; Elschner, A.; Schwartz, J.; Pireaux, J. J. and Kahn, A. (2003): Metal vs. Polymer Electrodes in Organic Devices: Energy Level Alignment, Hole Injection, and Structure, MRS Proceedings (volume 771), issue L3.6.

[101] Cosseddu, P. and Bonfiglio, A. (2006): Soft lithography fabrication of all-organic bottom-contact and top-contact field effect transistors, Applied Physics Letters (volume 88), issue 2. URL: ISI:000234606900081

[102] Cosseddu, P.; Vogel, J.-O.; Fraboni, B.; Rabe, J. P.; Koch, N. and Bonfiglio, A. (2009): Continuous Tuning of Organic Transistor Operation from Enhancement to Depletion Mode, Advanced Materials (volume 21), issue 3, pp. 344.

[103] Takami, K.; Akai-Kasaya, M.; Saito, A.; Aono, M. and Kuwahara, Y. (2006): Control of conduction of iodine-doped poly(3-octylthiophene) thin films by double-tip scanning tunneling microscopy, Chemical Physics Letters (volume 419), issue 1-3, pp. 250-253. URL: ISI:000235438900049

[104] Cohen, M. J.; Coleman, L. B.; Garito, A. F. and Heeger, A. J. (1974): Electrical-Conductivity of Tetrathiofulvalinium Tetracyanoquinodimethan (Ttf) (Tcnq), Physical Review B (volume 10), issue 4, pp. 1298-1307. URL: ISI:A1974U039900017

[105] Samori, P.; Francke, V.; Müllen, K. and Rabe, J. P. (1999): Self-assembly of a conjugated polymer: from molecular rods to a nanoribbon architecture with molecular dimensions, Chemistry-A European Journal (volume 5), issue 8, pp. 2312-2317. URL: ISI:000081866100012

[106] Maoz, R.; Matlis, S.; DiMasi, E.; Ocko, B. M. and Sagiv, J. (1996): Self-replicating amphiphilic monolayers, Nature (volume 384), issue 6605, pp. 150-153. URL: ISI:A1996VT33600060

[107] Schmidt-Mende, L.; Fechtenkotter, A.; Mullen, K.; Moons, E.; Friend, R. H. and MacKenzie, J. D. (2001): Self-organized discotic liquid crystals for high-efficiency organic photovoltaics, Science (volume 293), issue 5532, pp. 1119-1122. URL: ISI:000170432600054

[108] Cacialli, F.; Wilson, J. S.; Michels, J. J.; Daniel, C.; Silva, C.; Friend, R. H.; Severin, N.; Samori, P.; Rabe, J. P.; O'Connell, M. J.; Taylor, P. N. and Anderson, H. L. (2002): Cyclodextrin-threaded conjugated polyrotaxanes as insulated molecular wires with reduced interstrand interactions, Nature Materials (volume 1), issue 3, pp. 160-164. URL: ISI:000181498700018

[109] Kato, T. (2002): Self-assembly of phase-segregated liquid crystal structures, Science (volume 295), issue 5564, pp. 2414-2418. URL: ISI:000174712600044

Abbreviations

AFM	atomic force microscope
SPM	scanning probe microscope
STM	scanning tunneling microscope
FTIR	Fourier transform infra red spectroscope
NIR	near infra red
ν	wave number (cm^{-1})
UV/VIS	ultra violet and visible spectral range
ε_0	electric constant ($8.854...10^{-12}$As/Vm)
ε_r	relative static permittivity
TF	thin film
HT	high temperature
LT	low temperature
CC	conjugated core
vdWL	van der Waals length
o.-o.-p.	out of plane
γ(C-H)	bending vibration
ν_s	symmetric stretch vibration
ν_a	asymmetric stretch vibration
δ(C-H)	ring deformation vibration
d	inter layer distance
XRD	X-ray diffraction
i.p. XRD	in-plane XRD
q_z	momentum transfer vector normal to substrate surface

$\mathbf{q_{xy}}$	momentum transfer vector parallel to substrate surface
OSC	organic semiconductor
OLED	organic light emitting devices
OFET	organic field effect transistor
OHPV	organic heterojunction solar cell
MOSFET	metal oxide semiconductor field effect transistor
$\mathbf{V_D}$	voltage between source and drain contact
$\mathbf{V_G}$	voltage between source and gate contact
$\mathbf{I_D}$	current between source and drain contact
$\mathbf{V_t}$	threshold voltage
μ	charge carrier mobility
HTL	hole transport layer
ETL	electron transport layer
HOMO	highest occupied molecular orbital
LUMO	lowest unoccupied molecular orbital
$\mathbf{\Phi}$	work function
$\boldsymbol{E_{BI}}$	binding energy
D	donator
A	acceptor
ITO	Indium-Tin-oxide

Acknowledgement

This work would not exist without the help of numerous people I want give my deep appreciation.

Dr. Norbert Koch was my supervisor for the duration of this thesis. Besides sharing his knowledge about organic electronics with me, he also gave me a lot inspiration how the business of science works.

Prof. Dr. Jürgen P. Rabe the head of our work group and the speaker of SFB 448 of the DFG, which was my source of founding.

Dr. Ingo Salzmann and **Dr. Stephen Duhm** performed all X-ray diffraction experiments for me and helped me with the analysis.

Dr. Piero Cosseddu and **Prof. Annalisa. Bonfiglio** (University Cagliari) made the fruitfull collaboration possible and were giving the DH6T/6T films an actual application. Thank you for the very nice time in Berlin and Cagliari.

Manuel Genzler, **Philipp Lange**, and **Dr. Ingo Salzmann** for the proof reading of my manuscript.

My room mates (in chronological order) **I Min**, **Susie Gröper**, **Rolf Kniprath**, **Philipp Lange**, **Manuel Gensler** made my work in these 4 years a really pleasant one.

Evi Poblenz helped to keep the chaos out of the lab and was keeping an eye on our all safety.

Sabine Schönherr, **Claudia Stephan**, and **Martina Sae-Chew** for the excellent job on organization.

Last but not least my **family** who always supported me. I am as proud of them as they are (hopefully) of me.

Erklärung

Hiermit erkläre ich, Jörn-Oliver Vogel, diese Dissertation selbstständig erarbeitet habe und alle Hilfsmittel und Hilfen angegeben habe. Die verwendete Literatur und die Beiträge Dritter sind kenntlich gemacht.

Berlin den

Jörn-Oliver Vogel